CHARACTERISATION OF HVDC GAS INSULATED SYSTEMS

Thesis submitted to

CARDIFF UNIVERSITY

For the degree of

DOCTOR OF PHILOSOPHY

HAOLUAN LI

SCHOOL OF ENGINEERING

AUGUST 2023

Summary

This research investigated a challenging objective related to the future needs of transmission networks. To develop an environmentally friendly gas insulated system for HVDC applied voltage, extensive simulation and experiments have been done before the proposed solution could be deployed in industry.

The electric field distribution under DC applied voltage using an initial design of the spacer with and without temperature gradient was first introduced. When calculating with the initial design, different conductivity models with linear and nonlinear characteristics were used to explore the electric field distribution under DC steady state conditions controlled by the conductivity of the material.

Fundamental investigations on the properties of spacer shapes including increasing the spacer thickness, introducing a small gas gap at the spacer-flange interface, increasing the radius of the flange corner, varying the radius of the spacer edge near the ground side, increasing the spacer inclination angle, varying the distance between the spacer and the end of the flange radius, and the spacer materials using different conductivity models with linear and nonlinear characteristics were researched.

A finite element model combining steady-state and transient solvers was used to simulate the electric field distribution and space charge distribution in a gas-insulated system under DC superimposed lightning impulse voltage, which revealed the ion transportation law under lightning excitation.

C4-PFN and CF_3I based gas mixtures were tested electrically for withstand tests in a reduced scale gas insulated system and PDIV tests under DC applied voltages with positive and negative polarities at different pressures from 1 to 5 bar (abs.) with different electrode shapes and different gap distances.

A list of more detailed conclusions and discussion points are presented at the end of each chapter, and which are further developed in the last chapter of this thesis. Suggestions that can potentially be implemented in future works, experimental and theoretical, are also listed.

Contents

Acknowledgement

The completion of this research work would have not been possible without the guidance and assistance of many kind people.

I would like to express my sincere gratitude to my brilliant supervisors Prof. Manu Haddad, Dr. Nabila Zebouchi and Dr. Alistair Reid for their continuous technical guidance throughout my PhD study. I will also remember the valuable instructions I obtained from them beyond the research.

I would like to thank my parents for their encouragement and unconditional support throughout my life.

I would like to thank Mr. Meirion Hills and Mr. Christopher Stone for their support and assistance in setting-up the experiment in the high voltage lab.

I would like to acknowledge Dr. Michail Michelarakis, Dr. Mohammed Slama and Dr. Houssem Nechmi for their assistance and discussions from the view of industry which made me develop and complete important parts of this thesis.

I would like to thank my girlfriend, Mis. Ruimei Zhang for her accompany through my tough period.

I would also like to thank all my colleagues and friends at Cardiff University for all the motivation and inspiration I got from them.

Abbreviations

GIL	Gas insulated lines
AC	Alternative current
HVDC	High voltage direct current
GIS	Gas insulated switchgear
HVAC	High voltage alternating current
SF_6	Sulphur hexafluoride
GWP	Global warming potential
CO_2	Carbon dioxide
ODP	Ozone depletion potential
CF_3I	Trifluoroiodomethane
C4-PFN	C4-Perfluoronitril
N_2	Nitrogen
BPA	Bonneville Power Administration
ABB	ASEA Brown Boveri
Al_2O_3	Alumina
SiO_2	Silica
DGEBA	Diglycidyl ether bisphenol A
3M	Minnesota Mining and Manufacturing
LC50	Lethal Concentration 50%
OEL	Occupational Exposure Limits
FGM	Field grading materials
ZnO	Zinc oxide
2D-axisy	Two-dimensional axisymmetric
3D	Three-dimensional
2D	Two-dimensional
ATO	Antimony doped tin oxide

List of Figures

List of Tables

Chapter 1 Introduction

1.1 Background

The power transmission system is undergoing fundamental changes. To meet the growing power demand in urban centers, and to transport renewable energy such as wind power, solar energy, photovoltaics, biological, tidal, etc. from remote areas to load centers, large-capacity, long-distance transmission lines have been or are under construction all over the world. These long-distance transmissions use overhead lines, in which the towers are tall, and the wire bundles are large. This is not possible to build everywhere. Underground transmission or at least partial use of underground transmission may be required. For this demand, the gas insulated transmission system has become a good choice for the solution.

Alternating current (AC) power was widely used in the first stage of grid development due to its flexibility. However, in some special cases, the advantages of high voltage direct current (HVDC) power transmission surpass AC power transmission. Especially with the emergence of thyristors, HVDC power transmission is more attractive. With the continuous increase of transmission capacity, in order to solve the stability problem, the increase in the use of electrical equipment during AC transmission is extremely expensive. In contrast, the power loss of direct current (DC) transmission is much lower than that of AC transmission, and when transmitting power over long distances, the cost of DC transmission systems is lower.

High voltage gas insulated switchgear (GIS) and gas insulated lines (GIL) have been in use for high voltage alternating current (HVAC) electricity transmission for over 50 years, while the development of HVDC applications is still under development. New compact HVDC GIS and GIL are being developed around all over the world because of the increasing need to transmit electricity from these remote generating sites to populated areas. Underground HVDC GIL technology is particularly suitable for transmitting very high power over long distances due to its carrying capacity and low losses.

Epoxy insulators, also known as spacers, are often used in gas insulation systems to isolate gas zones and mechanically support the conductors. The electric field

distribution is largely determined by the permittivity under HVAC applied voltage, which does not vary with temperature. In contrast, the electric field distribution under HVDC applied voltage depends on the electrical conductivity of the spacer's material, which also depends on the temperature. At the same time, in addition to the effect of electrical conductivity, the shape of the spacer also significantly affects the electric field distribution at the interface between the gas, conductor/enclosure, and spacer, also called triple junction [1] [2]. At present, the research on HVDC GIS/GIL spacers is not fully developed, so it is very necessary to investigate the optimization of GIS/GIL spacers.

Sulphur hexafluoride (SF_6) is widely used in high voltage equipment, such as GIS and GIL, thanks to its excellent dielectric strength and arc interruption capability, but SF_6 is a highly potent gas due to its high global warming potential (GWP), which is approximately 23,900 times more than that of carbon dioxide (CO_2) over a given 100-year time horizon [3]. Therefore, environmentally friendly alternative gases are needed to replace the usage of SF_6 in a variety of high voltage equipment. The candidates must meet the environmental and safety requirements such as low GWP, no Ozone depletion potential (ODP), low or no-toxicity, non-flammability and safe to human health.

In recent years, C4-Perfluoronitrile (C4-PFN) and Trifluoroiodomethane (CF_3I) as new types of environmentally friendly gases have attracted the attention of researchers. They have the characteristics of high dielectric strength, non-flammability, low GWP and no or low ODP, while the disadvantage of these compounds is that they have a higher boiling point than SF_6. When used in lower temperature electrical equipment, the operator must use buffer gases, such as CO_2 and dry air, to reduce the liquefaction temperature of the final mixture.

1.2 Research Objectives

This research investigation is aiming to address a challenging objective related to the future needs of transmission networks. To develop an environmentally friendly gas insulated system for HVDC applied voltage, extensive simulation and

tests are required before the proposed solution could be deployed in industry. In this study, fundamental investigations on the properties of spacer shapes including increasing the spacer thickness, introducing a small gas gap at the spacer-flange interface, increasing the radius of the flange corner, varying the radius of the spacer edge near the ground side, increasing the spacer inclination angle, varying the distance between the spacer and the end of the flange radius, and the spacer materials using different conductivity models with linear and nonlinear characteristics were first researched. Then C4-PFN and CF_3I based gas mixtures were tested electrically for withstand tests in a reduced scale gas insulated system and PDIV tests under DC applied voltages with positive and negative polarities at different pressures from 1 to 5 bar (abs.) with different electrode shapes and different gap distances to analyze the feasibility of using such alternative gases to replace the usage of SF_6. This will open the prospect of new equipment designs that adopt non-SF_6 alternative gas mixtures as an insulation medium in gas-insulated systems. There are three main objectives of this work: (a) To modify the spacer design, which is to improve the original spacer design for HVAC to be suitable for HVDC gas insulated systems. (b) To verify the feasibility of spacer shape optimization under different gas mixtures. (c) To determine partial discharge levels on C4-PFN/CO_2 and CF_3I/CO_2 gas mixtures using different electrode configurations, gap distances, gas pressures, and polarities of the applied voltage. It is worth noting that both CO_2 and N_2 are widely used as buffer gases in C4-PFN or CF_3I based gas mixtures for the replacement of SF_6 since both gases are chemically inert, and CO_2 possesses similar dielectric strength compared to that of N_2 [4], while in this research CO_2 is selected due the fact that the insulation performance when using CO_2 as buffer gas is greater than that when using N_2 as buffer gas[5]-[6]. Besides, since the current literature of the insulation performance comparison between using CO_2 as buffer gas and using N_2 as buffer gas is still limited, further study is required in the dielectric strength and their chemical reactions with different materials in the gas insulated system.

The research programme undertaken for this study is extensive and wide-ranging, with tasks including the design, development, and fabrication of the spacers and the prototypes. Different types of experimental investigations were also carried out for

various gas mixtures under HVDC applied voltage to determine their insulation strength.

The main tasks to complete in order to achieve the above objectives are to:

- Perform the required simulation to identify high electric field regions with the original spacer design used for a HVAC GIL, which will ensure a better understanding of the electric field distribution with the initial geometry under HVDC applied voltage.
- Modify the shape and materials of the spacer to reduce the electric field especially at critical regions, which will be suitable for future eco-friendly HVDC compact gas-insulated systems.
- Determine the electric field distribution using the modified spacer under HVDC and superimposed lightning impulse voltage to ensure better understanding with the modified geometry.
- Design and fabricate a reduced-scale coaxial test system which has a similar electric field distribution as that of a full-scale 500 kV DC GIL. The test system is used to provide fundamental knowledge under HVDC applied voltage.
- Conduct verification tests using the modified spacer on the reduced-scale coaxial test system under HVDC applied voltage. The results will provide an insight into the performance of modified spacers using different gas mixtures for future SF_6 free compact GIS/GIL applications.
- Develop a reliable test rig for partial discharge experiments using different gases and gas mixtures which consists of a pressure vessel, different electrode configurations, and the setup for the generation and measurement of HVDC voltage and current waveforms.
- Perform experimental partial discharge tests on different electrode configurations, gap distance and pressures under different polarities of HVDC applied voltage. The results will provide an early indication on the usage of SF_6 free gas mixtures in GIS/GIL applications.

1.3 Contribution of the Thesis

The main contributions of the present work can be summarized as follows:

- The electric field distribution under DC voltage with and without temperature gradient was calculated using an initial spacer model design for a full-scale 420kV HVAC GIL.
- The optimization of the spacer shape was performed to fulfill the demand of the dielectric performance under HVDC applied voltage.
- Different types of spacer materials were introduced and investigated with and without the presence of a temperature gradient.
- The electric field distribution and the positive and negative ion density on the surface of the spacer were calculated under DC superimposed lightning impulse voltage.
- Reduced-scale coaxial test system was developed and fabricated to perform withstand test with and without spacers using dry air, 4% C4-PFN / 96% CO_2 and 30% CF_3I / 70% CO_2 gas mixtures.
- A test rig was developed for partial discharge tests using CO_2, 4% C4-PFN / 96% CO_2 and 30% CF_3I / 70% CO_2 gas mixtures under DC applied voltages at different pressures from 1 to 5 bar (abs.) with different electrode shapes and different gap distances.
- The experimental investigation was conducted to determine the partial discharge performance of CO_2, C4-PFN/CO_2 and CF_3I/CO_2 gas mixtures.

1.4 Organization of Thesis

This thesis is divided into 7 chapters:

CHAPTER 2- *Spacers for Gas Insulated Systems and non SF6 alternative gas mixtures: A Review*

This chapter provides a review of published literature with regard to the study

undertaken. A general review of spacer design and modification in gas insulated systems is presented with previous investigations by other researchers and the potential of C4-PFN and CF_3I and their mixtures as alternatives to replace the usage of SF_6. The purpose is to support the overall discussion on the reasons why the usage of HVAC spacers is limited when used for HVDC applications and a well performing compound such as SF_6 needs to be replaced, and what are the requirements needs to fulfil.

CHAPTER 3- *Improved Design of HVDC Gas Insulated System Spacer*

This chapter reports the first computation results of the electric field distribution using an initial design proposal for a spacer model. In order to obtain the desirable shape of the spacer model enabling local electric field enhancements at the critical regions to be avoided under DC voltage, based on electric field modelling with COMSOL Multiphysics software, an optimized shape of a spacer model was presented, and different types of materials were considered and investigated, which gave a better understanding for future HVDC spacer design.

CHAPTER 4- *Characteristics for HVDC GIS/GIL Spacer under DC Superimposed Lightning Impulse Voltage Conditions*

This chapter presents the results of modelling of electric field distribution and positive and negative ion density on the surface of the spacer in a gas-insulated system using the modified spacer under DC superimposed lightning impulse voltage, which provided the theoretical basis to the safety, standardization, and design of the future gas insulated system. Time-dependent electrostatic model is adopted because the discharge was relatively mild without strong current. Hence, the resulting magnetic field is almost negligible, and the Lorentz force effect of the magnetic field on charged ions was not taken into account. Electrostatic refers to the COMSOL module, and time-dependent considered the evolution process of the spatial ion concentration Np and Nn under the condition that the voltage changed with time.

CHAPTER 5- *Design of Reduced Scale GIL and Associated Laboratory Equipment*

This chapter describes the test equipment that were adopted for the experiments. A reduced-scale coaxial GIL prototype was designed and fabricated to investigate the dielectric performance of the optimized shape with conventional material spacers, and partial discharge characteristics using different gases and alternative gas mixtures.

CHAPTER 6- *Laboratory experiments on SF6 free gas mixtures*

This chapter presents the results of voltage withstand tests with optimized-shape spacers using different materials under HVDC applied voltage with different gas mixtures and the investigations on partial discharge inception voltage using different electrode configurations, gap distances and pressures under positive and negative polarities of HVDC applied voltage.

CHAPTER 7- *Conclusion and Future Work*

This chapter provides the conclusion of the work carried out for this PhD thesis and proposes new investigation ideas for continuing research work in the future.

Chapter 2 Spacers for Gas Insulated Systems and non SF_6 alternative gas mixtures: A Review

2.1 Introduction

High voltage gas insulated switchgear (GIS) and gas insulated lines (GIL) are mature technologies that operate in HVAC applications, while the development of HVDC applications is still challenging. The basic structure of the GIS busbar is similar to that of the GIL [5]. The inner conductor is coaxially surrounded by an outer enclosure, and the space between them is filled with SF_6 or SF_6/Nitrogen(N_2) compressed gas as an insulating medium. However, SF_6 is a gas with high global warming potential (GWP), with its GWP equivalent to 23,900 times that of CO_2, and the atmospheric lifetime is estimated to be over 3,000 years [3]. A more environmentally friendly gas is needed to replace SF_6.

At the same time, GIS/GIL contains solid insulators: (i) post-type insulators which can hold the high voltage conductor in the center; (ii) non-gas tight or gas tight insulators which can fix high voltage conductors in the center. The former can provide gas passages, and the latter also called spacer can divide the gas cell unit to create gas zones. Spacers are the key components in GIS/GIL systems. There are several issues which limit the usage of HVAC spacers in GIS/GIL when used for HVDC applications.

This chapter reviews the development status of gas insulation systems and their important position in power systems. Among them, HVDC GIS/GIL spacers have significant technical challenges. Then, another aspect which this chapter evaluates is the literature on SF_6 and possible alternatives C4-PFN, CF_3I and their various gas mixtures in GIS/GIL.

2.2 Review of Gas Insulated System Technology

2.2.1 Main Features and Benefits of Gas Insulated System

As shown in Fig. 2.1, GIL is essentially a coaxial cylindrical electrode arrangement composed of two concentric aluminum tubes. GIL allows the substation to be fitted into an enclosed space by using a different gas to air and pressurizing the gas. Normally, SF_6 or its mixture with other gases is the main

insulating medium, and the busbar inside the equipment is supported by the insulators.

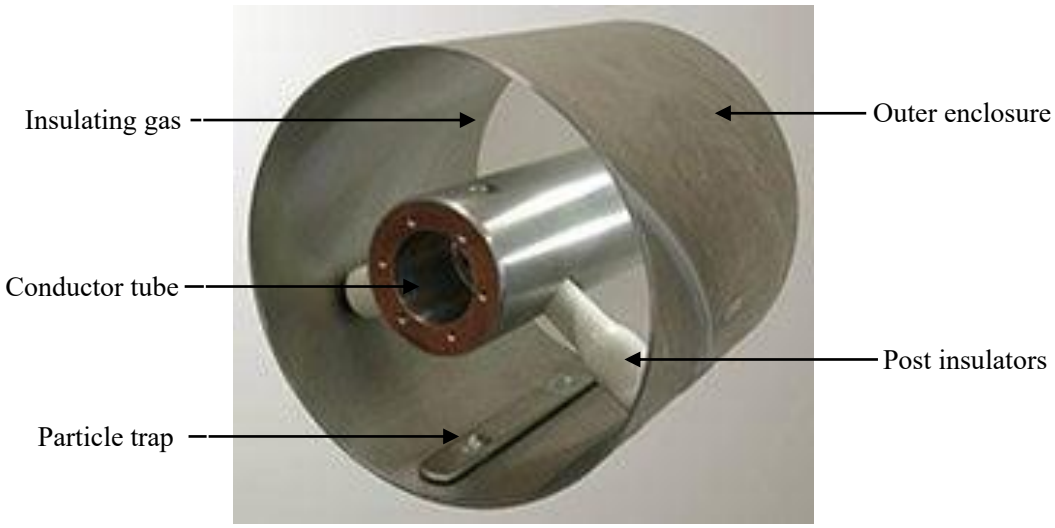

Fig. 2.1. A GIL showing conductor, enclosure, post-type, and particle traps insulators [7].

The differences between GIL and GIS are mainly in the following aspects:

- GIL can be used for a longer distance. It has greater transmission capacity, while GIS also includes circuit breakers, disconnectors, grounding switches, current transformers, voltage transformers, lightning arresters, and other equipment.
- A particle trap is set in GIL to reduce the adverse effects of free conductive particles [8], while the busbar in GIS is generally not equipped with particle traps due to the short unit length and easy inspection.
- GIL has a flexible turning angle unit, which can be installed in an inclined shaft within the range of 85° to 178° [5], while the busbar in GIS generally only contains a right-angle steering unit.

The advantages of using a gas insulated power transmission systems are as follows [9]:

- Low power transmission loss

Compared to overhead lines and power cables, the resistive loss is low due to the large cross section of the conductor and the enclosure. The outer diameter 500mm

or 600mm and the enclosure and conductor wall thickness 6-15mm, and the typical GIL resistance is 6-8 MΩ/km. When the rated current of the GIL is high, the characteristic of low loss becomes more significant, and the loss in the insulating gas is negligible.

- High level of safety

The energised components are fully enclosed by the grounded outer conductors. The safety of GIL can still be guaranteed when it is subjected to short-circuit current.

- High reliability

The sole purpose of GIL is to transmit electricity, so internal switching capabilities are not required. Based on these characteristics, GIL can be regarded as a high-voltage gas insulation system without moving parts.

- No electrical aging

Aging of gaseous insulators is negligible, and the best example is overhead lines using air as insulating gas. The electric field strength of the insulator and the maximum temperature of the gas insulated systems are low that no aging will occur. This has been confirmed by long-term testing in laboratories and the experience of many devices.

- Same operation as overhead lines

Overhead lines can be operated in automatic reclosing mode, which means that when a ground fault is detected, the circuit breaker will automatically cut off the line and close it again after a few seconds. In most cases, the condition that causes the short-circuit operation will be removed and the transmission line will resume its normal operation.

- No thermal aging

GIL is designed to operate at the highest operating temperature given by external conditions. Different temperatures depending on different countries and their standards are adopted. In all cases, the maximum allowable temperature of the conductor is close to 120°C, which is hard to reach, so the system will not actually age under these operating conditions.

- Minimised footprint

The GIS equipment has a compact structure, a small, occupied space, and a small volume, so it is more suitable for urban power grids, hydropower grids, and underground substations.

2.2.2 Applications of Gas Insulated System

The installation of the first-generation GIL was introduced in 1974 [9]. Because the oil cable of the Schluchsee pumping storage power plant in Germany suffered a major failure, it caused major losses to the cable and the tunnel. Therefore, the power plant tried to use a GIL scheme without burning risk to connect a 420kV high-voltage transformer with the overhead conductors through a 700-meter-long GIL tunnel. This is also the first generation of GIL, and its filling gas was 100% SF_6. After 35 years of regular maintenance and inspection, it was still in operation without any major failure. The first GIL performance index is shown in Table. 2.1.

Table. 2.1. Performance index of the first generation GIL [9].

Type	Value
Nominal voltage	380 kV(rms)
Maximum voltage	420 kV(rms)
Nominal current	2000 A(rms)
Peak lightning impulse voltage	1640 kV
Peak switching impulse voltage	1200 kV
Rated short-time current	135 kA
Rated gas pressure	7 bar abs
Insulating gas mixture	100% SF_6

The environmental problems caused by SF_6 prompted the development of the second-generation GIL. The main solution was to change the filling gas to a gas mixture, such as 80% N_2 and 20% SF_6. At the same time, new laying techniques and technologies had been adopted to reduce the total project cost, making a more economical solution for long-distance power transmission. First application of the second-generation GIL was at the International Telecommunication Exhibition

(2003) in Geneva, Switzerland. During the expansion of the PALEXPO exhibition venue, the GIL solution was used to replace the original high-voltage overhead wires due to the low magnetic field and high transmission capacity requirements [9]. The main technical data of the project is shown in the Table. 2.2.

Table. 2.2. Performance index of the second generation GIL [9].

Type	Value
Nominal voltage	300 kV(rms)
Operation voltage	220 kV(rms)
Nominal current	2000 A(rms)
Peak lightning impulse voltage	1050 kV
Peak switching impulse voltage	850 kV
Rated short-time current	50 kA/s
Rated gas pressure	7 bar abs
Insulating gas mixture	80% N_2/20% SF_6

The earliest metal-enclosed GIS began to be known in the 1930s [9]. In 1968, the world's first batch of high-voltage GIS using SF_6 as insulating and arc extinguishing medium was put on the market and installed in the 110kV Wittenau substation in Berlin, Germany. At that time, the air-tight aluminum casting process had not come out, and the size of the casting mold was limited, so the earliest GIS design used steel instead of aluminum as material for the enclosure, and then started using aluminum as the enclosure by the 1980s.

The busbar structure of GIS [5] is shown in Fig. 2.2. The research and development of GIS started very early. In the Americas, since 1985, the Bonneville Power Administration (BPA) in Portland, United States, had been committed to the development of GIS under DC voltage [10]. In 1988, BPA and ASEA Brown Boveri (ABB) in Zurich, Switzerland started to investigate GIS under DC voltage and, in 1996, AC 550kV and 800kV GIS was successfully converted into ± 500kV DC GIS.

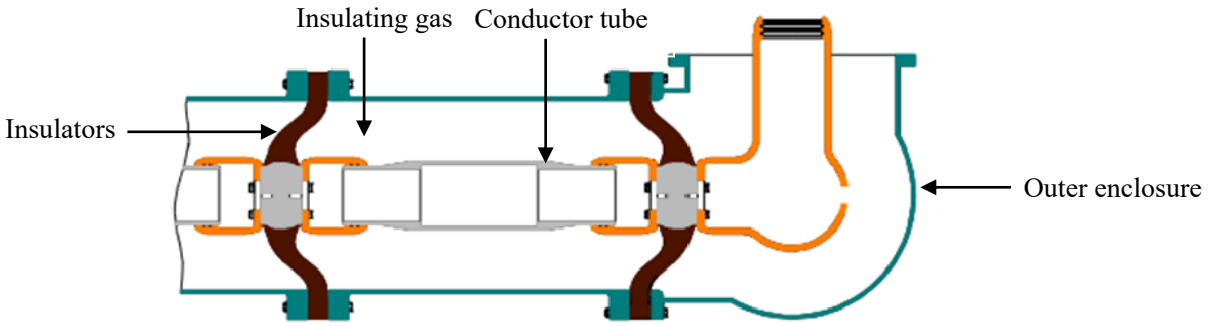

Fig. 2.2. A busbar section of GIS [5].

In Asia, Japan conducted years of research on ±500 kV HVDC GIS development in the 1980s. Technical problems were solved, and appropriate solutions were found through test verification [1], [11], [12] which led to the world's first commercial DC GIS installed at Anan converter station [13]. However, the GIS was large and had been operating at ±250 kV since 2000. Due to the increasing demand for HVDC power transmission, people have renewed interest into HVDC GIS, and today's focus is to further improve and develop compact HVDC GIS, as described in [14] [15]. In addition, with the acquisition of ABB Power Grids by Hitachi, ABB has developed ±350 kV rated voltage DC GIS [16], and now the ±550 kV rated voltage DC GIS is being developed. With the development of UHV transmission in China [17] and the growing interest in the development of large hydropower resources from the mountainous area of central China to the load center in the east, UHV DC transmission uses compact HVDC GIS/GIL technology to transmit ±800 kV and above seems promising.

In Europe, Siemens is ahead since compact HVDC switchgear with rated voltages of ±350 kV and ±550 kV [18] has been sold on the market [19], which can be used on wind farm DC offshore converter platforms. In addition, the development of a compact HVDC underground GIL for operation at ±550 kV and a rated current of up to 5000A has been completed, and this new transmission technology is approaching the market [20], [21].

2.2.3 Technical Challenge for Development of Spacers for HVDC GIS/GIL

The use of polymeric materials for high voltage transmission line insulators has been adopted for decades [22]. Up to now, the conventional material of the spacer in the gas insulation system is an epoxy-based matrix filled with alumina (Al_2O_3) or silica (SiO_2) particles [23]. The epoxy matrix usually consists of a base resin mixed with a hardener and a catalyst. Diglycidyl ether bisphenol A (DGEBA)-based resin and acid anhydride hardener are among the materials considered. The concentration of the filler is 60-70% per weight. Alumina-filled epoxy composite material seems to be the most suitable material in GIS, mainly because it can resist SF_6 decomposition by-products due to breakdown. However, the epoxy composite formulation is proprietary to the GIS/GIL manufacturer.

Spacers are the key components in the gas insulated systems. Although spacers are developed for HVAC applications, they cannot be used for HVDC applications due to the following main problems: [24]

(i) Resistive electric field enhancement

The electric field distribution near and along the surface of the spacer is controlled by the electrical conductivity of the gas and the spacer's epoxy material, under steady-state DC operating voltage, and the conductivity of the spacer's epoxy material depends on the electric field and the temperature. When the GIS/GIL is operating at full load, a temperature gradient will occur between the conductor and the enclosure due to the direct current flow and the ohmic loss caused by the Joule effect in the conductor. As a result, there will be a difference in the conductivity between the conductor and the enclosure.

In addition, besides the effect of the spacer's material electric conductivity, the shape of the spacer and its contacts with the high voltage conductor/ground enclosure and the surrounding gas called triple junctions, also change the electric field distribution especially at the triple junctions where it can be significantly intensified. Therefore, the shape of the spacer and its triple contact must be properly designed to keep the high electric field (tangential, normal, and total) strength

within a permissible level.

(ii) Charges accumulation on the spacer's surface

The charge can accumulate on the surface of the spacer and will introduce additional changes in the electric field distribution, which is a very serious problem when GIS/GIL is subjected to continuous high DC voltage or under polarity reversal, and it may lead to unpredictable surface arcing along the spacer. Therefore, it is important to understand and clarify the accumulation of surface charge in order to limit its amount to an acceptable level.

(iii) Flashover under superimposed lightning/switching impulse voltage onto DC operating voltage

When the HVDC GIS/GIL is turned on and off and under lightning strikes, the accumulated charge on the surface of the spacer will lower the dielectric strength. Therefore, in order to design a reliable HVDC spacer, it must fulfill the demand of DC superimposed lightning and switching impulse withstand voltage levels.

(iv) Metallic Particles

Metallic particles contamination inside the GIS/GIL enclosure caused by production, assembly, transportation and switching operations should be avoided for DC application as is the case in HVAC application. When the metal particles are adsorbed on the surface of the spacer due to interaction with the surface charge of the spacer and gravitational force, the electric field distribution on the surface of the spacer will be deposited, which brings greater insulation threat. [1] and [12] have proved that these metallic particles have a drastic influence on the GIS/GIL insulation performance not only on the spacer's surface but also on the gas gap insulation.

2.3 Comparison of the Properties of SF_6, C4-PFN and CF_3I Gases and Their Mixtures

Based on long-term GIS/GIL operation and maintenance experience, SF_6 has been proven to be a very reliable insulating medium, but in order to fundamentally

solve the greenhouse effect and global warming [17], [25], it is necessary to use environmentally friendly gaseous media to completely replace the usage of SF_6.

This section introduces the basic properties of SF_6 and its proposed alternative gases C4-PFN, CF_3I and their mixtures, as well as alternative technologies and their limitations. The comparison shows the similarities of the gases and explores the various advantages and disadvantages of each gas used for this purpose.

2.3.1 Physical and Chemical Properties

Sulfur hexafluoride was discovered by Moissan and Lebeau [26] in 1900 with a molecular formula of SF_6. It is synthesized directly from sulfur and fluorine elements and its molecular structure is shown in Fig. 2.3. In the development and evaluation stage of SF_6, it has been determined that SF_6 has high dielectric strength and useful interruption performance, so it is currently used in GIS/GIL applications [27]. SF_6 has strong electronegativity, high dielectric strength, and its breakdown voltage is almost 3 times that of air under atmospheric pressure [28].

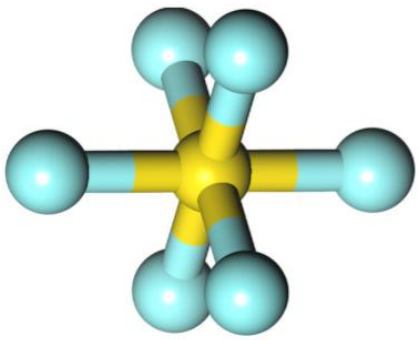

Fig. 2.3. SF_6 molecular structure [29].

C4-PFN, introduced by Minnesota Mining and Manufacturing (3M) Company in St. Paul, the United States, has a molecular formula of C_4F_7N, and its molecular structure is shown in Fig. 2.4. The molecular structure consists of 12 atoms.

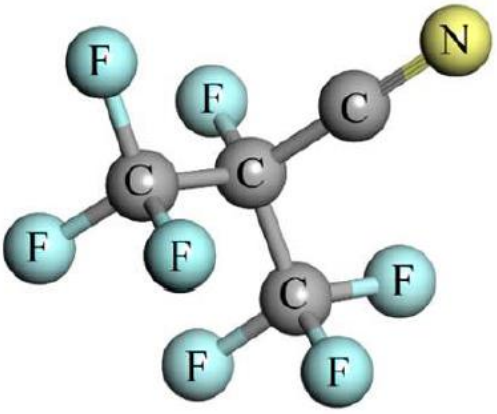

Fig. 2.4. C4-PFN molecular structure [30].

CF_3I is also a potential SF_6 substitute gas [31]. Its molecular structure is shown in Fig. 2.5. The molecule is composed of 5 atoms. The presence of fluorine and iodine makes CF_3I very easy to adsorb electrons and has strong electron adhesion ability, which inhibits the generation and development of electron avalanche in CF_3I gas.

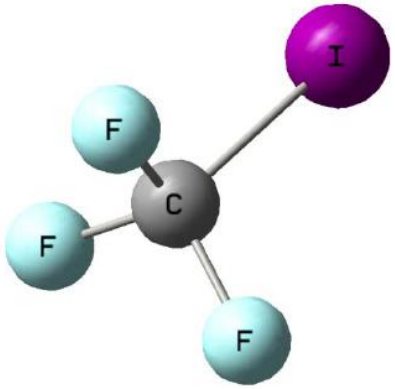

Fig. 2.5. CF_3I molecular structure [31].

The specific physical and chemical properties of SF_6, C4-PFN and CF_3I are shown in Table. 2.3[32]-[36]. It can be seen that these three gases have similar characteristics. For example, they are all colorless and odorless, and they are all much heavier than air. The boiling point of SF_6 is much lower than that of C4-PFN and CF_3I, while the boiling point of C4-PFN is the highest which is -4.7°C. This means that when the pressure increases, SF_6 can maintain a gaseous form and has a higher dielectric strength. Each gas has a critical point, which is defined by the

corresponding critical temperature and critical pressure. At this critical point and above, the distinction between gas and liquid disappears, which is called the supercritical region.

Table. 2.3. Comparison of properties for SF_6, C4-PFN and CF_3I[32]-[36].

Formular	SF_6	C4-PFN	CF_3I
Molar mass(g/mol)	146	195	196
Boiling point(°C)	-63.8	-4.7	-22.5
Appearance	Colorless gas	Colorless gas	Colorless gas
Door threshold	Odorless	Odorless	Odorless
Critical temperature(°C)	45.6	122.8	122
Critical Pressure (MPa)	3.78	2.5	4.04

2.3.2 Environmental Impact

Environmental impacts are generally based on two parameters: global warming potential (GWP) and ozone depletion potential (ODP). GWP is a relative measure of the ability of greenhouse gases to trap heat in the atmosphere compared with that of CO_2. ODP is the relative amount of degradation to the ozone layer that a chemical compound can cause with trichlorofluoromethane (CFC-11) being fixed at an ODP of 1.0.

Table. 2.4 shows the ODP and GWP of CO_2, SF_6, C4-PFN and CF_3I [34], [37]. SF_6 has a very high GWP and a long atmospheric lifetime, making it an unwelcome gas medium in high voltage and other applications. In contrast, compared with SF_6 the GWP of C4-PFN and CF_3I are much lower. It is worth noting that the life spans of C4-PFN and CF_3I are very short, and the global warming potentials of these two gases is lower in practice since the gases are unlikely to be evenly distributed on a global scale. Nevertheless, the global warming potential values are still significantly lower than SF_6, making them a more environmentally friendly alternative.

Table. 2.4. Global warming potential for CO_2, SF_6, C4-PFN and CF_3I [34], [37].

Chemical Formula	Lifetime (years)	Ozone Depletion Potential	Global Warming Potential for 100 years
CO_2	-	0	1
SF_6	3200	0	23900
C4-PFN	30	0	2100
CF_3I	0.005	<0.09	<5

2.3.3 Toxicity Review of SF_6, C4-PFN and CF_3I

As a pure gas, SF_6 has no known hazardous toxicity levels. However, since SF_6 is denser than air, SF_6 will pose a risk of suffocation for anyone entering a closed area if a large amount of SF_6 is released and allowed to settle in a closed space such as a tunnel. According to the gas material safety data sheet provided by Air Liquide Company, toxicological effects of SF_6 are not expected if Occupational Exposure Limit (OEL) values are not exceeded, and the OEL of SF_6 is 1,000 ppm[38]. When there is a trace amount of moisture and other impurities inside the gas insulated equipment, the by-products produced by the electrolysis will continue to react in these impurities to generate gases such as HF, SOF_2, SO_2F_2, SO_2 and H_2S [25],[39]. These decomposition products have a certain degree of toxicity and may also interact with the gas inside the insulation equipment to corrode the equipment. With regards to the toxicity of C4-PFN, according to the gas material safety manual provided by 3M Company, the Lethal Concentration 50% (LC50) of C4-PFN is higher than 10,000 ppm, and the OEL of C4-PFN is 65 ppm [40]. The experiments on rats showed that 1.5% C4-PFN had a certain degree of damage to rat lung, kidney, intestine and brain tissue, and had little effect on eyes, skin, heart, and liver. The LC50 of C4-PFN on rats for 4 hours is in the range of 15,000 ppm and 20,000 ppm [41]. The main breakdown byproducts of the C4-PFN/CO_2 gas mixture are perfluorocarbons and perfluoronitriles, including CO, CF_4, C_2F_4, C_2F_6, C_3F_6, C_3F_8, C_4F_6, C_4F_{10}, C_2N_2, CF_3CN, C_2F_3CN, C_2F_5CN, HCN, and HF[42]. Since most of the products have a lower electrical strength than C4-PFN, the insulation performance after multiple breakdowns can gradually become degraded. When it comes to the

toxicity of CF_3I, inhalation tests [43] indicated that adverse effects were seen in rats at concentrations of 100,000 ppm or greater; for subacute exposures, changes in some thyroid measures were seen at 20,000 ppm, and hematologic effects and decreased body weights were seen at 40,000 ppm; for sub-chronic exposures, hematologic effects were seen at 2.0%, which concluded that CF_3I is a slightly toxic gas. The main breakdown byproducts of the CF_3I/CO_2 gas mixture are $C_2F_6O_3$, C_2F_6, C_3F_8 and CF_4 with potential by-products of $C_2H_3F_3$, C_2F_5I or C_2F_9I, C_2HF_5 and CHF_3[44]. Besides, some of the decomposition products are toxic, so special care should be taken when handing the decomposed gases.

2.4 Review of Numerical and Experimental Investigations on Alternative Gases and GIS/GIL Spacers

The current research showed that the electric field distribution, the maximum electric field strength, and its location vary with the type of the applied voltage, and the electric field is intensified near the triple junction areas formed by the triple contact. The temperature gradient in the gas insulated systems has a large effect on the electric field distribution. Geometrical modification of the spacer's profile can mitigate the local concentration of the electric field at the critical locations. Besides, the electric field distribution is strongly influenced by the electric conductivities of the epoxy spacer's material and the surrounding gas. It has been also found that C4-PFN/CO_2, and CF_3I/CO_2 are promising gas candidates to replace the usage of SF_6, and the research on the substitution of SF_6 mainly focuses on the dielectric strength of these two types of gas mixtures.

This section reviews the numerical modelling and experimental research on spacers as the main solid insulating material in gas insulation systems, as well as previous research using C4-PFN, CF_3I and their gas mixtures as alternative insulating media.

2.4.1 Development of Spacer Designs and their Characterization

The current research on spacers is mainly focused on their electric field

distribution, maximum electric field strength, surface charge accumulation, insulation properties, shape optimization, and different novel materials. The electric field distribution under DC is affected by the conductivity of the spacer material and the surrounding gas. Since the conductivity of the epoxy spacer material is temperature dependent, the electric field distribution on the insulating material is also affected by the radiated heat from inner conductor due to load current.

Several researchers have conducted investigations concerning the influence of spacer shape under DC applied voltage [45]-[50], surface charge accumulation [51]-[54], and novel material for spacers [55]-[58]. Koch et al. [59] found that, with the non-linear behavior of the temperature gradient, spacers have a large influence on the electric field distribution. Without the temperature gradient, the high electric field occurred near the inner conductor, while, with the temperature gradient, the high electric field region was located on the surface of the spacer, leading to a shift towards the enclosure as shown in Fig. 2.6. It worth noting that the electric field intensity the electric field distribution is higher with temperature gradient than that without temperature gradient.

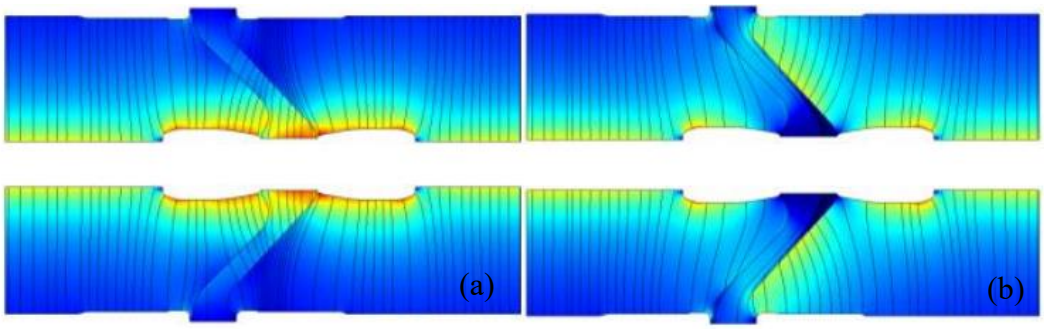

Fig. 2.6. Electric field distribution under DC applied voltage without (a) and with (b) temperature gradient due to spacer conduction [59].

Vu-Cong et al. [60] calculated that, when the impulse voltage was superimposed on the pre-applied DC voltage of the opposite polarity, the electric field strength is higher than that under the condition of the polarity reverse of DC voltage, as shown in Fig. 2.7. It is worth noting that the applied impulse voltage is lighting impulse voltage with the peak value 1050 kV which is defined in the IEC 62271-203.

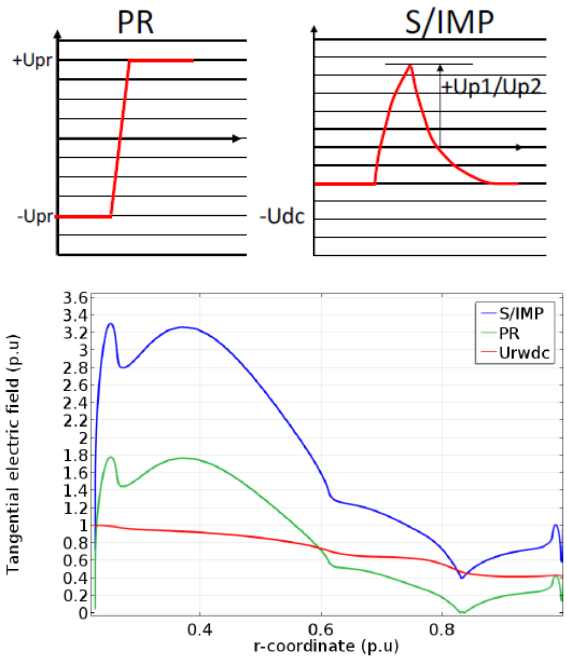

Fig. 2.7. Comparison between polarity reversal and superimposed impulse voltage under DC voltage (PR: Polarity reversal, S/IMP: DC superimposed lightning impose voltage) [60].

Geometrical modification of the spacer's inclination angle, creepage distance, and thickness can reduce the electric field strength at the critical regions [61]-[63]. In order to obtain the desirable shape of the spacer model under DC voltage, it is necessary to consider a small normal electric field on the spacer surface to minimize surface charge accumulation, and sufficient creepage distance to prevent surface flashover caused by a high tangential electric field. In [61], different spacer geometries shown in Fig. 2.8 were studied, and the results were compared with the optimized cone-shaped spacer, which has been commercially available in DC GIS.

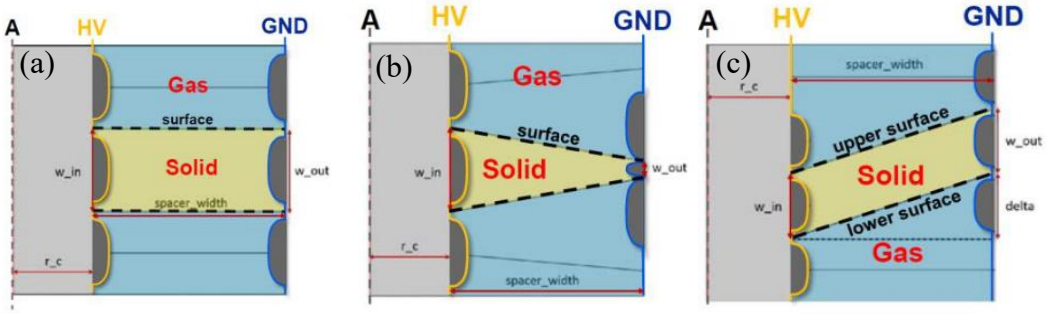

Fig. 2.8. Geometries of (a) rectangular, (b) trapezoidal, (c) slanted spacers design. HV conductor radius=50mm, spacer width=120mm, spacer thickness=50mm (a,c) [61] .

Compared with traditional epoxy resin spacers, spacers made of non-linear conductive electric field grading materials (FGM) composed of epoxy filled with functional fillers can significantly reduce the electric field concentration in high-stress areas[64]-[65]. Fig. 2.9 and Fig. 2.10 show the tangential electric field distribution along the spacer made of the epoxy filled with zinc oxide (ZnO) microvaristors and filled with IriotecR 7000 (Merck Group, Darmstadt, Germany) that consists of flake shaped mica particles at 500kV DC and covered with a nano-scale semiconducting antimony-doped tin oxide (ATO) layer, denoted in the reviewed papers as mica functional filled (MFF) [65], respectively. It is worth noting that in Fig. 2.9 E_b is switching field strength, and σ(E) is the conductivity of the insulator.

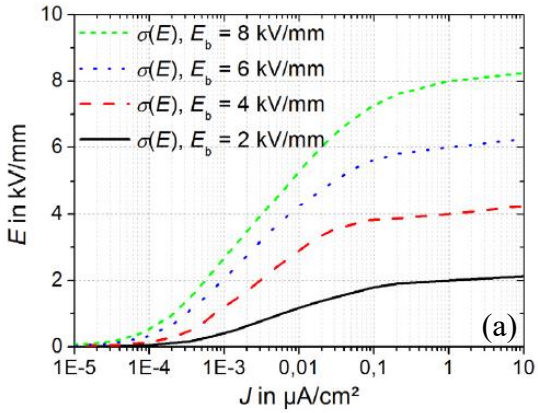

(a) Nonlinear E-J curves of ZnO microvaristor filled epoxy.

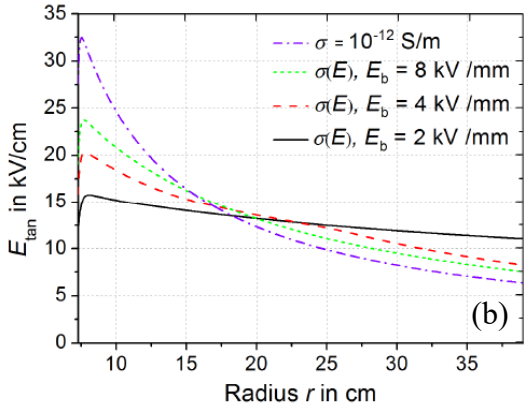

(b)E_t along the spacer surface.

Fig. 2.9. Electric field distribution along the spacer surface with different conductivities of ZnO microvaristor filled epoxy, (a) Nonlinear E-J curves. (b) Tangential electric field distribution along the spacer surface [64]. Noting that E_b is switching field strength and σ(E) is the conductivity of the insulator.

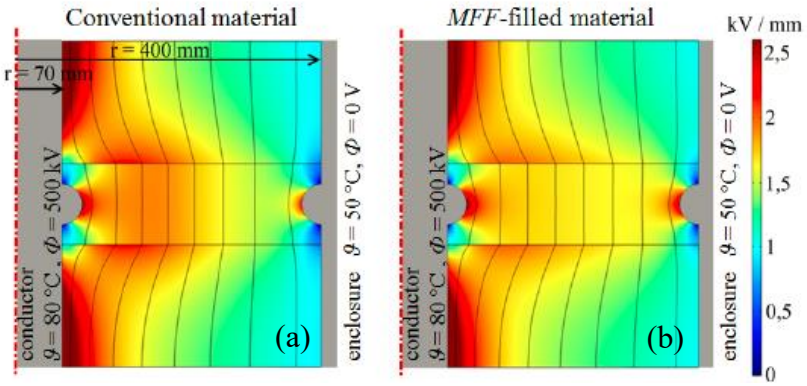

(a) Spacer with conductivity σ= 10^{-13} S/m. (b) *MFF*-filled spacer with bulk conductivity.

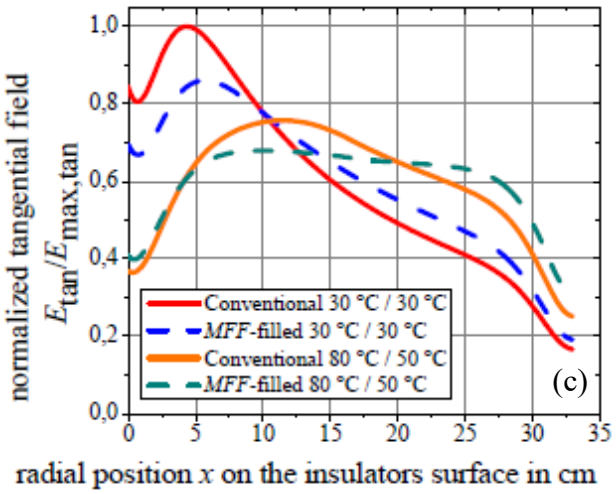

(c) Normalized tangential electric field distribution at the spacer surface with and without temperature gradient

Fig. 2.10. Electric field distribution on the spacer under 500kV DC applied voltage (a) Spacer with conductivity σ= 10^{-13} S/m; (b) *MFF*-filled spacer with bulk conductivity; (c) Normalized tangential electric field distribution at the spacer surface with and without temperature gradient [65].

Nakanishi et al. [65] used an electrostatic probe to measure the surface charge accumulation of conical epoxy spacer setting in coaxial cylinder bus with compressed SF_6 gas under DC voltage. After a positive 100kV voltage was applied, charge accumulated on the surface of the sample. After 5 hours of continuous testing, the charge would no longer change and would remain at a saturation level. Under negative DC voltage, negative charge deposited circumferentially on the concave part of spacer, but the negative surface charge was not observed on the convex part of the spacer when positive DC voltage was applied to the conductor. The reason is that negative surface charge was considered to be caused by the field emission when

negative voltage was applied. The negative charge carriers supplied by the field emitted electrons from protrusions on the conductor migrate along the direction of electric field and reach the concave surface of spacer. The negative surface charge was not observed on the convex part of spacer in the positive polarity experiment, because the electric stress on the outer conductor is too low for the field emission. Through comparison of the surface charges under the two polarity voltages, it was found that the negative charge was greater than the positive charge, which means that negative charge was easier to accumulate. When the applied voltage was removed, the residual surface charge cannot be completely dissipated in a short time, and the charge distribution remained unchanged even after 15 hours.

Sato et al. [66] used two direct high-voltage levels of 600kV and 800kV to study corona discharge on the epoxy spacer surface. After removing the applied voltage, the surface charge was continuously recorded. The statistical data showed that the surface charge can only dissipate about 1% of the charge per hour on the epoxy spacer surface, indicating that the surface charge would affect the electric field distribution characteristics of the insulator surface for a long time and would significantly increase the possibility of flashover on the surface.

Based on the calculation and analysis of the electric field of the tapered partition applied by the compact HVDC ±320 kV DC GIS, Hitachi Power Grids successfully demonstrated the system with multiple insulators through geometric optimization of the partition and the insertion of a current collector and passed the verification test [61].

2.4.2 Research on Alternative Gases

As a gas insulating medium used in power equipment, the insulation design process of electrical equipment needs to rely on a large amount of basic data of gas insulation, such as partial discharge inception voltage, breakdown field strength, maximum field strength of flashover along the surface and arc extinguishing performance. Several researchers [67]-[71] have reviewed the discharge characteristics of SF_6 when mixed with various gases. At the same time, many researchers [72]-[76] have carried out macroscopic insulation performance tests

using alternative gases and their mixtures.

Nechmi et al. [77] used different electric field structures in the range of 1-10 bar to study the AC and both positive and negative lightning impulse breakdown characteristics of fluoronitrile/CO_2 gas mixtures. The results showed that, when the gas mixtures contained 20% of fluoronitrile, the breakdown voltage was equivalent to pure SF_6 at 1 bar(abs.) as shown in Fig. 2.11.

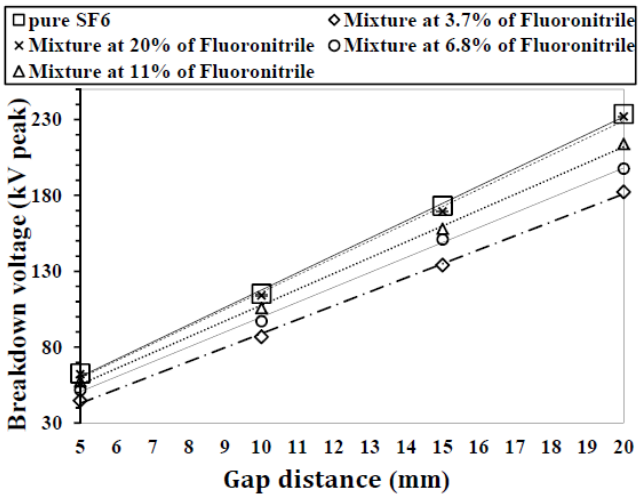

Fig. 2.11. AC breakdown voltage of C4-PFN /CO_2 mixture, SF_6 at 1 bar(abs.), in sphere-to-sphere configuration [77]

The lightning impulse breakdown voltage of the gas mixture containing 3.7% C4-PFN under a uniform field is equivalent to 72% of the SF_6 dielectric strength at 5.5 bar(abs.). In order to achieve the same insulation level with SF_6, the pressure of the gas mixture needs to be increased to 0.88 bar as shown in Fig. 2.12.

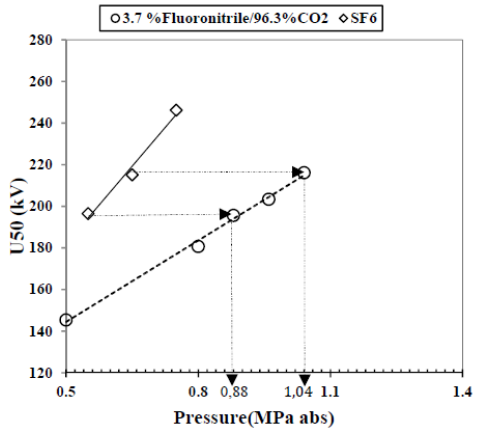

Fig. 2.12. Lightning impulse breakdown characteristics of 3.7% C4-PFN/96.7% CO_2 mixture and pure SF_6 for plane-plane electrode configuration [77]

In a non-uniform field, the lightning impulse test results of the gas mixture containing 3.7% C4-PFN showed that, as the pressure increased or the non-uniform coefficient increased, there was a cross point between the positive and negative breakdown voltage curves, and Fig. 2.13 shows the crossover point between positive and negative lightning impulse breakdown voltages. The effect of gas pressure depends on the polarity of applied voltage. This is linked to the corona stabilization region up to the critical pressure P_c at which breakdowns and corona discharges will coincide. In the corona stabilization region under low pressure, it is more likely for negative breakdown voltage to be higher than positive breakdown voltage. The transition between these regions may cause a crossover between the breakdown trends of positive and negative polarities. It is proposed that the C4-PFN /CO_2 mixture with a mixing ratio of 3.7%/96.3% provides a good compromise and an appropriate substitute for SF_6 in high voltage apparatus for a minimum temperature of down to -30°C, but further study of C4-PFN /CO_2 mixture is required in the dielectric strength and their chemical reactions with different materials in the gas insulated system under DC applied voltage.

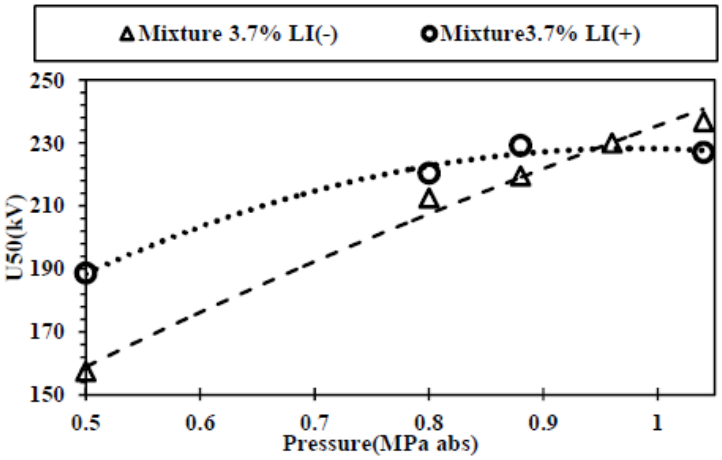

Fig. 2.13. Lightning impulse breakdown voltages of 3.7% C4-PFN/96.7% CO_2 mixture for a sphere- plane electrode configuration [77]

Tu et al. [78] measured the breakdown voltage, insulator flashover voltage, and the partial discharge inception voltage of C_3F_7CN/CO_2 gas mixtures under DC voltage with the ratio of 4% C_3F_7CN /96% CO_2 and 8% C_3F_7CN /92% CO_2. The result showed a growth trend of the DC breakdown voltage with the increase of the

pressure with the plane-plane electrode configuration with 3mm gap length as shown in Fig. 2.14.

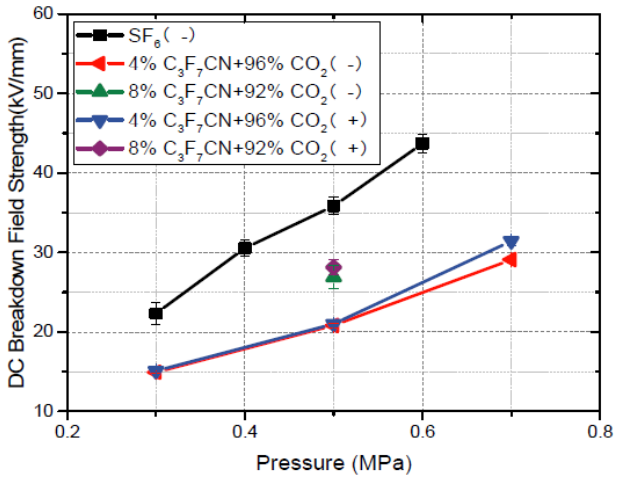

Fig. 2.14. Breakdown voltages of C4-PFN/CO_2 gas mixtures under DC voltage with sphere-plane electrode configuration with 3mm gap length [78].

While using the needle-plane electrode configuration with 5mm gap length, the negative breakdown voltage with the ratio of 4% C_3F_7CN/96% CO_2 and 8% C_3F_7CN/92% CO_2 increased with the increase of pressure, but the result of positive polarity exhibited the opposite trend as shown in Fig. 2.15. At the same gas pressure, for both gas mixtures, the negative breakdown voltage was significantly higher than the positive, and their difference increased with pressure.

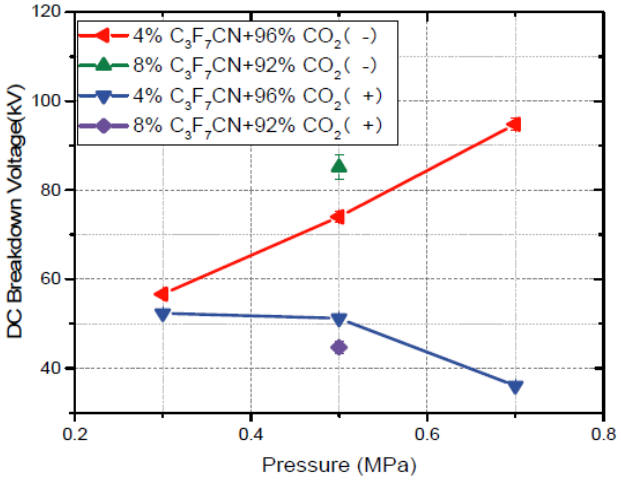

Fig. 2.15. Breakdown voltages of C4-PFN/CO_2 gas mixtures under DC voltage with needle-plane electrode configuration with 5mm gap length [78].

Fig. 2.16 shows the flashover voltage with the ratio of 4% C_3F_7CN/96% CO_2 and 8% C_3F_7CN/92% CO_2 using the needle-plane electrode configuration with 5mm gap length. The flashover voltage increased with the pressure, and the positive flashover voltage was lower than that of negative polarity at the same pressure.

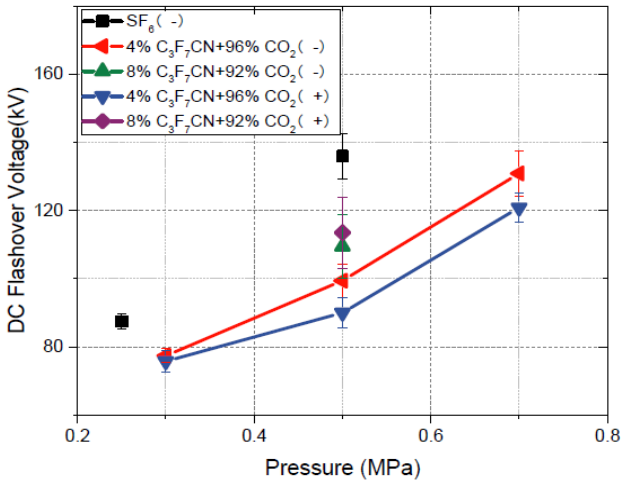

Fig. 2.16. DC flashover voltages of C4-PFN/CO_2 mixture and pure SF_6 for sphere- plane electrode configuration with 5mm gap length[78] .

Chen et al. [6], [79] studied the gas breakdown characteristics using rod-plane, plane-plane electrode configuration varying the gap length from 10mm to 50mm and coaxial GIL test system using 30%/70% of CF_3I/CO_2 under lightning impulse voltage at 1 bar(abs.). The test results show that the mixture of CF_3I/CO_2 has the practical value of replacing SF_6 in GIL, and CF_3I/CO_2 has better insulation performance than the same ratio of CF_3I/N_2 as shown in Fig. 2.17.

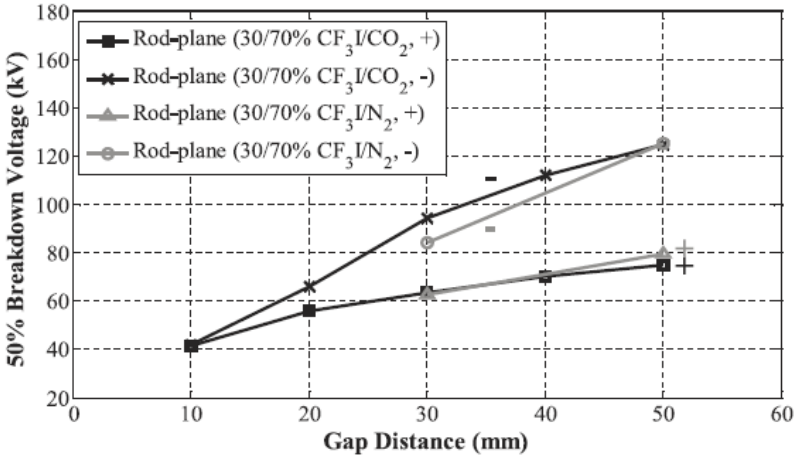

Fig. 2.17. Breakdown voltage U_{50} with rod-plane electrode configuration using the mixture ratio of 30%/70% for both CF_3I/CO_2 and CF_3I/N_2 gas mixtures at 1 bar (abs.) under lightning impulse voltage [6].

Fig. 2.18 shows the breakdown voltage using a coaxial system with 1cm of the inner conductor and under lightning impulse voltage. The result showed that the breakdown voltage increased with increasing pressure, and, with higher CF_3I content the breakdown voltage was higher.

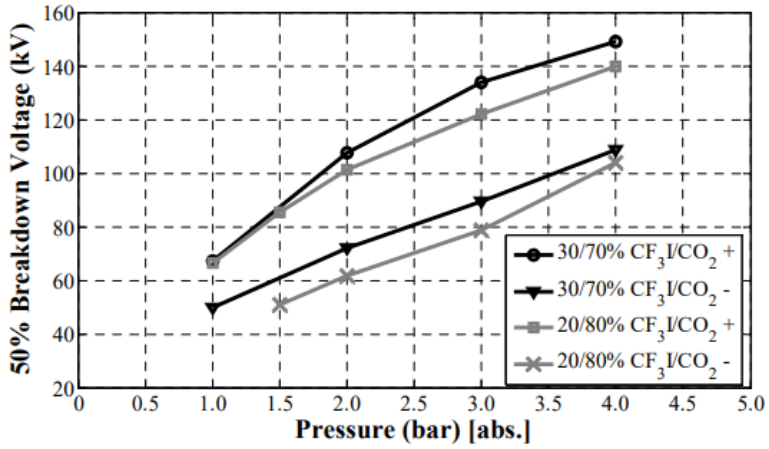

Fig. 2.18. Breakdown voltage U_{50} under positive and negative polarities for various CF_3I/CO_2 under lightning impulse voltage [79].

Ngoc et al. [80] used two sphere electrodes with the diameter of 10 mm to measure the breakdown voltage with different ratios of CF_3I/N_2 gas mixture under DC voltage, varying the gap distance from 0 to 2mm. The results showed that the

breakdown voltage of pure CF_3I is higher than that of SF_6, as shown in Fig. 2.19. The results showed that, up to 2 mm.bar, the CF_3I breakdown voltage was higher than that of SF_6. Fig. 2.20 shows the breakdown voltage of different ratio of CF_3I/N_2 gas mixture. The results showed a linear variation of breakdown voltage in the range from 1 to 5 mm.bar.

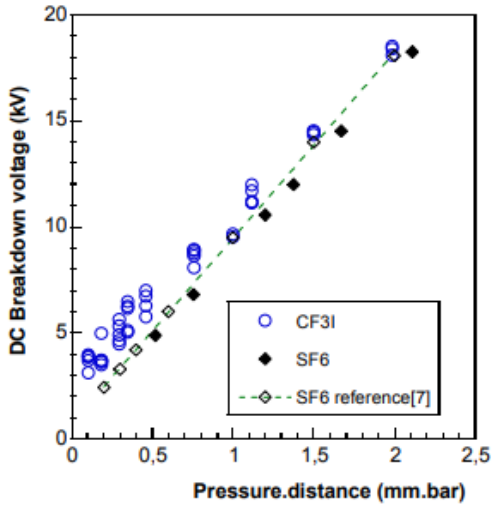

Fig. 2.19. Breakdown voltage in pure CF_3I and SF_6 under DC voltage [80].

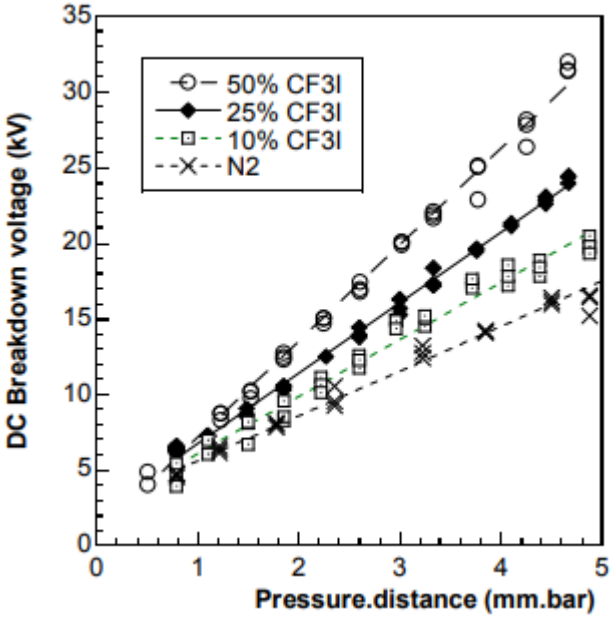

Fig. 2.20. Breakdown voltage in different ratio of CF_3I content under DC voltage [80].

Tu et al. [81] measured the breakdown voltage with the electrode system of a plane-plane configuration in uniform electric field with pure CF_3I, pure SF_6,

CF_3I/N_2, and SF_6/N_2 gas mixtures under negative DC voltage and lightning impulse voltage, and the gap distance was 3mm. Fig. 2.21 shows the breakdown field strength of pure SF_6, CF_3I/N_2 and $/N_2$ gas mixtures. The results showed that the dielectric strength of pure SF_6 is higher than all the gas mixtures, and that of $30\%CF_3I/70\%N_2$ is the lowest.

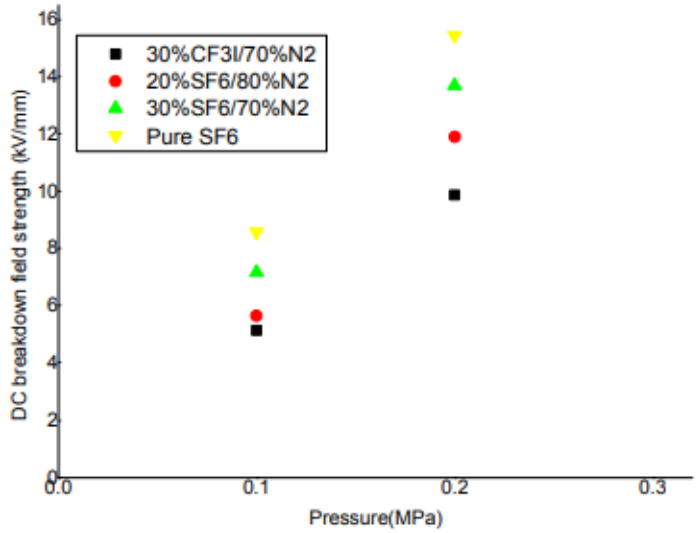

Fig. 2.21. Breakdown field strength of CF_3I/N_2, SF_6/N_2 gas mixtures and pure SF_6 gas under negative DC voltage [81].

2.5 Conclusion

New compact HVDC GIS and GIL are currently under development worldwide, and spacers are key components although they have been developed for HVAC applications, but they cannot be used for HVDC applications. This chapter presented an overview of the existing literature on gas insulation systems, their important component, spacers, alternative gas C4-PFN, CF_3I, and their various gas mixtures. The optimization of today's spacers needs the combination of the appropriate spacer shape design and the adjustment of the DC electric conductivity of the spacer's epoxy material by modifying slightly its chemical composition. Besides, testing of HVDC GIS and GIL prototype installations is required to demonstrate the reliability of the systems under real service conditions. Furthermore, the knowledge, the reliability and compatibility of alternatives to SF_6 in some commercial HVAC gas insulated systems under HVDC GIS/GIL gas

insulated systems are needed in extensively studied and test verified. From this literature review, several research gaps can be identified that are important to the improvement of gas insulation systems. These are listed as follows:

- Simulation based on a reduced-scale GIL along the spacer to develop an initial understanding of the electric field distribution.
- The optimization of geometric dimensions to effectively reduce the electric field strength of the critical region, thereby improving the insulation performance of the spacer.
- The adjustment of the DC electrical conductivity of the spacer's epoxy material by modifying its chemical composition to decrease the electric field strength.
- Development of a reduced-scale gas insulated system under HVDC voltage for the purpose of experimental withstand tests for modified spacers to verify the feasibility of spacer modifications.
- Experimental investigations on the partial discharge inception voltage of C4-PFN/CO_2, and CF_3I/CO_2 gas mixtures under HVDC applied voltage to determine the impact from gas pressure, gap distance, and applied voltage polarity.

All the above-mentioned actions will form the basis of the fundamental knowledge needed to characterize future gas insulated applications. It is hoped that this will contribute to improved reliability and continued operation of these systems and extend their lifespan, especially when using SF_6 alternative gas mixtures as an insulator in a full-scale gas insulated system under HVDC applied voltage.

Chapter 3 Improved Design of HVDC Gas Insulated System Spacer

3.1 Introduction

Testing of the electrical insulation performance of the full-scale high-voltage power equipment is time-consuming and costly. Therefore, a reduced-scale GIS/GIL system was constructed, with the purpose of studying the performance of spacers for future compact high-voltage DC GIS/GIL under higher electric fields having different shapes. The spacer is made of new advanced materials and will be contained in a new SF_6 gas-free gas environment.

In this chapter, the initial design of the spacer under DC applied voltage with and without temperature gradient is first introduced based on Multiphysics simulation. When calculating with the initial design, different conductivity models with linear and nonlinear characteristics were used to explore the electric field distribution under DC steady state conditions controlled by the conductivity of the material. Then, the shape and material optimization of the spacer were studied with and without the presence of a temperature gradient, and the surface charge accumulation was calculated with the optimized spacer. The optimized DC spacer model was tested on a reduced-scale GIL prototype for experimental verification. These results are presented in Chapter 6.

3.2 Finite Element Modelling

The commercial finite element package COMSOL Multiphysics was used for spacer modelling and electric field calculations. When solving a specific problem, three stages are involved, namely the pre-processing stage, the solution stage, and the post-processing stage.

- In the pre-processing stage, the basic principles of the model are developed and determined, such as the design of the geometry, definition of the materials, selection of the domains and boundary conditions, and the criteria of mesh.

- The solution stage is the execution stage of the simulation which is carried out using the relevant mathematical model of differential equations for a stationary or a time/frequency dependent study.
- Finally, in the post-processing stage, the user can view the results and generate graphs of various variables or parameters depending on the user's preference.

3.2.1 Scaled GIL Model

The GIL model was created in the AutoCAD software, which is a professional drawing tool, and then imported into COMSOL Multiphysics software. Since the shape of the vessel, electrode and spacer assembly is axisymmetric, the design was simplified to a two-dimensional axisymmetric (2D-axisy) model instead of a complete three-dimensional (3D) model. By adopting this approach, memory and processing time would be saved. Even in a two-dimensional (2D) model, the axisymmetric feature could further simplify the model without affecting the accuracy of the simulation results.

The initial geometrical structure that was modelled in this work was based on a conventional full-size cone spacer used in a HVAC 420 kV gas-insulated system and its geometry was reduced to 1/4 scale. Namely, the dimensions of the full-size gas-insulated system with respect to the central conductor outer diameter, the enclosure inner diameter, and the spacer shape are all downsized by a factor of 4. Fig. 3.1 shows the geometrical construction of the initial prototype design. The conductor and the enclosure are made of stainless steel and the spacer is made of conventional HVAC alumina-filled epoxy.

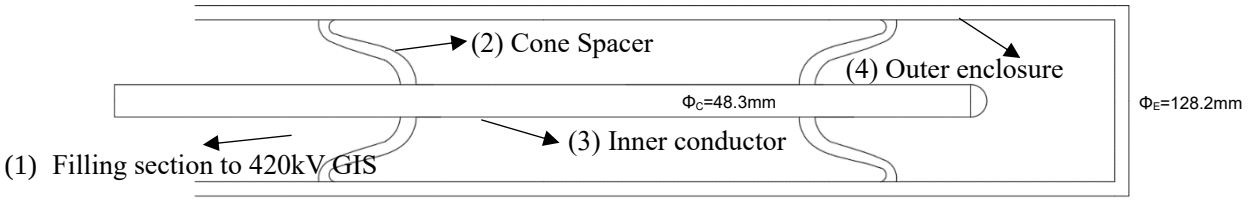

Fig. 3.1. Initial GIL geometrical structure drawn in AutoCAD (1) Filling section to 400kV GIS, (2) Cone Spacer, (3) Inner conductor, (4) Outer enclosure, the diameter of the conductor is 48.3mm, the diameter of the enclosure is 128.2mm, the thickness of the spacer is around 8mm, the length of the spacer is around 71mm.

3.2.2 Methodology and Governing Equations

The electric field distribution under stationary DC voltage was obtained from the equation of current conservation, Ohm's law, and the conductivity models of the spacer's material and the surrounding gas, as follows:

$$\nabla \cdot \overrightarrow{J_C} = \nabla \cdot (\sigma \vec{E}) = 0 \tag{3.1}$$

$$\vec{E} = -\nabla V \tag{3.2}$$

where:

$\overrightarrow{J_C}$ is the current density (A/m^2)

σ is the conductivity (S/m)

V is the electric potential (V)

$\vec{E}$ is the electric field (V/m)

Dirichlet boundary condition is used to define the electric potential on the high voltage and ground electrodes, and Von-Neumann boundary condition for insulating boundaries. The electric potential on the gaseous and the solid side of the spacer's surface are continuous. Dirichlet boundary condition means the mathematical constrains to specify its zero-order value at given boundaries. i.e. $\mathrm{V} = 0$ at the enclosure, and $\mathrm{V} = \mathrm{f(t)}$ at the conductor. The scalar field variable electrical potential V(x,y,z) is the dependent variable to be solved in the Finite Element Applications (FEA) model. Neumann boundary condition means the mathematical constrains to specify its first order gradient at given boundaries. i.e. $\mathbf{D} \cdot \mathbf{n} = 0, \varepsilon_0 \varepsilon_\mathrm{r} \mathbf{E} \cdot \mathbf{n} = 0, \varepsilon_0 \varepsilon_\mathrm{r} \boldsymbol{\nabla}(-\mathrm{V}) \cdot \mathbf{n} = 0$ at outer most exterior boundaries

3.2.3 Model Materials Properties

In the model, there were four important domains that need to be considered. These were the domains of the conductor, the enclosure of the pressure vessel, and the dielectric materials which were the spacers and the insulating gas. The C4-PFN (4%)/CO_2 (96%) and CF_3I (30%)/CO_2 (70%) gas mixtures were intended to be used in this work, but there are no published information data available about the DC

electrical conductivity, relative permittivity and thermal conductivity of these new gas mixtures. It is assumed in the calculations that their physical parameters are close to those of SF_6, namely the electrical conductivity is equal to 10^{-18} S/m [82], the thermal conductivity is equal to 0.0145 W/m.K and the relative permittivity is equal to 1. The specific parameters of spacer materials will be introduced in detail in the coming sections.

3.2.4 Mesh

The last part of the pre-processing stage is mesh generation. After completing the model with geometric drawing software, the model was imported into COMSOL Multiphysics. When completing the material properties and boundary conditions in the domain, the entire model was decomposed into non-overlapping triangular elements during the mesh process. According to the areas of interest, the triangular elements could be refined into smaller ones, thereby improving the accuracy of the simulation results.

In this model, the focus was on the triple junction formed at the conductor/enclosure-spacer-gas interface, because it has the highest electric field strength. Therefore, the element size was reduced, and the number of triangular elements was increased for the refinement of the mesh on the spacer surface. Choosing how much refinement was a trade-off between the accuracy of the drawing results, memory requirements and processing time. Further refinement of the mesh grid would produce a smoother electric field map but would need more computational memory and require longer processing time. The optimized refinement would require less simulation time without affecting the accuracy of the results.

3.2.5 Solver Settings

The model was simulated in the AC/DC module and Heat Transfer module through the COMSOL Multiphysics software. Electric current interface was used to calculate the electric field, current and potential distribution in the conductive medium under steady state conditions. The electronics solver module was used to

calculate the electric field and ion density under DC superimposed lightning impulse voltage. The Heat Transfer interface was used to compute temperature distribution. Stationary, time-domain and frequency-domain modeling are supported in all space dimensions.

3.3 Spacer model and Initial Simulation Results

The initial shape of the spacer model to be optimized for DC use is shown in Fig. 3.2, which was based on a commercial conventional full-size cone spacer used in HVAC 420 kV gas insulated system reduced to a ¼ scale. It's worth noting that the angle between spacer and conductor/enclosure is close to 90°.

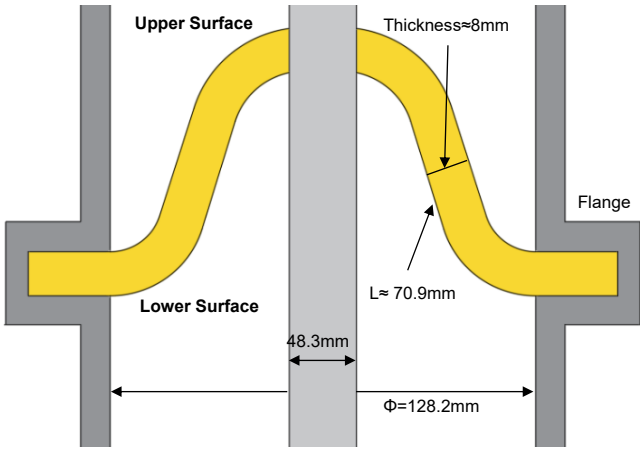

Fig. 3.2. Initial profile of the reduced scaled spacer model.

3.3.1 Electrical Conductivity Models of the Spacer Material

Two types of epoxy-based materials for the spacer were studied, (i) insulating and (ii) nonlinear resistive field grading materials with large and moderate nonlinearity. This starting investigation could give a general overview about their performance before selecting the category of materials to be used. Their thermal conductivity corresponds to 0.675 W/mK [83] and the relative permittivity is equal to 5 for (i) and to10 for (ii).

It was assumed that the conductivity behavior of the spacer's material with the electric field and the temperature is dependent on the material's constituents, such

as nature of the epoxy base resin, hardener type, catalyst, other additives as well as the type (insulating or semi-conductive), shape, size and filler concentration. Therefore, once the desired conductivity properties that fulfill the requirements of the electrical field distribution along the spacer are found by simulation, they can be experimentally fitted by the leakage current measurements through careful selection of the ingredients and tailoring the material composition.

3.3.1.1 Insulating material

According to published literature [64], [84]-[86], the behaviour of the DC electrical conductivity with electric field and temperature, σ(E, T), of alumina-filled epoxy material has been found to be weakly dependent on the electric field up to 10 kV/mm and strongly dependent on temperature where the conductivity increases by 2 to 3 decades from 20 ºC to the maximum operating temperature of 105 ºC. In general, the conductivity is expressed by the following two empirical models[84]-[86]:

$$\sigma_{insulating} = \sigma(E,T) = \sigma_0 \cdot e^{\alpha T + \beta E} \tag{3.3}$$

$$\sigma_{insulating}(E,T) = \sigma_0 \cdot e^{-\frac{W_a}{k_B T}} \cdot e^{\beta E} \tag{3.4}$$

where:

β is the field dependency coefficient (mm/kV)

α is the temperature dependency coefficient (K^{-1})

σ_0 is the specific conductivity constant (S/m)

k_B is the Boltzmann constant (eV/K)

W_a is the thermal activation energy (eV)

The second conductivity formula Equation (3.4) was used where its characteristics as a function of E and T are shown in Fig. 3.3 with σ_0=1.99 x10^2 S/m, β=0.08 mm/kV, W_a=0.95 eV, and K_B=8.62 x10^{-5} eV/K. It is worth noting that the second conductivity formula Equation determined Arrhenius behaviour by repeated polarization/depolarization measurements at various temperatures, which is more

accurate.

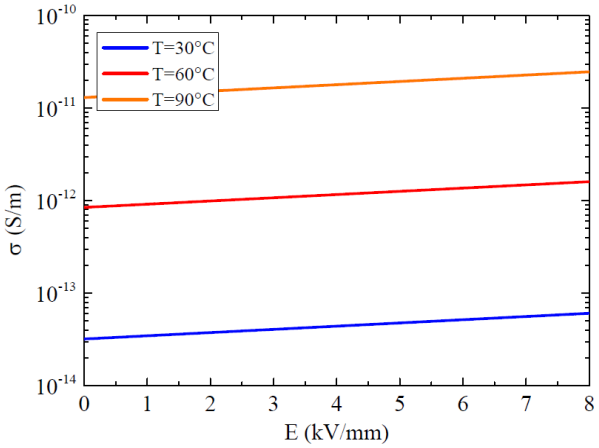

Fig. 3.3. Computing electric field and temperature dependent conductivity of the epoxy insulating material.

3.3.1.2 Nonlinear resistive field grading material

Electric field grading materials are used to reduce the local enhancements of the electric field in high voltage electrical apparatus. Nonlinear resistive field grading material (FGM) possesses a field-dependent conductivity which increases from a low conductivity value σ_0 to a high value at the switching field E_1 which indicates where the FGM becomes active. The electrical conductivity is constant at a low electric field intensity, whereas the electrical conductivity sharply increases when the electric field exceeds a certain threshold electric field. In addition, the electrical conductivity saturates in a certain electric field above the threshold electric field. Among the mathematical models that describe such nonlinear behavior of $\sigma_{FGM}(E)$, the following two expressions were reported in [87], [88]:

$$\sigma_{FGM}(E) = \sigma_o \frac{1+(\frac{E}{E_1})^{\gamma-1}}{1+(\frac{E}{E_2})^{\gamma-1}} \tag{3.5}$$

$$\sigma_{FGM}(E) = \sigma_o \cdot \frac{\sqrt[N_1]{1+10^{mN1(E-E_1)}}}{\sqrt[N_2]{1+10^{mN2(E-E_2)}}} \tag{3.6}$$

where:

σ_0 is the base conductivity (S/m)

E_1 is the switching field strength (kV/mm)

E_2 is the saturation field strength (kV/mm)

γ and m are the slopes of nonlinearity

N_1 and N_2 are the smoothing parameters

The latter conductivity model Equation (3.6) was used since it is high has a high nonlinearity. The base conductivity σ_0 should be higher than the conductivity of the adjacent gas insulation and its maximum value should not lead to degradation through heat losses. The switching electric field strength E_1 is the field strength where the conductivity of FGM starts to increase sharply. It is worth noting that E_1 is sensitive, and it should be approximated or close to E_1=applied voltage/spacer surface length. Further details about how to tailor all parameters of the nonlinear conductivity of Equation (3.6) for a spacer in HVDC gas insulated system was explained in [89]. Firstly, the minimum switching field strength E_1 is determined. As a second step, a range for the base conductivity for the continuous operation is specified. Then, the slope of the σ-E curve is optimized to dampen the maximum field strength. At last, to achieve optimal field grading, the minimum value for E_2 should lie above the mean field strength.

By considering the temperature effect, Equation (3.6) becomes:

$$\sigma_{FGM}(E,T) = \sigma_{o,T} \cdot exp\left(-\frac{Wa}{k_B \cdot T}\right) \cdot \frac{\sqrt[N_1]{1+10^{mN1(E-E_1)}}}{\sqrt[N_2]{1+10^{mN2(E-E_2)}}} \quad (3.7)$$

where:

$\sigma_{0,T}$ is the specific conductivity constant (S/m)

The curve of σ_{FGM}(E, T) is shown in Fig. 3.4 with the parameters: $\sigma_{0,T}$=2.20x10^{5}S/m, E_1=1.2kV/mm, E_2=4.8kV/mm, m=2.4 mm/kV, N_1=N_2=1 and W_a=0.95 eV. It is worth noting that the model is obtained according to the tailoring process as provided in the above section, and there is no experimental data at present.

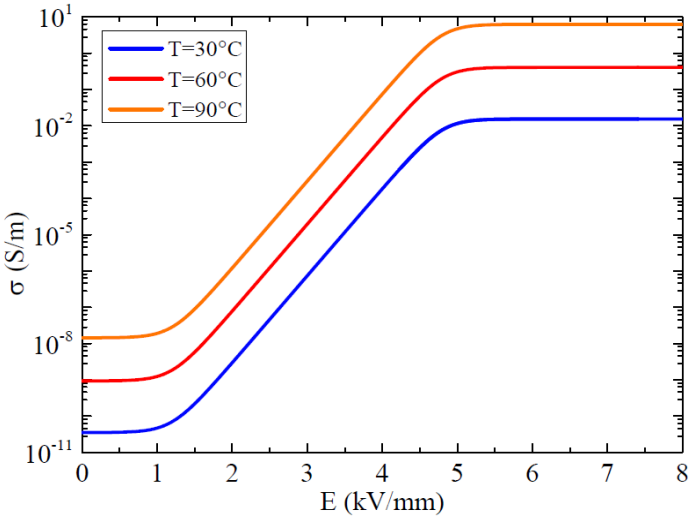

Fig. 3.4. Conductivity of FGM with T and E.

Today's most relevant epoxy based nonlinear resistive FGM is epoxy filled with ZnO microvaristors which has a high nonlinearity. The standard commercial composites have a switching field strength that does not exceed 1.2 kV/m. Some development studies have been undertaken to obtain higher switching field values for the use in compact HVDC GIS and are still ongoing [90].

3.3.1.3 Nonlinear resistive field grading material with moderate nonlinearity

Recently, a new FGM has been found to be a promising material for HVDC GIS applications [64] which is epoxy filled with Iriotec 7000 particles (Merck) formerly named Minatec that consist of flake shaped mica particles covered with a nanoscale semiconducting antimony doped tin oxide (ATO) layer. The experimental characteristics of this material's conductivity with the electric field and the temperature variations are shown in Fig. 3.5. Compared with highly nonlinear ZnO microvaristors-filled epoxy, Iriotec 7000 filled epoxy FGM has a moderate nonlinearity.

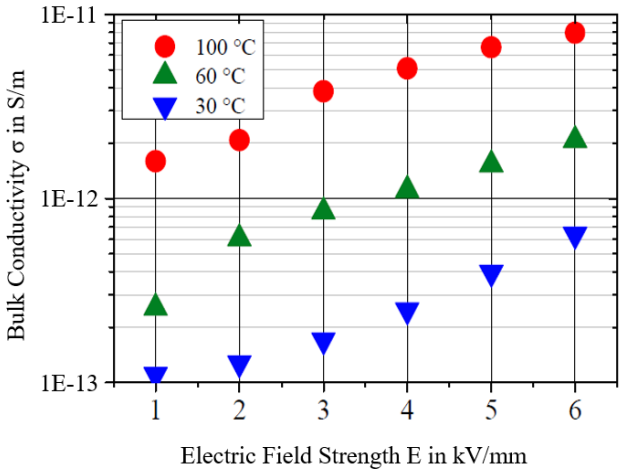

Fig. 3.5. Conductivity characteristics (κ) of Iriotec 7000 filled epoxy [91].

3.3.2 Simulation Results of the Electric Field Distribution

The initially designed spacer model for the reduced scale GIS/GIL test set-up is shown in Fig. 3.6.

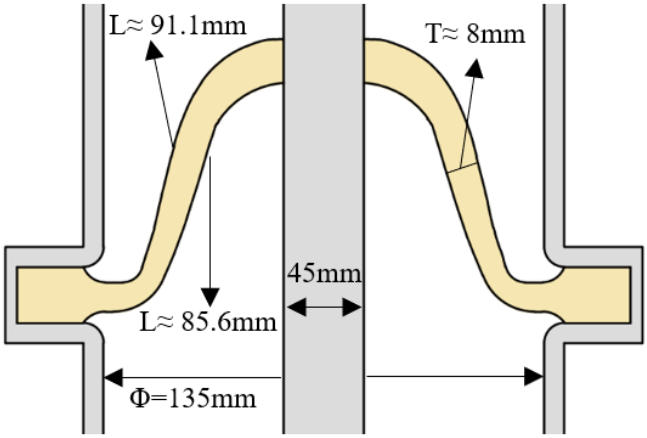

Fig. 3.6. Initial spacer model configuration.

The applied DC voltage was 125.5 kV where the maximum electric field magnitude at the central conductor and the grounded enclosure were 5.57 kV/mm and 1.86 kV/mm respectively, and they were approximately close to those present in the full size 500kV DC gas insulated systems.

To apply a temperature gradient ΔT, the temperature of the high voltage conductor T_c was varied from 30°C to 90°C while the temperature of the grounded

enclosure T_e remains at 30°C which means $T_c=T_e$ (30°C)+ΔT. An example of the temperature distribution is shown in Fig. 3.7 with ΔT=60°C and T_c=30°C+ΔT=90°C by considering the thermal conductivities of the spacer material and the gas corresponding to 1.2 W/mK and 0.0145 W/mK respectively.

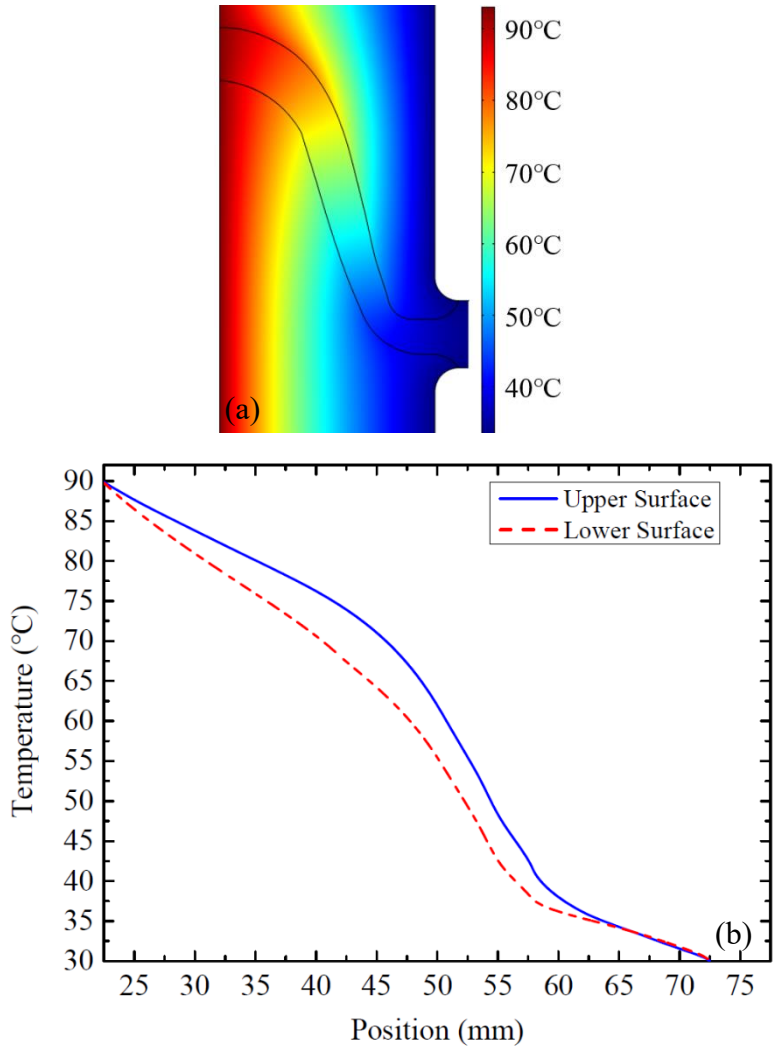

Fig. 3.7. (a) Temperature distribution when T_c=90°C and T_e=30°C. (b) Temperature distribution along the upper and lower surfaces of the spacer.

The results of the electric field distributions around the spacer made of different types of materials under various temperature gradients are given in Fig. 3.8 with a gas conductivity value of 10^{-18} S/m.

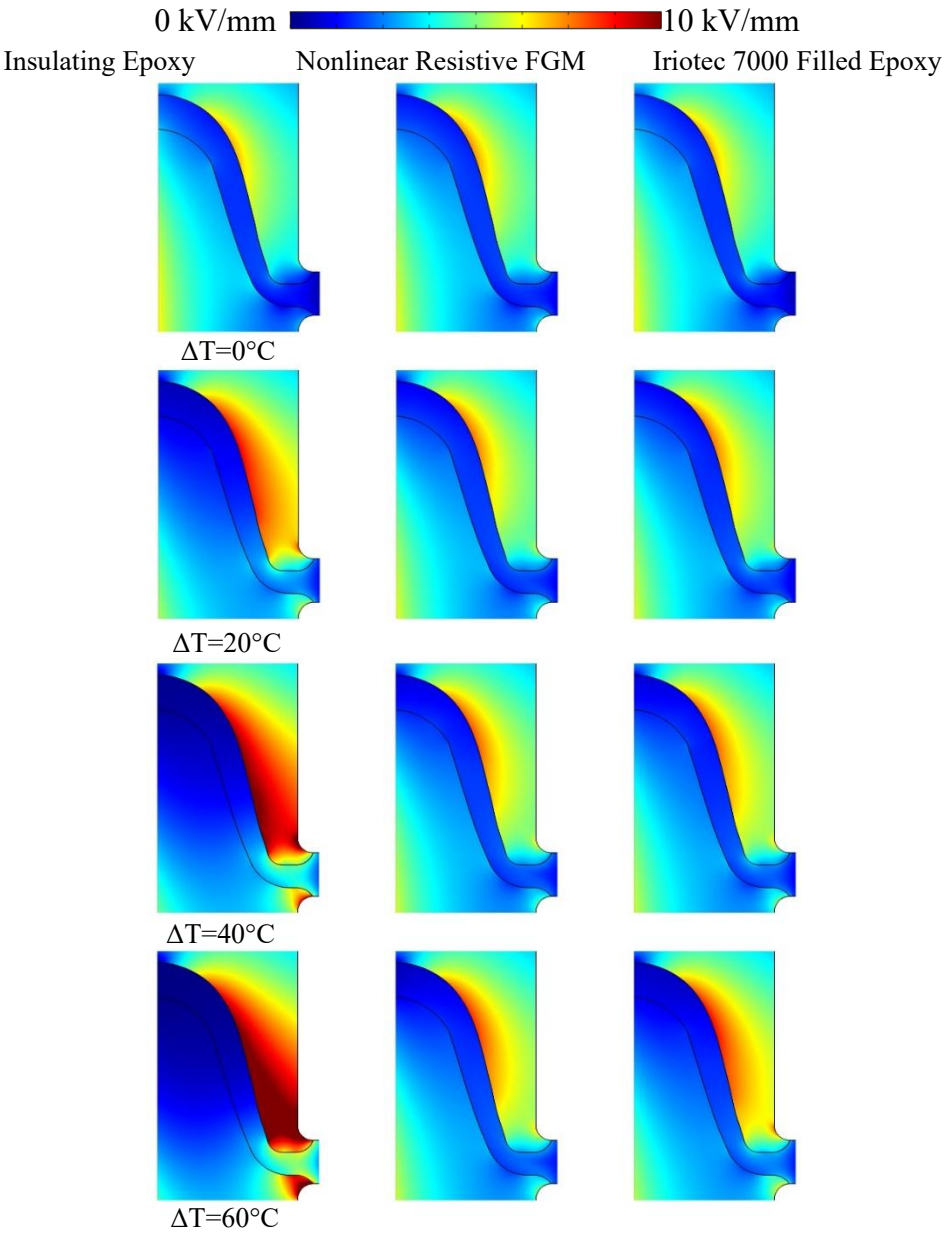

Fig. 3.8. Electric field distributions around the spacer made of different materials with ΔT increase under 125.5 kV with $\sigma_{gas}=10^{-18}$ S/m.

As can be seen on the figure, there is an influence of the temperature gradient increase on the electric field distributions around the spacer for all types of materials. However, a considerable change was observed for the insulating epoxy based spacer where the distribution of the electric field was completely shifted towards the grounded enclosure compared to the uniform temperature case ΔT=0°C. In addition, the electric field was also intensified at the flange's rounded edges where it reached 11.5 kV/mm instead of 3.5 kV/mm at the upper side and 10 kV/mm instead of 2.2

kV/mm at the lower side.

The tangential electric field of the insulating spacer is presented in Fig. 3.9 for different ΔT along both upper (a) and lower (b) surfaces**.** It can be observed that the increase of ΔT led to an intensification of the electric field at the triple junction: grounded flange-spacer-gas. For example, at ΔT=60°C, the maximum electric field reached 8.1 kV/mm at the upper side and 12.4 kV/mm at the lower one respectively.

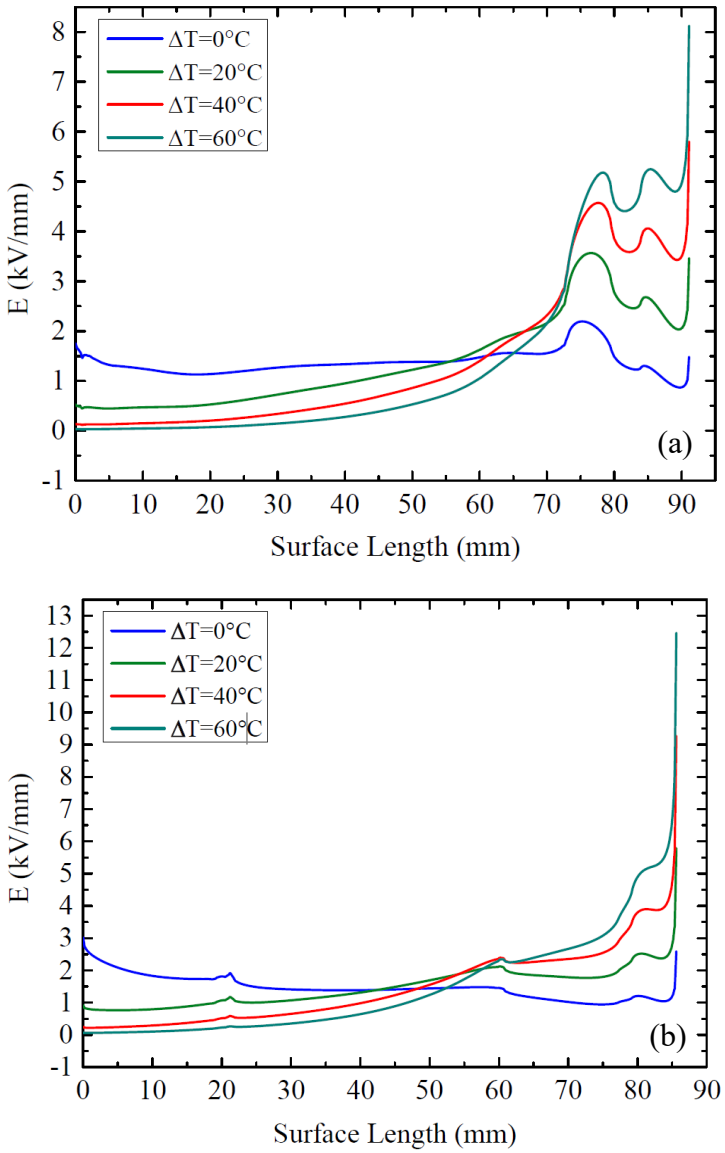

Fig. 3.9. Tangential electric field along the upper (a) and the lower (b) surfaces of the insulating spacer for different ΔT under 125.5 kV.

For the spacers made of nonlinear resistive FGM, irrespective of the linearity (large or moderate), the major differences observed in comparison with the

insulating spacer were that, under high temperature gradient, the electrical field enhancement at the rounded edges of the flange was much improved (see Fig. 3.8) and the tangential electric field along the spacer surface was significantly lowered as shown in Fig. 3.10 for ΔT = 60°C at both upper (a) and lower (b) surfaces respectively. The maximum electric field at the highly stressed triple junctions was considerably reduced in the case when the spacer was made of FGM, from 8.1 kV/mm to 2.6 kV/mm at the upper surface and from 12.4 kV/mm to 2.6 kV/mm at the lower surface.

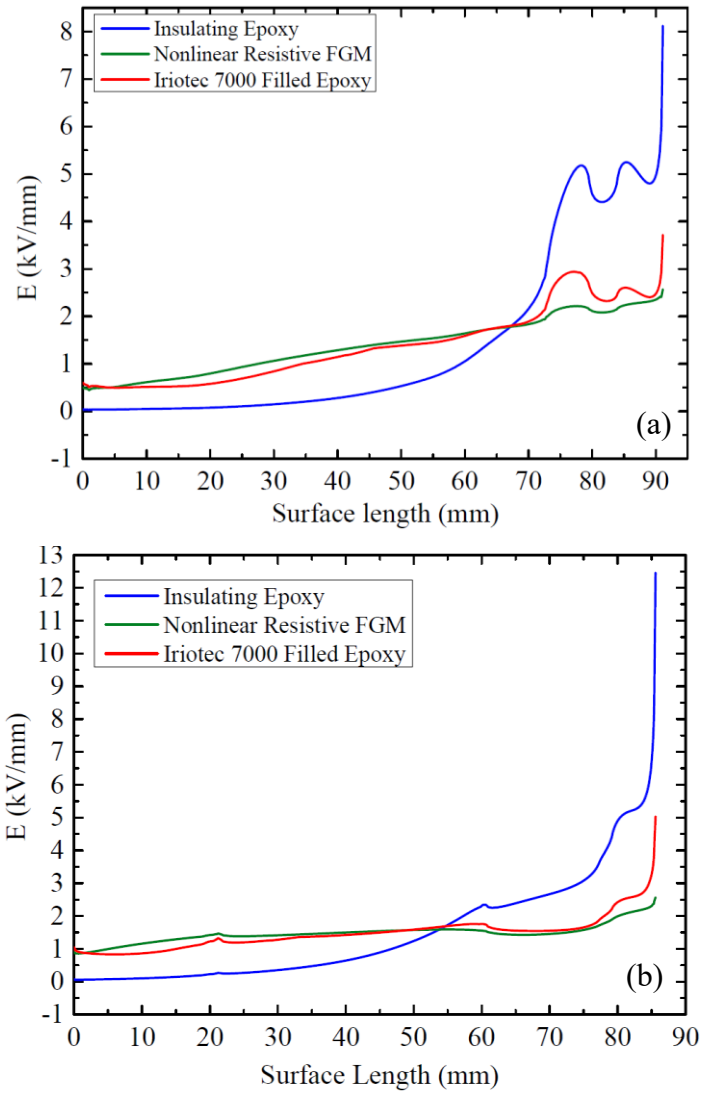

Fig. 3.10. Tangential electric field distribution at the upper (a) and the lower (b) surfaces of the spacer made of nonlinear resistive FGM and Iriotec 7000 filled epoxy in comparison with the insulating material for ΔT = 60°C under 125.5kV.

Furthermore, it is intended from Fig. 3.10, that Iriotec 7000 filled epoxy having a moderate nonlinearity could be enough to control and reduce the enhancement of the electric field at the critical regions instead of the highly nonlinear resistive FGM based on ZnO microvaristors filled epoxy. In addition, the use of Iriotec 7000 filled epoxy performs well under comparison because the fabrication of ZnO microvaristors requires doping with small amounts of other metal oxides and the sintering process is long and should be well controlled.

The numerical simulations have also shown that, when the conductivity of the gas is increased to 10^{-15} S/m, the electric field distributions around the spacer remain unchanged for all types of spacer materials. An example is given in Fig. 3.11 for ΔT=60°C along the upper surface.

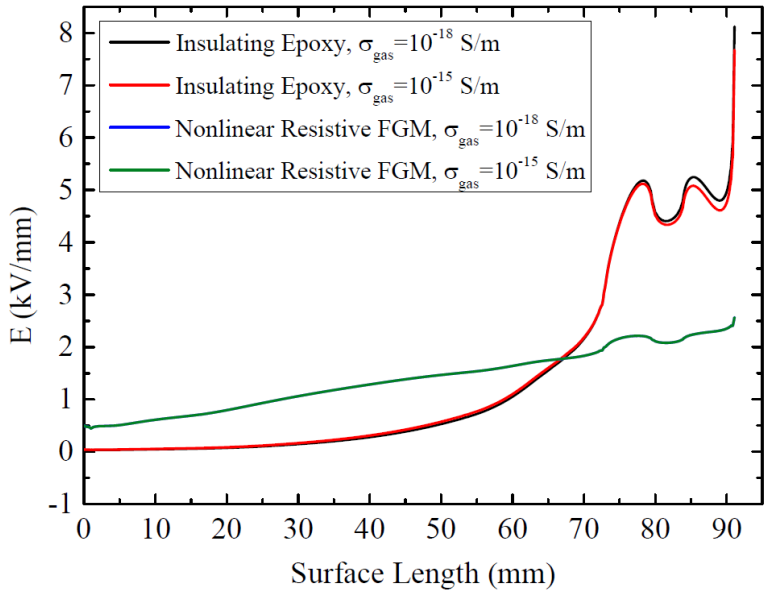

Fig. 3.11. Tangential electric field distribution at the upper surface of the spacer made of the insulating material and nonlinear resistive FGM for ΔT = 60°C under 125.5kV using $\sigma_{gas}=10^{-18}$ S/m in comparison with 10^{-15} S/m.

3.4 Modified Spacer Model and Simulation Results

3.4.1 Spacer's Epoxy-based Material

In this section, three types of epoxy-based materials were investigated:

(i) conventional epoxy resin matrix filled with 60 to 66 wt.% of micro-sized

alumina (Al_2O_3) commonly used in HVAC GIS/GIL systems.

(ii) modified filled epoxy with a lower temperature dependence of the conductivity.

(iii) nonlinear resistive electric field grading material (FGM). Their thermal conductivity corresponds to 0.675 W/mK [92] and the relative permittivity is equal to 5 for (i) and (ii) and to10 for (iii).

The electrical conductivity of the materials is electric field and temperature dependent whose models are described below.

This investigation aims to identify which material type performs better when considering electric field distribution, determined using numerical simulations, in order to select the most appropriate category for the fabrication of DC spacer models and their tests verification in the reduced-scale GIS/GIL.

3.4.1.1 Conventional alumina filled epoxy

Equation (3.13) was used to describe the relationship between the electric field and the conductivity under different temperature gradients for conventional alumina filled epoxy, where the characteristics of the alumina-filled epoxy as function of E and T are shown in Fig. 3.12 with σ_0=19.9 S/m, β=0.08 mm/kV, W_a=0.95 eV and K_B=8.62 x10^{-5} eV/K.

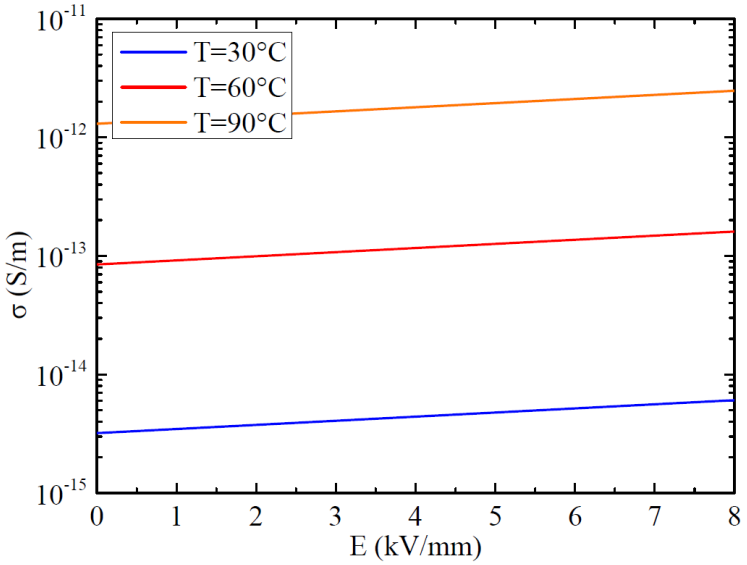

Fig. 3.12. Computing electric field and temperature dependent conductivity of the standard HVAC alumina-filled epoxy.

3.4.1.2 Modified filled epoxy

The modified epoxy-filled material exhibits a lower temperature dependence of the conductivity compared with that of the conventional HVAC alumina-filled epoxy, which is represented by a decreased value of the thermal activation energy Wa in Equation (3.14). Indeed, for the development of HVDC cables, it has been found that improved cross-linked polyethylene (XLPE) based insulating materials with reduced temperature-dependent conductivity is one of the key solutions to obtain a desired electric field distribution compared to conventional HVAC XLPE materials [93]. Therefore, this approach is considered to verify whether the reduced temperature dependence of the conductivity could also be beneficial for the improvement of filled epoxy materials for HVDC GIS/GIL applications.

Practically, such modified epoxy-filled material can be obtained by careful selection and tuning of the constituents of the epoxy material formulation, such as nature of the epoxy base resin, hardener type, catalyst, other additives as well as the type of filler (alumina, silica, etc.), its shape, size, and concentration.

Fig. 3.13 plots the conductivity of the modified-filled epoxy material as function of the electric field at 30 ºC and 90 ºC with σ_0= 3.64×10^{-7} S/m, β=0.08 mm/kV and Wa=0.5 eV together with the conventional alumina-filled epoxy having Wa=0.95 eV. The initial conductivities of both materials are assumed to be equal at 20 ºC and low field.

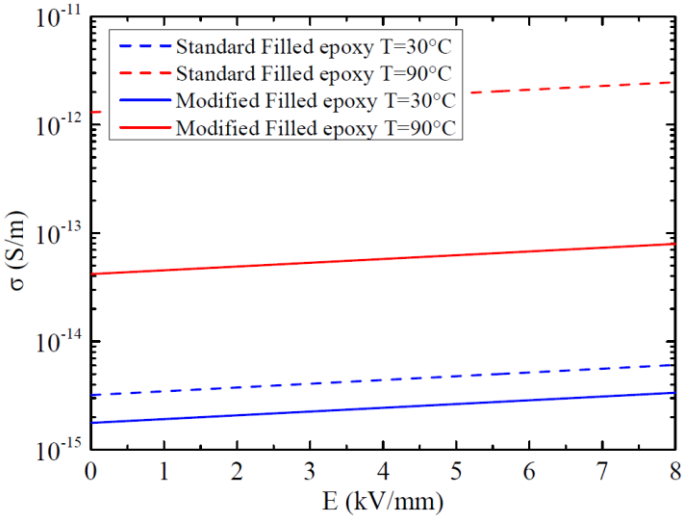

Fig. 3.13. Electric field and temperature dependent conductivity of the standard HVAC alumina-filled epoxy and modified filled epoxy.

3.4.1.3 Nonlinear resistive field grading material

Equation (3.5) was used to describe the relationship between the electric field and the conductivity under different temperature gradients for the nonlinear resistive field grading material. By considering the temperature effect, Equation (3.5) becomes:

$$\sigma_{FGM}(E,T) = \sigma_{o,T} \cdot \exp\left(-\frac{Wa}{k_B \cdot T}\right) \cdot \frac{1+\left(\frac{E}{E_1}\right)^{\gamma-1}}{1+\left(\frac{E}{E_2}\right)^{\gamma-1}} \quad (3.8)$$

Where:

$\sigma_{0,T}$ is the specific conductivity constant (S/m)

Among the different electric field grading materials that have been investigated for use in HVDC GIS/GIL applications and which are still under development, there are: (i) ZnO microvaristor filled epoxy material [91] which has a strong field dependence, or high nonlinearity coefficient ($\gamma > 20$), of its conductivity. However, ZnO microvaristor filler is composed, besides ZnO, of other metal oxides (Bi_2O_3, Sb_2O_3, etc.), requires a well-controlled sintering process at temperatures above 900ºC, and its fabrication is mastered by only few ZnO varistors manufacturers; (ii) epoxy filled with Iriotec 7000 particles (Merck Global) that consist of flake shaped mica particles covered with a nanoscale semiconducting antimony doped tin oxide (ATO) layer [48] and shows a modest nonlinearity where the measured electrical conductivity is in the range [10^{-13}–10^{-11} S/m]; (iii) silicon carbide (SiC)/Al_2O_3 filled epoxy [19].

We are particularly interested in verifying the effectiveness of another novel FGM type having a moderate nonlinearity coefficient ($\gamma<8$) that can be obtained by filling the epoxy resin matrix with two types of fillers (n/p doped semiconducting SiC with conducting/semiconducting bridging particles) namely doped SiC/CB (carbon black) or doped SiC/ATO. It should be noted that doped SiC/CB mixed into a rubber matrix was employed for electric field control in commercial HVDC cable accessories [94], [95]. Such novel type of epoxy-based FGM has a nonlinear resistive conductivity σ_{FGM} (E, T) behavior that can match approximately the theoretical one illustrated in Fig. 3.14 where $\sigma_{0,T}=3.83\text{x}10^{-3}$S/m, E_1=1 kV/mm,

E_2=5 kV/mm, W_a=0.5 eV, γ= 6.

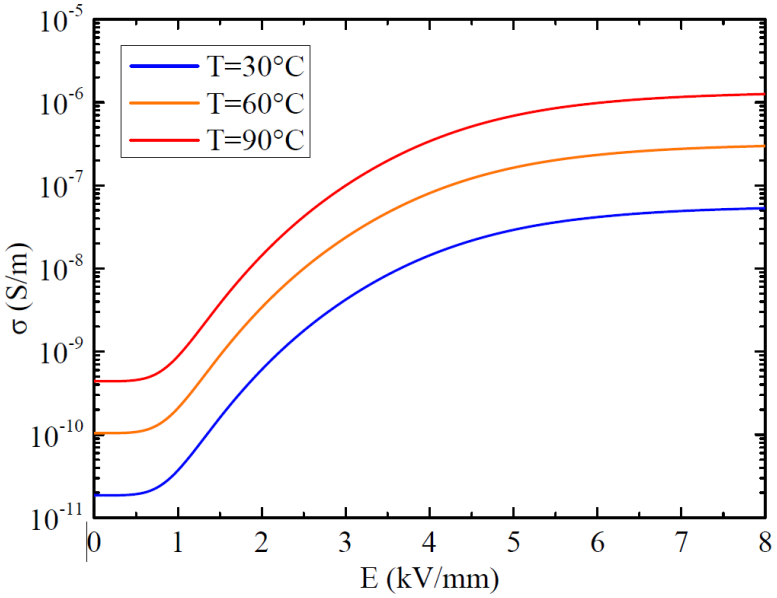

Fig. 3.14. Conductivity of novel nonlinear resistive field grading material (FGM) with temperature and electric field having a moderate nonlinear coefficient γ = 6.

3.4.2 Optimization of DC Spacer Shape

In order to obtain the desirable shape of the spacer model enabling local electric field enhancements at the critical regions to be avoided under DC voltage, the following optimization criteria were considered:

A minimum value of electric field magnitude at both the HV and the ground triple junctions (spacer-gas-HV conductor/grounded flange interface).

- Minimises the normal component of electric field on the spacer surface in order to minimize surface charge accumulation as recommended in [96].
- Sufficient creepage distance to prevent surface flashover caused by a high electric field.
- Minimized field enhancement along the spacer surface.

To fulfil these requirements, the geometrical modifications that have been carried out with respect to the initial shape and the flange are shown in Fig. 3.15, and they are as follows:

(1) Increasing the spacer thickness (T) at the HV conductor contact to reduce

the electric field at the HV triple junction.

(2) Introducing a small gas gap (g) at the spacer-flange interface to lower the electric field at the ground triple junction.

(3) Increasing the radius (R) of the flange corner.

(4) Varying the radius (r) of the spacer edge near the ground side.

(5) Increasing the spacer inclination angle (θ) to lower the normal component of the electric field and, hence, minimize the surface charges accumulation.

(6) Varying the distance (s) between the end of the flange radius and the spacer.

It is worth mentioning that modifying the contact condition between the grounded flange and the epoxy spacer by the introduction of a gas gap (g) [62] and increasing the spacer inclination angle (θ)have been found [97] to be effective in avoiding local electric field intensification under DC voltage application.

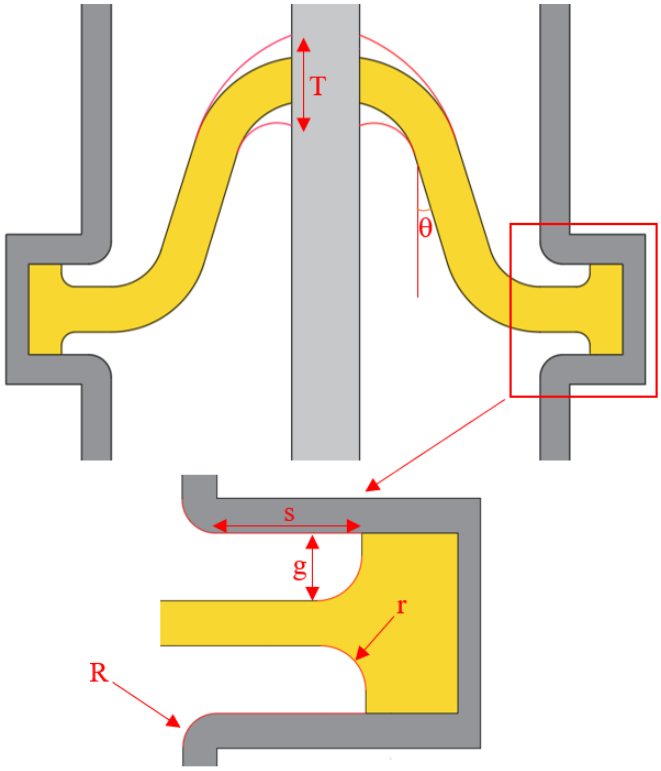

Fig. 3.15. An illustration of the geometrical parameters' variables (T, θ, g, s, r, R) for the spacer model optimization.

The geometrical optimization of the spacer model has been undertaken under uniform temperature set to $T_c=T_e=30ºC$. The spacer is made of conventional HVAC alumina-filled epoxy having the electrical conductivity characteristics as shown in Fig. 3.12.

The optimization procedure has been developed without the use of any mathematical optimization algorithm but according to the following steps: (i) the selected geometrical controllable parameters (R, g, s, T, r, θ) were varied over the indicated given ranges in Table. 3.1; (ii) the electric field distribution along the spacer is calculated under DC voltage energization; (iii) the electric field distribution is analyzed by verifying whether it matches the targeted requirements. The final obtained optimized values are indicated in Table. 3.1.

Table. 3.1. Controlled geometrical parameters and final optimized values. *Note that sharp edges of the flange and the spacer are described by R=0 mm and r=0 mm respectively.*

Geometrical parameter	Initial value	Variation range	Optimized value
Flange radius (R)	0 mm	0-15 mm	15 mm
Gas gap (g)	0 mm	0-5 mm	5 mm
Distance (s)	0 mm	0-8 mm	4 mm
Thickness (T)	10 mm	10-25 mm	23 mm
Radius (r)	0 mm	0-5 mm	5 mm
Inclination angle (θ)	17º	17º, 45º, 60º	60º

The resulting optimized configuration is illustrated in Fig. 3.16, and the obtained results of its electric field distributions (tangential, normal, and total) are illustrated in Fig. 3.17(a) for the upper surface of the spacer and Fig. 3.18(a) for the lower surface of the spacer in comparison with those of the initial spacer profile presented in Fig. 3.17(b) and Fig. 3.18(b).

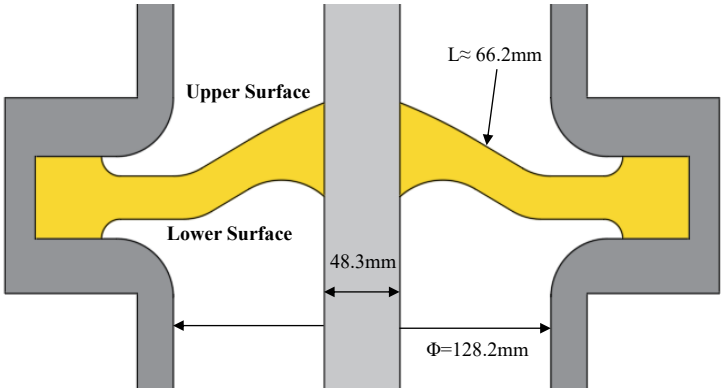

Fig. 3.16. Optimized shape of the spacer model for DC energization.

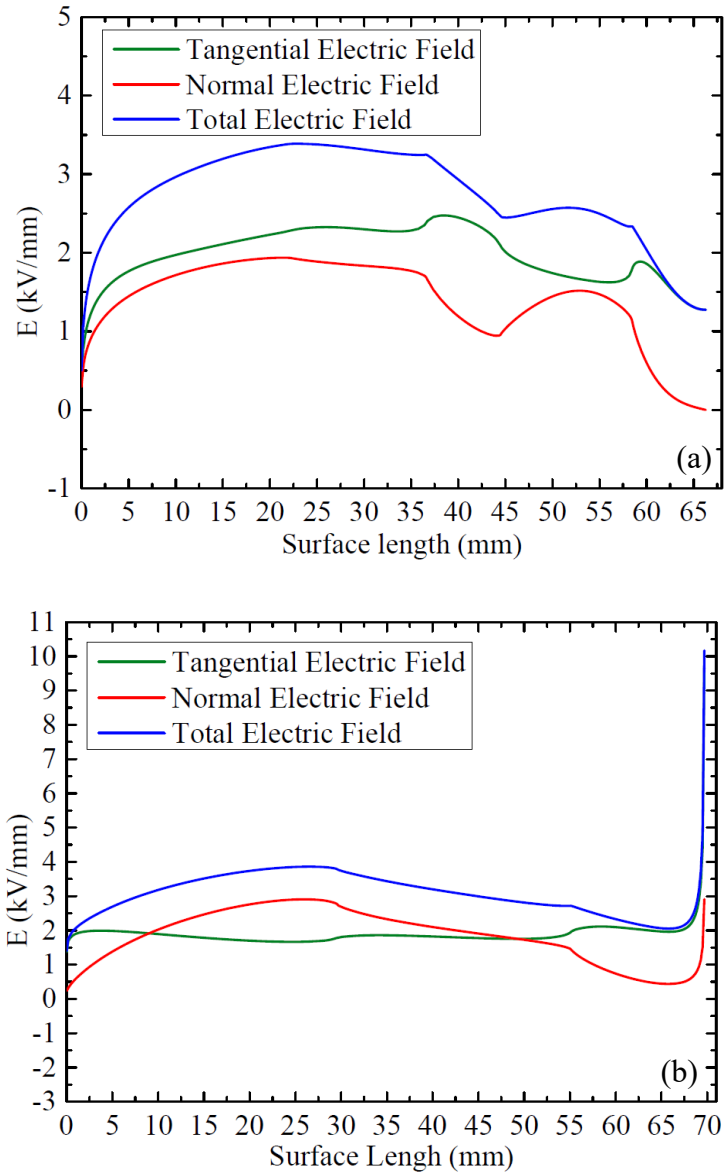

Fig. 3.17. Results of the tangential, normal, and total electric field distributions on the upper surface of the optimized spacer (a) in comparison with that of the initial configuration (b).

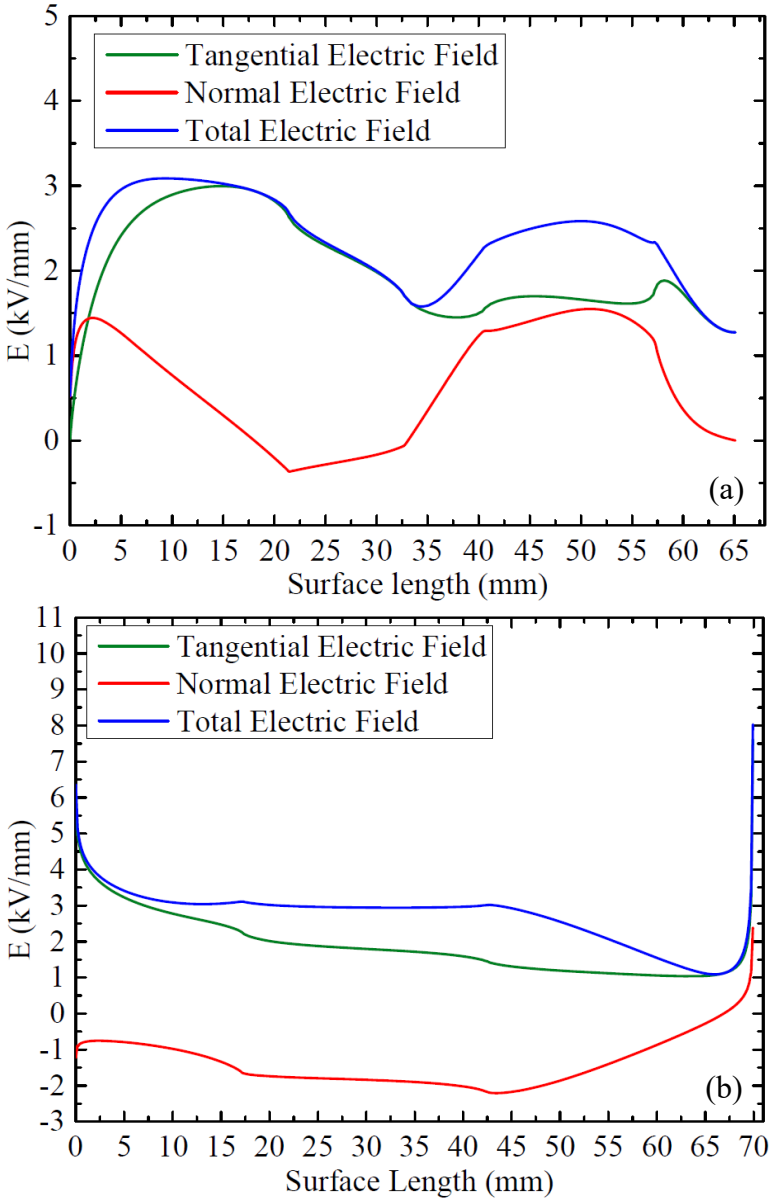

Fig. 3.18. Results of the tangential, normal, and total electric field distributions on the lower surface of the optimized spacer (a) in comparison with that of the initial configuration (b)

As can be seen in Fig. 3.17(b) and Fig. 3.18(b) of the spacer's initial profile, the maximum electric field values at both upper and lower surfaces occur at the critical ground triple junction (gas-spacer-grounded flange) and are 10 kV/mm at the upper side and 8 kV/mm at the lower side which exceeds the maximum applied electric value of 5.03 kV/mm at the inner conductor. However, the maximum electric field of the improved optimized spacer is not located at the critical ground triple junction and is much lower with 3.4 kV/mm at the upper surface side and 3.2 kV/mm at the

lower one (Fig. 3.17a and Fig. 3.18a). At the ground triple junction, the maximum electric field is 1.2 kV/mm and is lower than the ground applied electric field of 2.09 kV/mm. Furthermore, the maximum value of the normal component of the electric field which is responsible for surface charge accumulation is about 3 kV/mm for the initial shape whilst it is 2 kV/mm for the optimized one.

3.4.3 Effects of Spacer's Material and Temperature Gradient on the Electric Field Distribution

To account for the load conditions of the DC GIS/GIL, the temperatures of the HV conductor T_c and the grounded flange T_e were set to 90 ºC and 50 ºC respectively with a temperature gradient ΔT=40 ºC. The temperature distribution around the optimized spacer model is shown in Fig. 3.19.

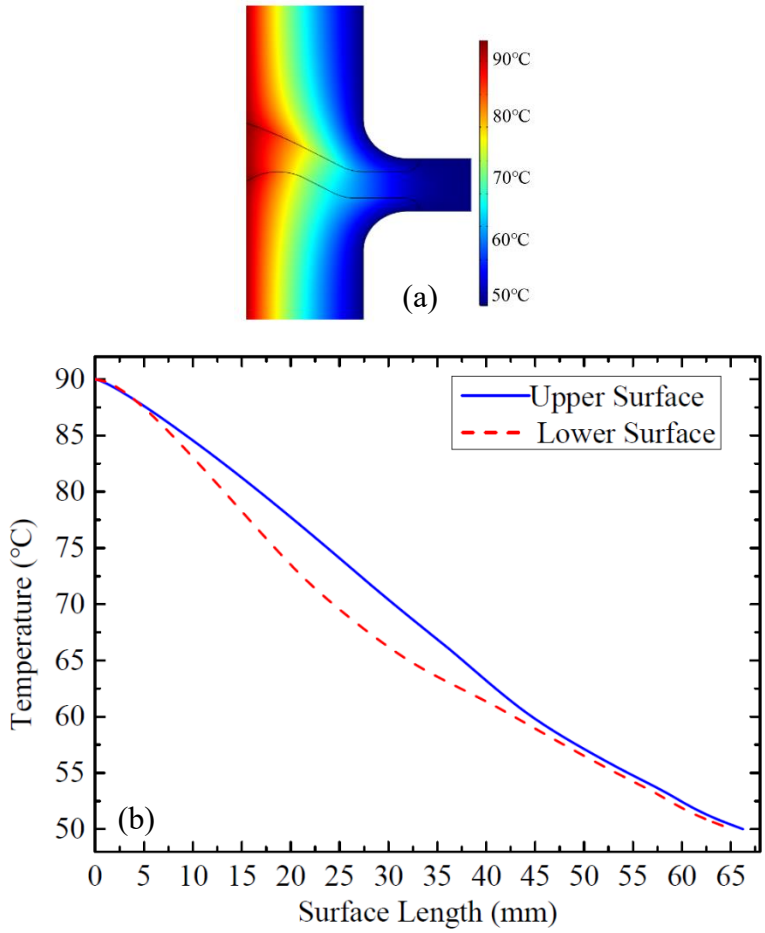

Fig. 3.19. (a) Temperature distribution around the optimized spacer model with T_c=90°C and T_e=50°C. (b) Temperature distribution along the upper and lower surfaces.

The results of the electric field distributions around the optimized spacer made of different types of epoxy-based materials at uniform temperature (30 ºC) and in the presence of a temperature gradient of 40 ºC are given in Fig. 3.20.

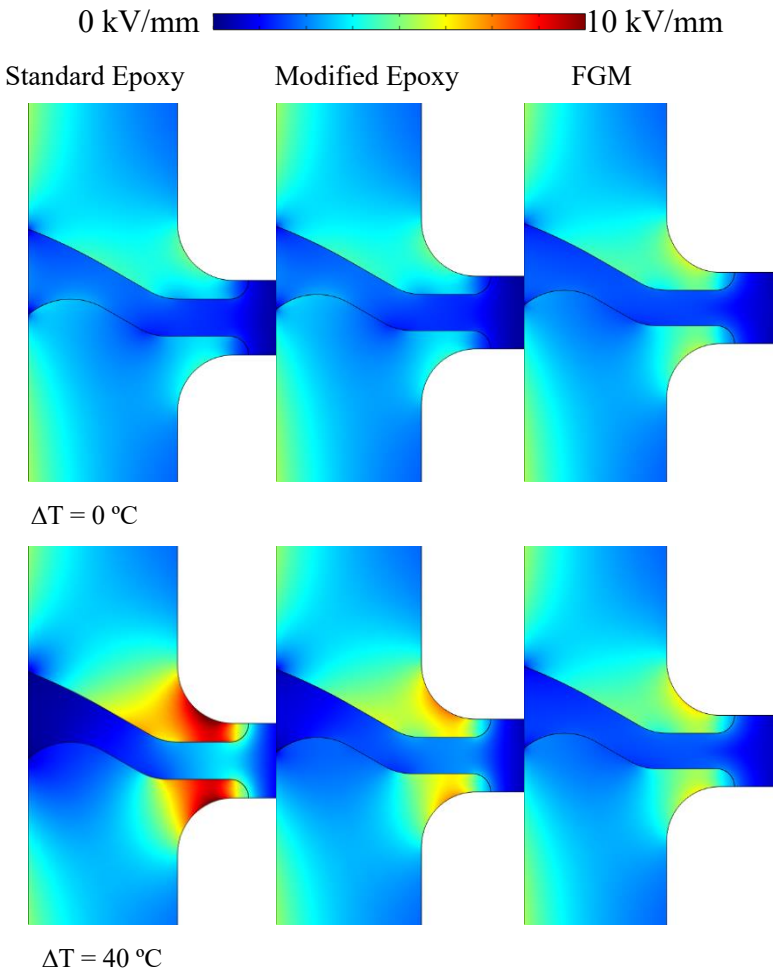

Fig. 3.20. Electric field distributions around the spacer model made of different materials at uniform temperature (T = 30 ºC) and ΔT = 40 ºC under DC voltage of 131.3 kV.

As can be seen in Fig. 3.20, there is an influence of the temperature gradient on the electric field distribution around the spacer for all types of materials where the distribution of the electric field is shifted towards the grounded flange compared to the uniform temperature case ΔT=0°C. It is important to note that such phenomenon of electric field redistribution towards colder regions where the electrical conductivity is lower than the one of the warmer regions near the HV conductor, is well known when HVDC GIS/GIL are under load operation.

However, a significant increase of the electric field is observed for the

conventional HVAC alumina-filled epoxy. Furthermore, it is worth noting that the electric field is also intensified at the flange's rounded edges where it reaches 11.5 kV/mm instead of 3.5 kV/mm at the upper side and 10 kV/mm instead of 2.2 kV/mm at the lower side.

The total electric field E_{total} distributions along the upper surface of the optimized spacer model made of AC standard alumina filled epoxy material, modified filled epoxy material and FGM, are presented in Fig. 3.21(a) and (b) for uniform temperature (ΔT=0 ºC) and temperature gradient (ΔT=40 ºC) respectively under DC voltage of 131.3 kV.

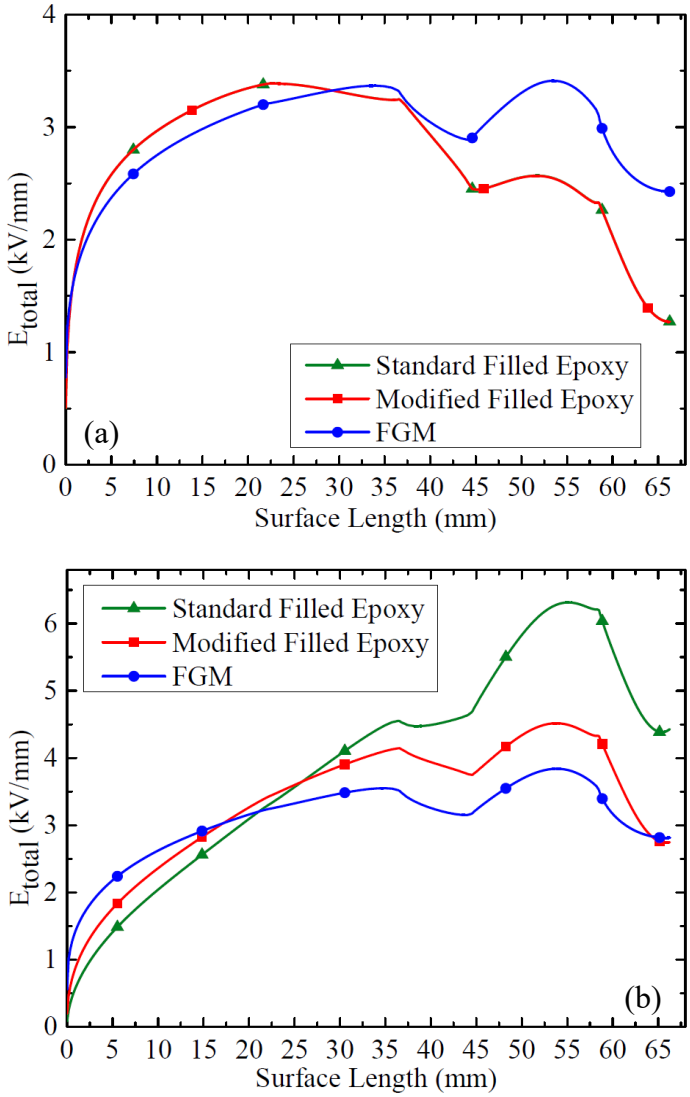

Fig. 3.21. Total electric field distribution at the spacer's upper surface under 131.3 kV DC for ΔT=0 ºC (a) and ΔT=40 ºC (b) of standard HVAC alumina filled epoxy, modified filled epoxy and FGM.

Under a uniform temperature of 30 ºC (Fig. 3.21(a)), the obtained electric field distributions for the standard alumina-filled epoxy and the modified filled epoxy material have similar magnitudes, as shown in Fig. 3.13, both materials have the same weakly electric field-dependent conductivity (β=0.08 mm/kV), and the conductivity difference at 30º C for both materials is low. Moreover, for FGM, although the maximum value of the total electric field remained unchanged, the electric field at the ground triple junction is 2.4 kV/mm compared to the other two materials where it is 1.2 kV/mm, and this may be caused by the moderate nonlinearity coefficient γ of the material.

In the presence of a high temperature gradient (ΔT=40 ºC), as can be seen in Fig. 3.21(b), the most relevant finding is that the use of modified filled epoxy material, which has a reduced temperature dependence on the conductivity, represented by a lower thermal activation energy (W_a=0.5 eV) compared with the conventional alumina-filled epoxy having W_a=0.95 eV, results in a significant reduction of the electric field enhancement. Compared with the standard alumina-filled epoxy, the maximum value of the total electric field is decreased from 6.5 kV/mm to 4.5 kV/mm without exceeding the maximum applied conductor electric field of 5.03 kV/mm. Furthermore, the electric field at the critical ground triple junction is lowered from 4.5 kV/mm to 2.8 kV/mm. To determine the stability of the model, during the Mesh in the pre-processing stage, the triangular elements were refined into extreme fine ones when the surface of the spacer was decomposed into non-overlapping triangular elements, thereby improving the accuracy of the simulation results. The electrical field enhancement at the rounded edges of the flange is much improved too (Fig. 3.20). The FGM having a low nonlinearity coefficient, does not add any further minimization of the electric field at the critical ground triple junction.

3.4.4 Surface Charge Accumulation

The steady-state accumulated charges on the spacer surface can be calculated directly from the obtained electric fields by using Gauss's law as follows:

$$\rho_S = \varepsilon_0 \varepsilon_G E_{GN} - \varepsilon_0 \varepsilon_I E_{IN} \tag{3.19}$$

where ε_G is the relative permittivity of the gas, ε_I the relative permittivity of the spacer material and ε_0 the permittivity of vacuum. E_{GN} and E_{IN} are the normal components of the electric field in the gas side and the spacer side respectively.

Fig. 3.22 presents the accumulated charge along the spacer's surface under stationary DC applied voltage of 131.3 kV at uniform temperature of 30 ºC (ΔT=0 ºC) and thermal gradient of ΔT=40 ºC between the central conductor and the flange respectively, for standard AC alumina filled epoxy, modified filled epoxy and FGM. As can be seen, positive charges accumulate on the whole surface of the spacer, because according to the COMSOL electric field calculations and Equation (3.19), the obtained normal electric field component at the gas side E_{GN} is highest where the electrical conductivity is very low (10^{-18} S/m) and that, at the spacer side, E_{IN} is negligible.

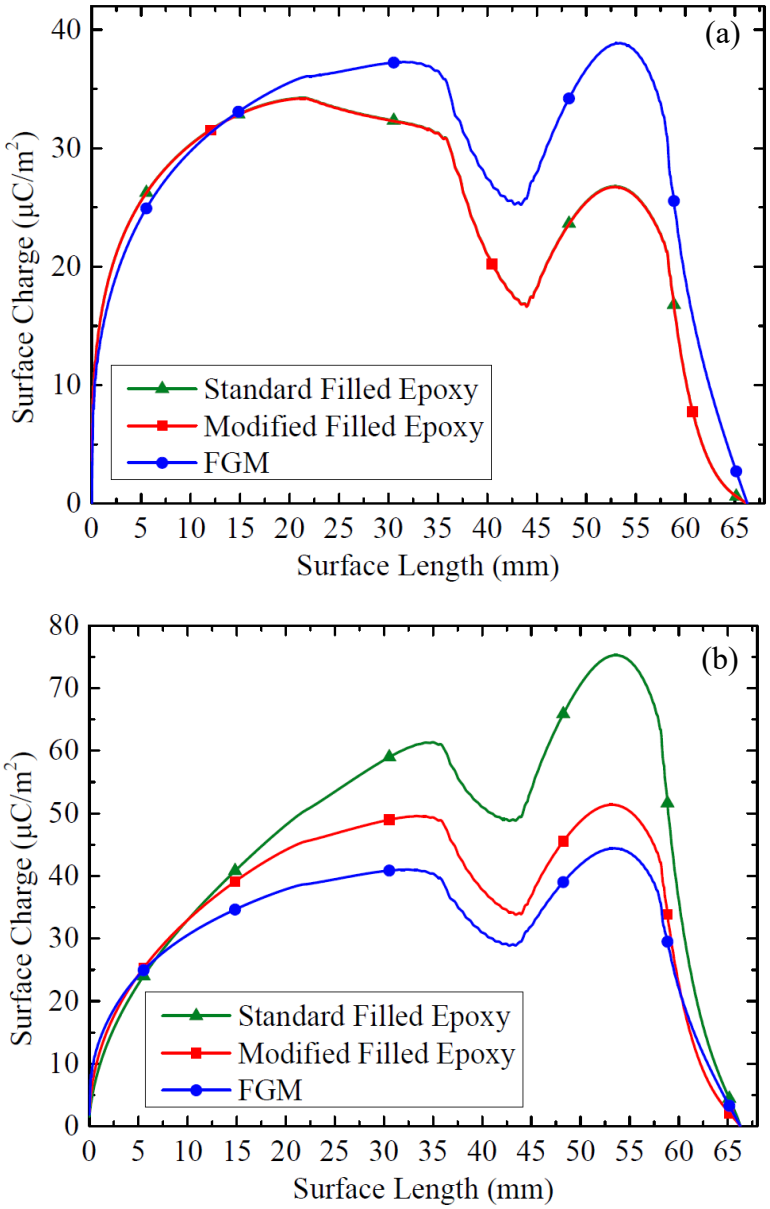

Fig. 3.22. Accumulated charges at the spacer's upper surface under 131.3 kV DC for ΔT=0 ºC (a) and ΔT=40 ºC (b) of standard filled epoxy, modified filled epoxy and FGM.

Under uniform temperature distribution, the maximum surface charge density was 34.2 μC/m^2 for both standard AC alumina filled epoxy and modified filled epoxy since they had the same weak electric field-dependent conductivity and 38.9 μC/m^2 for FGM. However, for ΔT=40 ºC the surface charge density increased for the three materials (Fig. 3.22b). Such impact of temperature gradient on surface charge accumulation on spacers has been also obtained in the thermo-electrical simulation investigation of the work by Zhou et.al. [98] on insulators in 500 kV

DC-GIL.

The most significant increase is seen with the standard AC alumina filled epoxy material exhibiting a higher temperature-dependent electrical conductivity (W_a=0.95 eV) where the maximum surface charge density is more than two times larger (75.3 μC/m^2) than without thermal gradient (34.2 μC/m^2). The surface charge density of modified filled epoxy, which has a weaker temperature-dependent electrical conductivity (W_a=0.5 eV), is reduced with a value of 51.4 μC/m^2 and of FGM is 44.4 μC/m^2. This indicates that a weak dependence of the electrical conductivity with temperature is very effective in reducing surface charges formation under DC energization and thus modified filled epoxy should be used in HVDC GIS/GIL spacers.

3.5 Conclusion

Several researchers have conducted investigations concerning the influence of spacer shape under DC applied voltage, surface charge accumulation, and novel material for spacers, but the modification is quite simple, and without the test verification. In this work, the optimized DC spacer model was tested on a reduced-scale GIL prototype for experimental verification, and the results are presented in Chapter 6. The main outcomes of this work can be summarized as follows:

- For HVDC GIS/GIL applications, the temperature gradient between the high voltage conductor and the grounded enclosure has a big influence on the electric field distribution around the spacers under stationary DC voltage
- Nonlinear resistive field grading materials (FGM) are very effective to lower the electric field enhancement at the critical regions
- Iriotec 7000 filled epoxy FGM having a moderate nonlinearity seems to be an interesting material candidate compared to the highly nonlinear ZnO microvaristors-filled epoxy
- The increase of the gas conductivity from 10^{-18} S/m to 10^{-15} S/m does not change the distribution of the electric field along the spacer made of the investigated different materials

- The geometrically optimized spacer model profile for DC operation is very effective in reducing the enhancement of the electric field at the critical locations where the resulting maximum electric field along the spacer is within the acceptable/permissible range.
- The presence of a high temperature gradient has a significant influence on the electric field distribution along the spacer and shifts the maximum electric field from the central HV conductor towards the grounded flange side. One of the key mitigations to reduce this electric field enhancement is by using new modified filled epoxy material having a weakly temperature-dependent conductivity, namely a lower thermal activation energy than that of the conventional AC alumina-filled epoxy.
- The increase of temperature gradient leads also to charge accumulation increase on the spacer surface with the highest surface charge density when using AC standard material.
- Novel nonlinear resistive field grading material (FGM) having a moderate nonlinearity coefficient ($\gamma < 8$) is also effective but does not add further improvement.
- Once the spacer profile had been initially well optimized for DC energization, the use of modified filled epoxy may be sufficient for 500 kV DC GIS/GIL applications provided that the maximum temperature gradient (ΔT) during load operation is not very high.

Chapter 4 Characteristics for HVDC GIS/GIL Spacer under DC Superimposed Lightning Impulse Voltage Conditions

4.1 Introduction

Due to the problems of electrical insulation and discharge under extreme conditions of ultra-high voltage and superimposed lightning impulse voltage, the current research mainly focuses on the normal working state of the gas insulated systems under HVDC voltage. The simulation and experiment results are affected by the factors such as applied voltage, polarity, spacer shape, insulating material characteristics[6][99][100]. However, it lacks the working state of spacers under DC superimposed lightning impulse voltage condition, including changes in the characteristics of insulating materials, safety assessment for the gas-insulated system. Research on the discharge process of gas-insulated systems under HVDC applied voltage including streamer breakdown theory, but this is only concentrated normal working condition under HVDC applied voltage and lacks the discharge results under extreme condition such as DC superimposed lightning impulse voltage and polarity reversal[101]. At the same time, due to the difference in the micro-reaction including elastic collisions, ionization, electron- positive ion recombination, excitation, electron-impact reactions of different insulating gases, the discharge mechanism on the surface of the spacer is also different. Traditional discharge tests IEC 60270 are mainly to investigate the number of discharge pulse, discharge magnitude, and macroscopic indicators such as electromagnetic waves, light, and sound radiated during the discharge process[102][103]. However, it is difficult to describe microscopic changes such as the surface discharge movement on spacers, the accumulation of positive and negative ions, and the directional movement of ionized particles, and the accumulation of electric charges on the surface generates built-in field, which generates further excitation and ionization, affecting the safe operation of the equipment. Therefore, it is necessary to use simulation calculations to carry out theoretical research under DC superimposed lightning voltage, which is conducive to the microscopic discharge understanding of processes and mechanisms.

In order to provide a reliable HVDC GIS/GIL spacer design, superimposed impulse tests are also required on the system energized over a long period of time by HVDC voltage to evaluate the dielectric strength of the spacer. Therefore, it is

necessary to evaluate the electric field distribution on the surface of the spacer under DC superimposed lightning impulse voltage. In this section, a finite element model combining steady-state and transient solvers was used to simulate the electric field distribution and space charge distribution in a gas-insulated system under DC superimposed lightning impulse voltage, which revealed the ion transportation law under lightning excitation. Based on the conventional spacer material after the shape optimization as discussed in Chapter 3.4, the results under steady state condition to initialize the physical fields before lighting was applied, and the general form partial differential equations were established to construct the electric field-temperature-ion concentration equations under DC superimposed lightning voltage. The change of the electric field distribution, ion concentration, charge density and other parameters around the spacer was discussed after the lightning impulse voltage was superimposed, which provided the theoretical basis to the safety, standardization, and design of the future gas insulated system.

4.2 Methodology and Governing Equations

The simulation was conducted by synthesizing the Gauss theorem, Fourier heat transfer theory and ion conservation equations, considering both the dependence of spacer electrical conductivity on electric field and temperature, and constructing a dynamic feedback mechanism between the positive and negative ion concentration and electric field distribution through the Poisson's equation. First of all, the current density and electric field distribution provided by steady state condition are set as the heat source for heat transfer and the initial value of the electric field and temperature under lightning impact. Then, the electric field and temperature under electrostatic condition and heat transfer were calculated coupled with the spacer conductivities and heat. In order to simplify the simulation, the current was not considered because the discharge is relatively mild and did not have strong current. Due to electric field redistribution and temperature diffusion under DC superimposed lightning impulse voltage, positive ions will migrate to the negative electrode, and negative ions will migrate to the positive electrode. At the same time, the change of surface charge accumulation and ion transportation affect the electric

field distribution around the spacer based on the charge conservation equation using a time dependent solver.

When GIS/GIL is subjected to a DC superimposed lightning impulse voltage, a large amount of charge accumulates at the positive and negative electrodes. Also, the space charge density, electric field and ion concentration are redistributed. The electrostatic governing equations are as follow:

$$div\vec{D} = \rho_v \tag{4.1}$$

$$\vec{D} = \varepsilon_0 \varepsilon_r \vec{E} \tag{4.2}$$

Where:

$\vec{D}$ is the electric flux density (C/m^2)

ρ_v is the space charge volume density (C/m^3)

ε_0 is the permittivity of vacuum (F/m)

ε_r the relative permittivity (1)

Since the conductivity of the spacer's material was depended on the temperature, to obtain the electric field distribution, the temperature distribution must be first determined. For calculation simplification, it was assumed that the heat transfer process occurred by thermal conduction through both the gas and the spacer under steady sate conditions according to the equation:

$$div(kgrad(T)) = Q \tag{4.3}$$

where:

k is the thermal conductivity (W/(m·K))

The temperatures at the grounded enclosure T_e, and at the high voltage conductor T_c were set constants and did not exceed the maximum allowable temperatures under operation.

Unlike in DC steady-state conditions, when DC superimposed lightning impulse voltage is present, the temperature of the insulator is solved by transient equation: T_2. As an independent variable, T_2 reflects the transient temperature field change.

$$\rho C_p \frac{\partial T_2}{\partial t} + div(-kgradT_2) = 0 \quad (4.4)$$

Where:

ρ is the density of insulating material (kg/m^3)

C_p is the volume heat capacity under constant pressure (J/(kg·K))

T_2 is the temperature (K)

Under steady state conditions, there are a certain number of free ions in equilibrium. When encountering the impact of lightning pulse, the electric field and the number of carriers increase significantly. To simplify the simulation, the initial concentration of positive and negative ions was assumed to be equal and the influence of electronic participation in transmission was ignored, with the value of 5×10^{16} 1/m^3 which is below the streamer propagation concentration [104]. The dynamic change of negative and positive ions concentrations can be described by generation, recombination, and motion of positive and negative ions as follows[105]:

$$\frac{\partial N_p}{\partial t} = S - RN_pN_n - div\left(N_p\mu_pE - D_pgradN_p\right) \quad (4.5)$$

$$\frac{\partial N_n}{\partial t} = S - RN_pN_n - div(-N_n\mu_nE - D_ngradN_n) \quad (4.6)$$

Where:

S is the gas generation rate (30 Ion pairs(*IP)*/(cm^3·s))

R is the gas recombination rate (3.4×10^7 cm^3/s)

N_p, N_n are the concentration of positive and negative ions (5×10^{16} 1/m^3)

μ_p, μ_n are the mobility of positive and negative ions (0.08 cm^2/(V·s))

D_p, D_n are the diffusion coefficient of positive and negative ions (m^2/s)

The diffusion coefficient of the charge carriers is related to the mobility via Einstein relation. The spatial charge distribution is determined by the net charge of positive and negative ions.

$$D_{p,n} = \frac{k_BT_2}{e_0}\mu_{p,n} \quad (4.7)$$

$$\rho_v = \left(N_p - N_n\right)e_0 \tag{4.8}$$

Where:

e_0 is the elementary charge (C)

k_B is the Boltzmann constant (eV/K)

ρ_v is the spatial charge density (C/m^3)

As the flux flowing out of the boundary, the emission current participates in the conservation relationship of ion charge, and its value has a significant dependence on the spatial electric field strength, as shown in Equation (3.11) [105]:

$$e_0(N_p\mu_p E - D_p\nabla N_p)\cdot \mathbf{n} = j_{emitted} \tag{4.9}$$

The emitted current can be calculated by the following equation[105]:

$$j_{emitted} = \frac{j_0 e^{1.8\vec{E}}}{e_0} \tag{4.10}$$

Where:

j_0=12.5 pA/m^2

Equation (4.10) indicates that the emitted boundary current density is in an extremely low because the gas mixture in the GIL/GIS is hard to ionize and the mobility of positive and negative ions is low electric field strength, and when $|E|$ exceeds the ionization E strength of the insulating gas, $j_{emitted}$ will suddenly increase. For instance, the knee point of ionization E strength can be fitted according to the experimental results by adjusting the exponent parameter.

It should be noted that for the conductor, the positive value means that the current is emitted. The dependence of the emission current on the electric field strength is shown in Fig. 4.1.

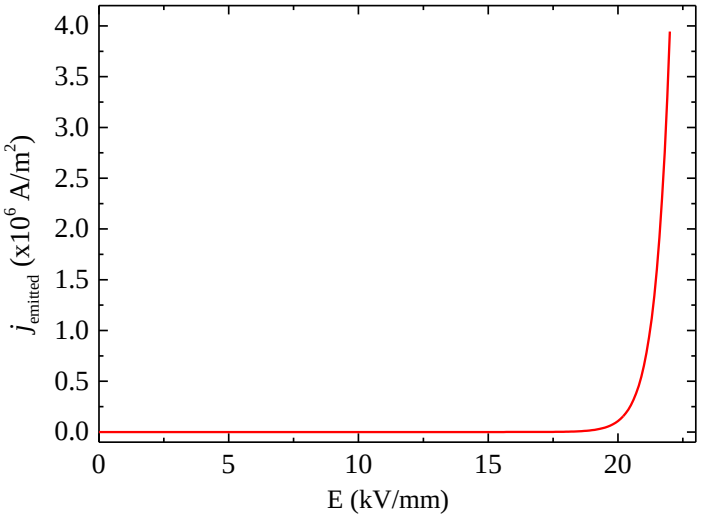

Fig. 4.1. Relationship between the emission current and the electric field.

4.3 Simulation Results

4.3.1 Electric Field Calculation Under DC Superimposed Lightning Impulse Voltage

Three working conditions (see shapes in Fig. 4.2) were conducted: DC superimposed same polarity lightning impulse voltage, DC superimposed opposite polarity lightning impulse voltage, and only lightning impulse applied voltage as shown in Fig.4.2. The distribution of the tangential electric field intensity on the surface of the spacer, the change of the maximum electric field intensity and the time dependence with lightning impulse voltage were investigated. It is worth noting that a standard lightning impulse voltage (1.2/50 μs) with the amplitude 358 kV of positive polarity is applied to HV electrode.

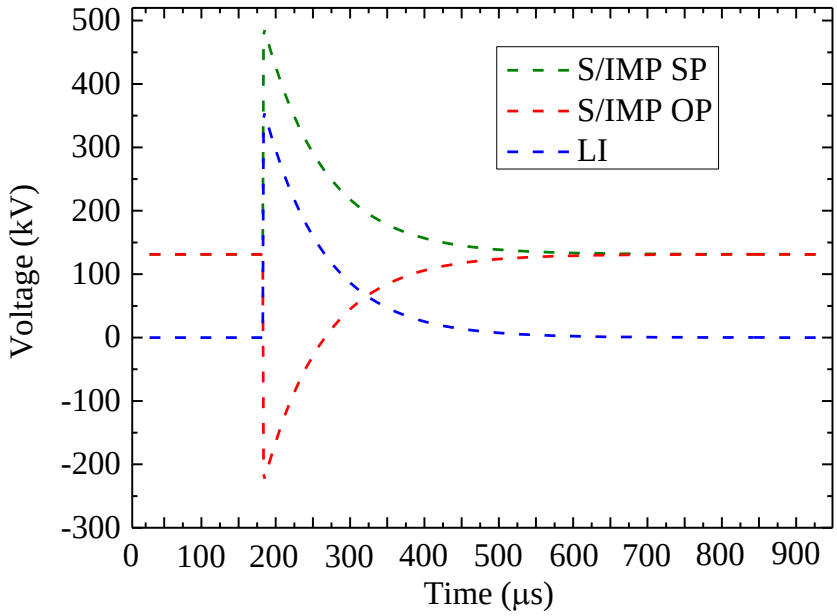

Fig. 4.2. Illustration of lightning impulse voltage and DC superimposed lightning impulse voltage (S/IMP SP: DC superimposed same polarity lightning impulse voltage, S/IMP OP: DC superimposed opposite polarity lightning impulse voltage, LI: Only lightning impulse applied voltage).

The tangential electric field distribution evolution under DC superimposed same polarity lightning impulse voltage is shown in Fig. 4.3. The *x*-axis is the surface length (from positive to negative) of the spacer surface. The *y*-axis is the time evolution process, and the start, development, and stability stages correspond to 2μs, 25μs, and 50μs respectively. From the viewpoint of time evolution, Fig. 4.3(a) demonstrates that the electric field of spacer upper surface reached a peak value of 11.1 kV/mm at the beginning of superimposed lightning impulse voltage, and then rapidly decayed, which was consistent with the trend of the lightning impulse waveform as shown in Fig. 4.2. From the viewpoint of spatial distribution, the tangential electric field reached a peak near the conductor, and then gradually decreased, almost returning to a stable working state near the enclosure. Fig. 4.3(b) presented a similar pattern of the tangential electric field distribution on the lower surface of the spacer, but the electric field intensity was higher, with a peak value of 13.8 kV/mm which may be attributed to the influence of the electrical conductivity distribution and structure of the spacer. Due to the vertically similar distribution of conductivity within the spacer, the upper and lower surfaces showed similar tangential electric field distribution, while the higher electric field amplitude on the lower surface can be attributed to the larger radius of curvature.

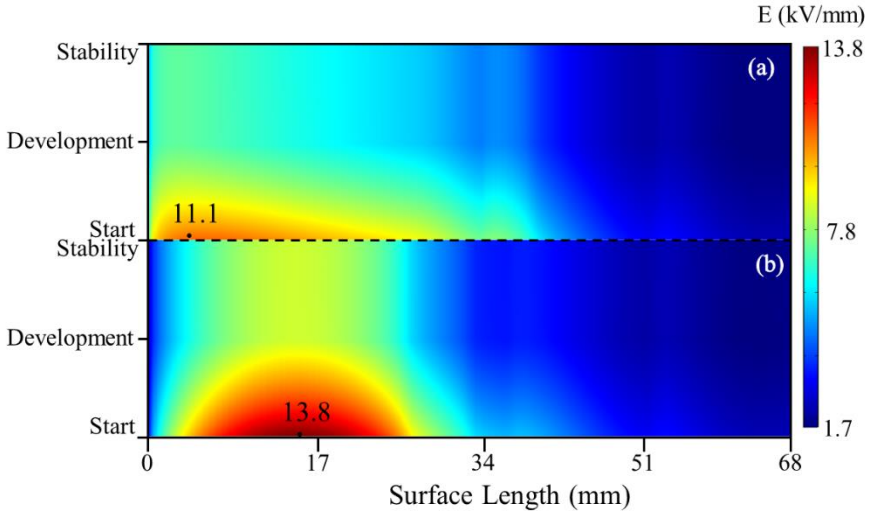

Fig. 4.3. Tangential electric field under DC superimposed same polarity lightning impulse voltage (a) upper surface (b) lower surface. Start, development, and stability stages correspond to 2μs, 25μs, and 50μs respectively.

The tangential electric field distribution evolution under DC superimposed opposite polarity lightning impulse voltage is shown in Fig. 4.4. From Fig. 4.4 (a) and Fig. 4.4(b) the tangential electric field presented a reverse negative distribution, and the amplitude was reduced. The highest tangential electric field on the upper surface was 6.1 kV/mm, and 8.1 kV/mm on the lower surface. It is worth noting that compared with DC superimposed same polarity lightning impulse voltage, although the electric field follows the same trend, the electric field distribution was flatter along the surface of the spacer and more intensive with the increase of time.

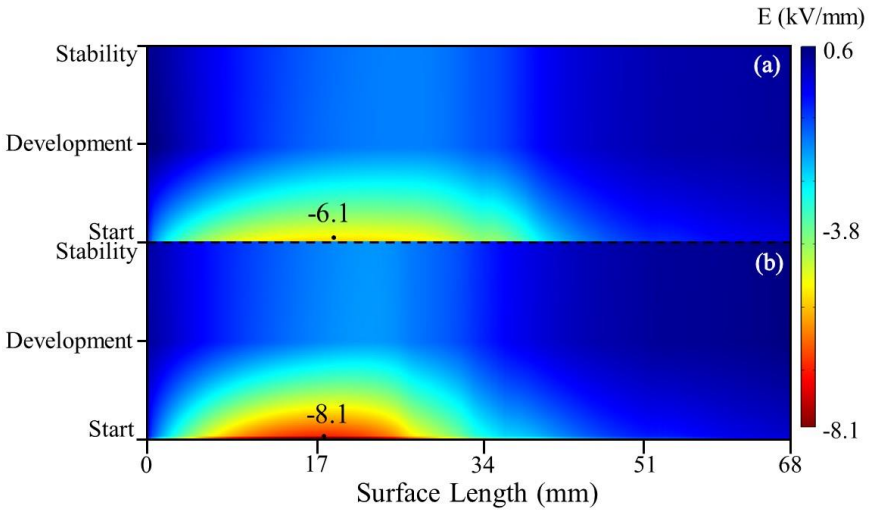

Fig. 4.4. Tangential electric field under DC superimposed opposite polarity lightning impulse voltage (a) upper surface (b) lower surface. Start, development, and stability stages correspond to 2μs, 25μs, and 50μs respectively.

Fig. 4.5 shows the tangential electric field distribution evolution under lightning impulse voltage. The amplitude of the tangential electric field on the upper surface of the spacer was 7.9 kV/mm, and 10.3 kV/mm on the lower surface. Both appeared in the initial stage and then gradually decreased, tending to be stable.

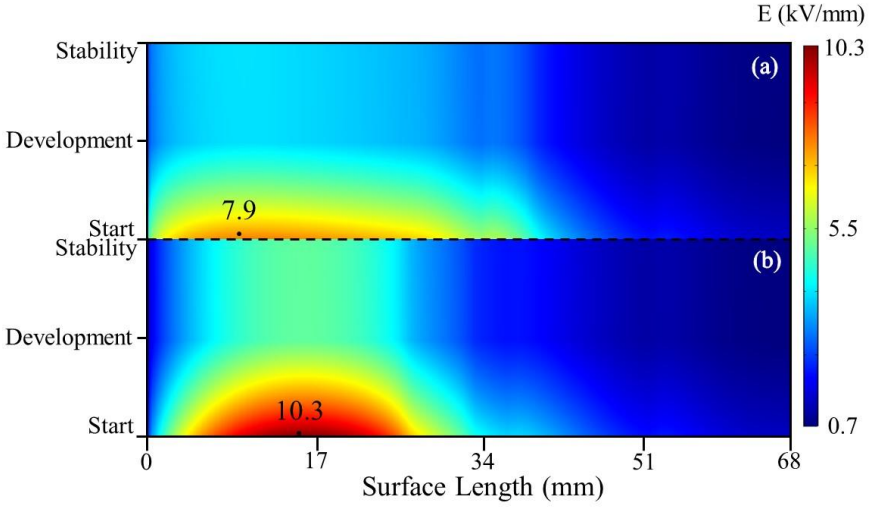

Fig. 4.5. Tangential electric field under lightning impulse voltage (a) upper surface (b) lower surface. Start, development, and stability stages correspond to 2μs, 25μs, and 50μs respectively.

The tangential electric field under DC superimposed same polarity lightning

impulse voltage is shown Fig. 4.6. As can be seen, the tangential electric field increased first and then decreased along the *x*-axis direction. The amplitude of the lower surface electric field was slightly higher than that of the upper surface. At the same time, both surfaces presented a decreasing trend with the development of the lightning impulse, and the electric field intensity was the largest at the beginning. In the electric field distribution on the upper surface of the spacer in Fig. 4.6(a), there were fluctuations at 3 mm, 37 mm, and 57 mm, respectively. The main reason is that, on the one hand, there were curvature changes at 3 mm, 37 mm, and 57 mm on the upper surface, which further accumulated space charges and locally increased the electric field distribution, and on the other hand, under the influence of the lightning impulse voltage, the tangential electric field suddenly decreased, presenting a fluctuation. The tangential electric field on the lower surface was higher, showing a similar trend while the volatility was not obvious.

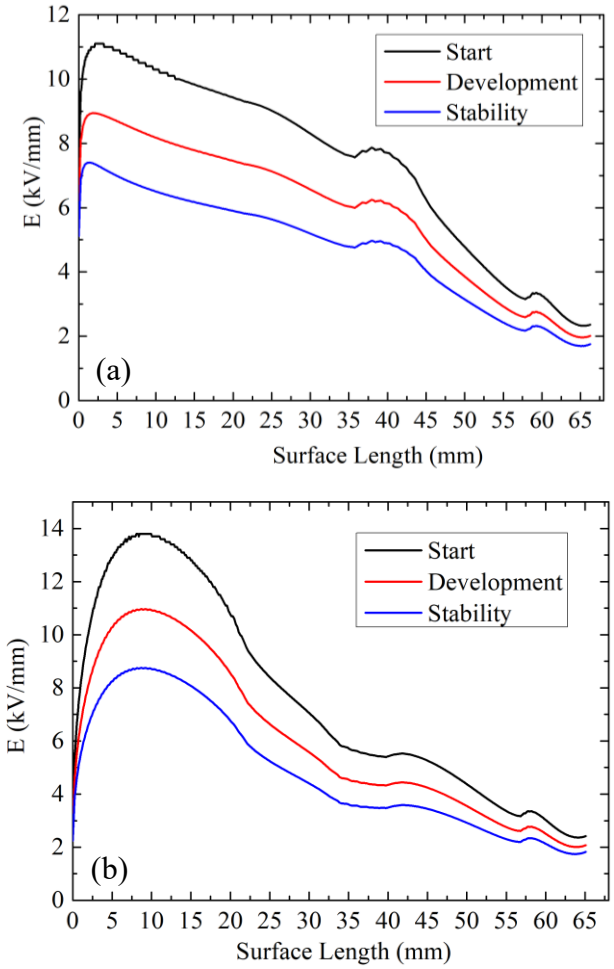

Fig. 4.6 Tangential electric field distribution under DC superimposed same polarity lightning impulse voltage (a) upper surface (b) lower surface.

Fig. 4.7 shows the tangential electric field distribution under DC superimposed opposite polarity lightning impulse voltage. Unlike the superimposed same polarity condition, the amplitude was lower, but showed the same trend. It is worth noting that the change of the tangential electric field was smoother, and there was no obvious fluctuation at the curvature changing area, which was due to the decrease of the electric field.

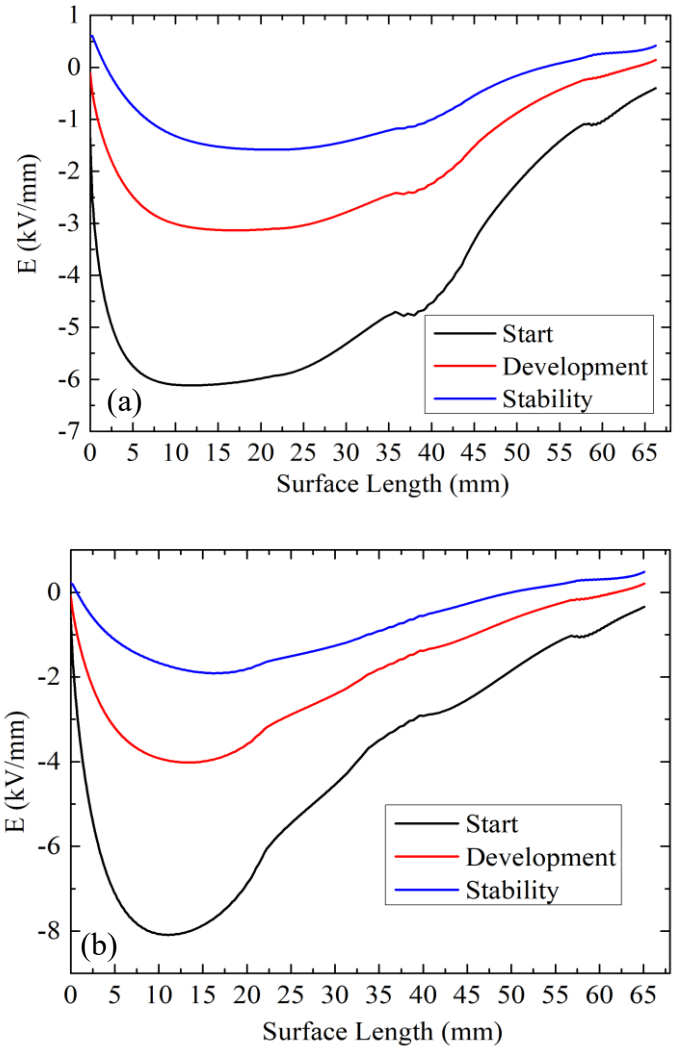

Fig. 4.7. Tangential electric field distribution under DC superimposed opposite polarity lightning impulse voltage (a) upper surface (b) lower surface.

Fig. 4.8 shows the tangential electric field distribution under lightning impulse voltage. As can been seen from the figure, the tangential electric field of the spacer increased first and then decreased along the spacer. The lower surface had a higher

amplitude with the value 10.3 kV/mm, and the tangential electric field on the upper surface changed smoothly. During the whole process, the electric field distribution showed a consistent change trend, while the upper surface showed obvious fluctuations at 37 mm due to the inconsistent radius of curvature, which led to the re-arrangement of charges. Compared with the DC superimposed same polarity lightning impulse voltage condition, the electric field strength was lower, and the amplitude was 7.9 kV/mm, because there was no steady-state charge accumulation effect.

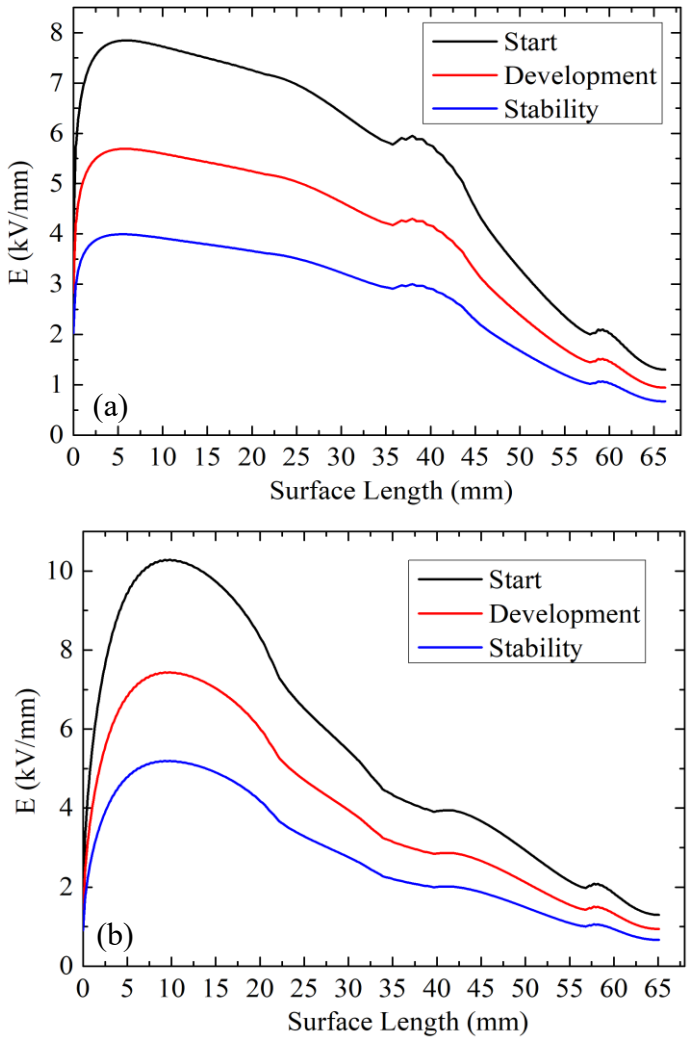

Fig. 4.8. Tangential electric field distribution under lightning impulse voltage (a) upper surface (b) lower surface.

Fig. 4.9 shows the tangential electric field distribution at the beginning under three different conditions. The tangential electric field presented the same trend of

increasing first and then decreasing under all three conditions. At the same time, compared with Fig. 4.9(a), the electric field density on the lower surface changed drastically, and the amplitude was higher. Under lightning impulse voltage and DC superimposed same polarity lightning impulse conditions, local electric field enhancement fluctuations were found at 37mm and 57mm on the upper surface, due to the change of the curvature change of the spacer. The lower surface showed a similar trend, although since the electric field was slightly higher than that on the upper surface by 2kV/mm and the speed of change was more severe, the fluctuation was not obvious.

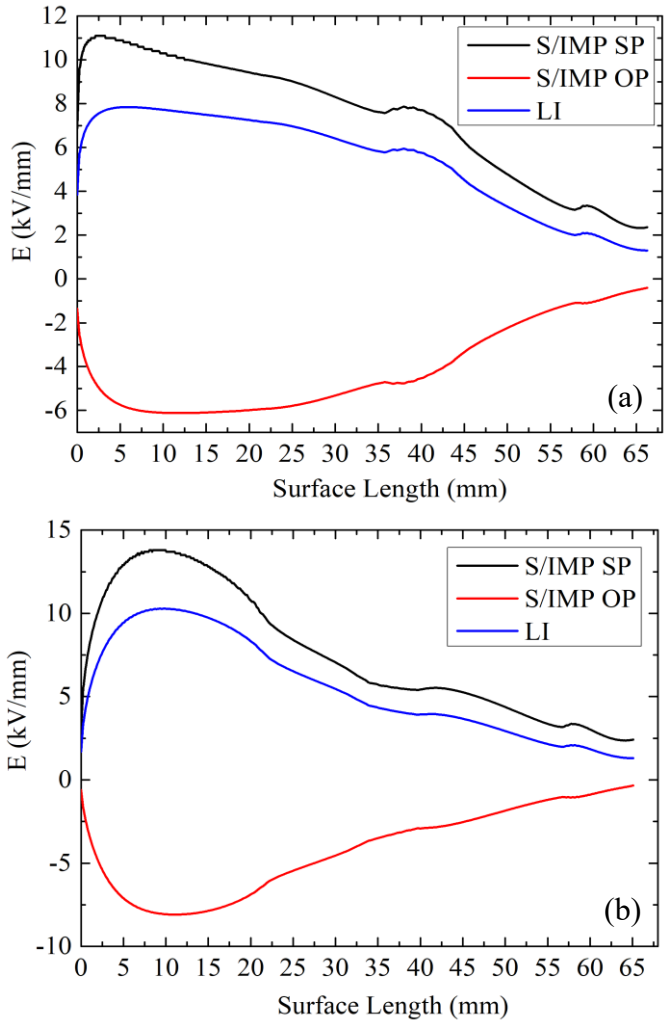

Fig. 4.9. Tangential electric field distribution at the beginning stage under three conditions (a) upper surface (b) lower surface(S/IMP SP: DC superimposed same polarity lightning impulse voltage, S/IMP OP: DC superimposed opposite polarity lightning impulse voltage, LI: Only lightning impulse applied voltage).

Fig. 4.10 shows the maximum tangential electric field under three conditions varying with time. When the lightning impulse voltage was at the beginning stage, the electric field intensity on the surface of the spacer reached its maximum, with value on the upper surface 11.1 kV/mm 6.1 kV/mm and 7.9 kV/mm, and on the lower surface, 13.8 kV/mm 8.1 kV/mm and 10.3 kV/mm respectively. During the period within the range of 0-50μs in Fig. 4.10, corresponding to the development stage of the lightning impulse voltage, the pulse function decayed rapidly, and the maximum electric field intensity gradually decreased. It is worth noting that under DC superimposed opposite polarity lightning impulse voltage condition, the maximum tangential electric field decreased rapidly after the beginning stage, which was due to the lightning impulse voltage function. The lightning impulse was in the stable stage after 50μ, and the maximum tangential electric field on the surface of the spacer remained almost unchanged.

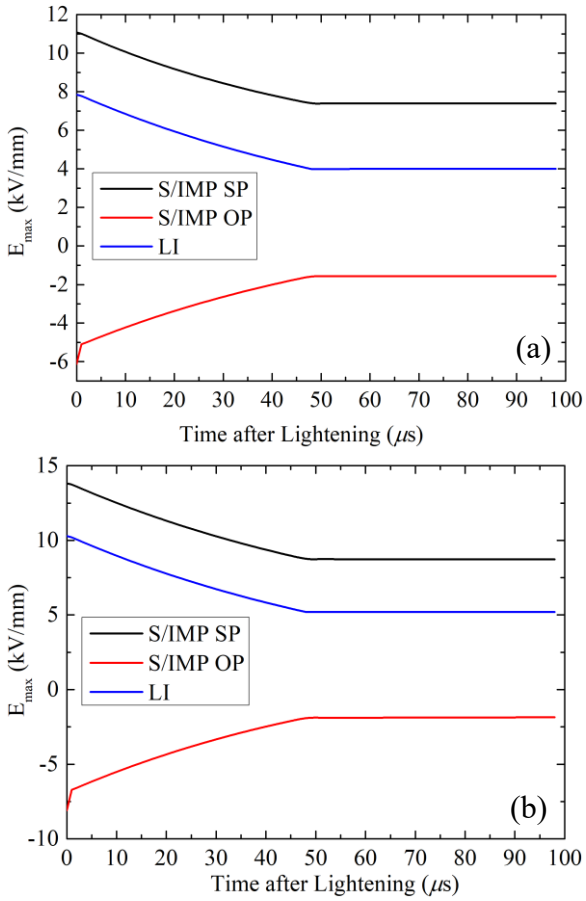

Fig. 4.10. Maximum tangential electric field under three conditions varying with time since the start of the initial waveform (S/IMP SP: DC superimposed same polarity lightning impulse voltage, S/IMP OP: DC superimposed opposite polarity lightning impulse voltage, LI: Only lightning impulse applied voltage).

4.3.2 Ion Density Distribution

The electric field driven movement caused by Coulomb force, and diffusion effects caused by concentration gradient are dominant reasons to determine the distribution of ion pattern as formulated in Equation (4.5) and Equation (4.6). Based on equation (4.7) and the electric field on the surface of the spacer, the ion diffusion coefficients were calculated as shown in Fig. 4.11. The left side was the ion diffusion coefficient of the upper and lower surfaces of the spacer, and the right side was the electron mobility. In this study, to simplify the simulation, a constant electrical mobility was used for positive and negative ions as the input parameter, with a value of 0.08 $cm^2/(V.s)$ [105]. The computed results shown that the ion diffusion coefficient gradually decreased along the surface of the spacer, which was mainly determined by the temperature distribution.

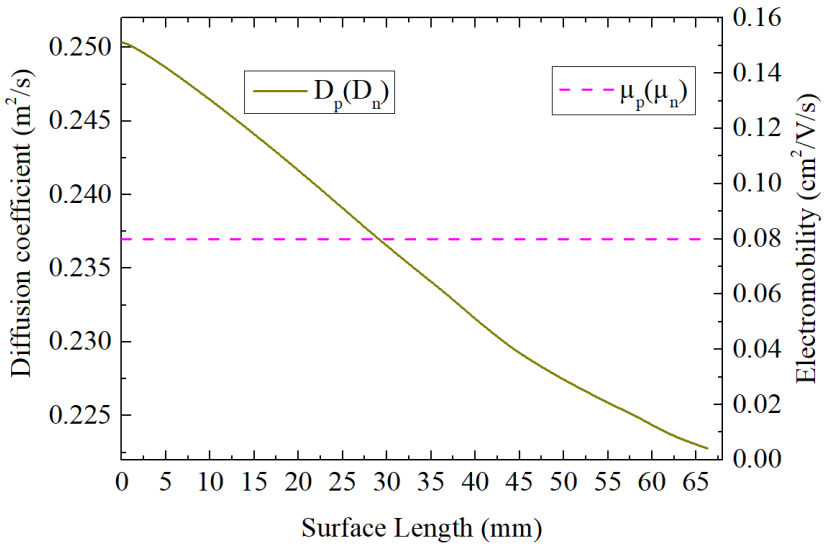

Fig. 4.11. Diffusion coefficient and electron mobility of ions on the surface of the spacer.

The ion density under DC superimposed same polarity lightning impulse voltage on the surface of the spacer is shown in Fig. 4.12, where the solid line is for positive ions N_p, and the dashed line is for negative ions N_n. It can be observed from the figure that positive ions showed an increasing trend, while negative ions decreased. This was mainly due to the ions driven by electric force, and the N_p migrated to the enclosure, with the highest value of ion density 1.85×10^{17} $1/m^3$, while N_n accumulated on the conductor in the opposite direction, with the highest value of

ion density 6.54×10^{17} $1/m^3$. It is worth noting that the lightning impact may distort the time and spatial distribution of ion density as shown in the inset figure of Fig. 4.12, that is, a cross point appears nearby the enclosure where N_p at development stage suddenly grows and exceeds that of start and stability stages because of the synergism effect of rapid growth rate and electric enhancement. The ion density around the spacer is shown in Fig. 4.13. It is thought that the main reasons of the cross point were: (i) The migration and diffusion of the density of positive and negative ions were comprehensively affected by many factors: When the ion concentration was not high, it was difficult to change linearly due to the constraints of the temperature and electric field distribution; (ii) When the positive and negative ions moved in opposite directions, they were attracted by the Coulomb force of the nearby moving ions, and part of them accumulated or deviated, and slight fluctuations occurred due to collective behaviour. The movement was still in the direction of the current density. The arrows at the boundary of the spacer in Fig. 4.13 represents the current density; (iii) A small ion vacuum area that may be caused by the accumulation of a large amount of charge on the boundary. Compared with the upper surface, it can be seen that the lower surface had a similar trend, but the change of the density was more gradual. The reason is that the structure of the lower surface was more complicated, the curvature radius changed more, and the current density was stronger as shown in the size of the arrow in Fig. 4.13.

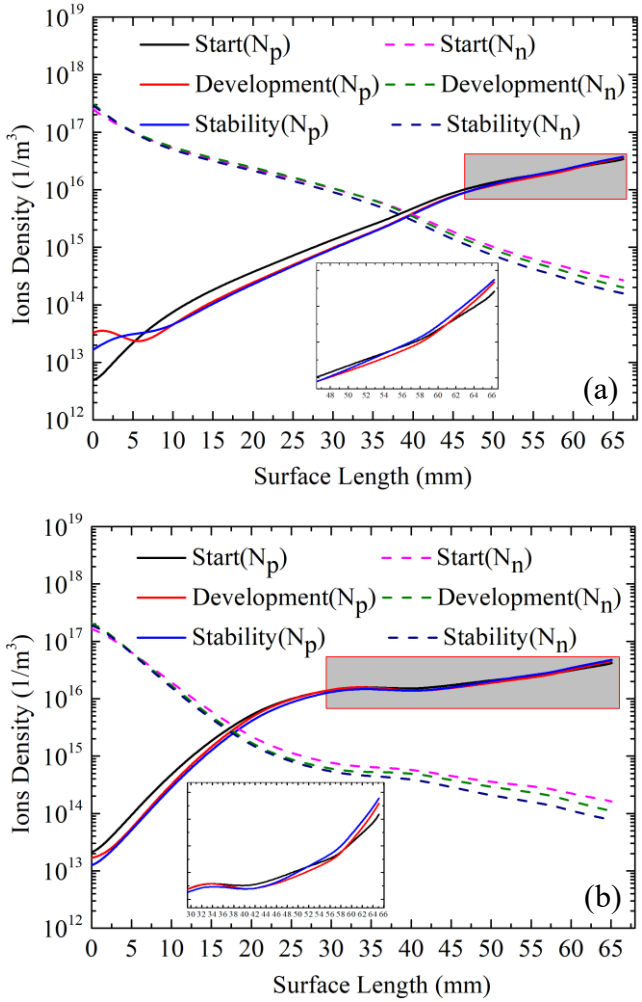

Fig. 4.12. Ion density under DC super imposed same polarity lightning impulse voltage (a) upper surface, (b) lower surface.

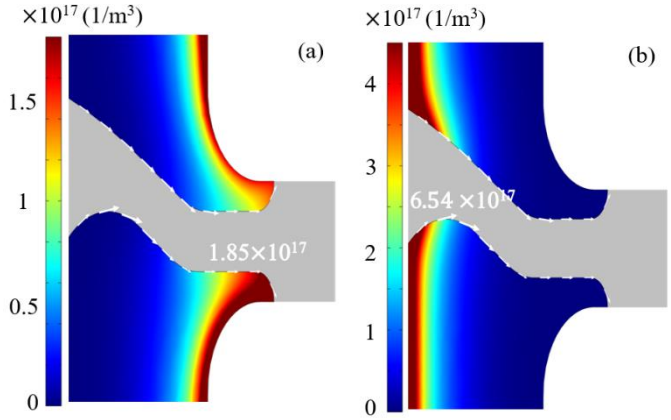

Fig. 4.13. Ion density distribution around the spacer under DC superimposed same polarity lightning impulse voltage (a) Np, (b) Nn.

The ion density under DC superimposed opposite polarity lightning impulse voltage on the surface of the spacer is shown in Fig. 4.14. Both the upper and lower surfaces of the spacer as well as the positive and negative ions showed a similar pattern to the condition that under DC superimposed same polarity lightning impulse voltage. The positive ion density gradually increased, and the negative ion density gradually decreased. The maximum ion density was 6.23×10^{16} 1/m^{3}and 9.08×10^{16} 1/m^3 for positive and negative ions respectively. Combined with the ion density distribution around the spacer as shown in Fig. 4.15, it can be found that the ion density was significantly reduced. Generally, when the ion density exceeds 10^{19} 1/m^3, breakdown is likely to happen [106]. So, in this study, the spacer did not reach the failure stage after superimposed lightning voltage.

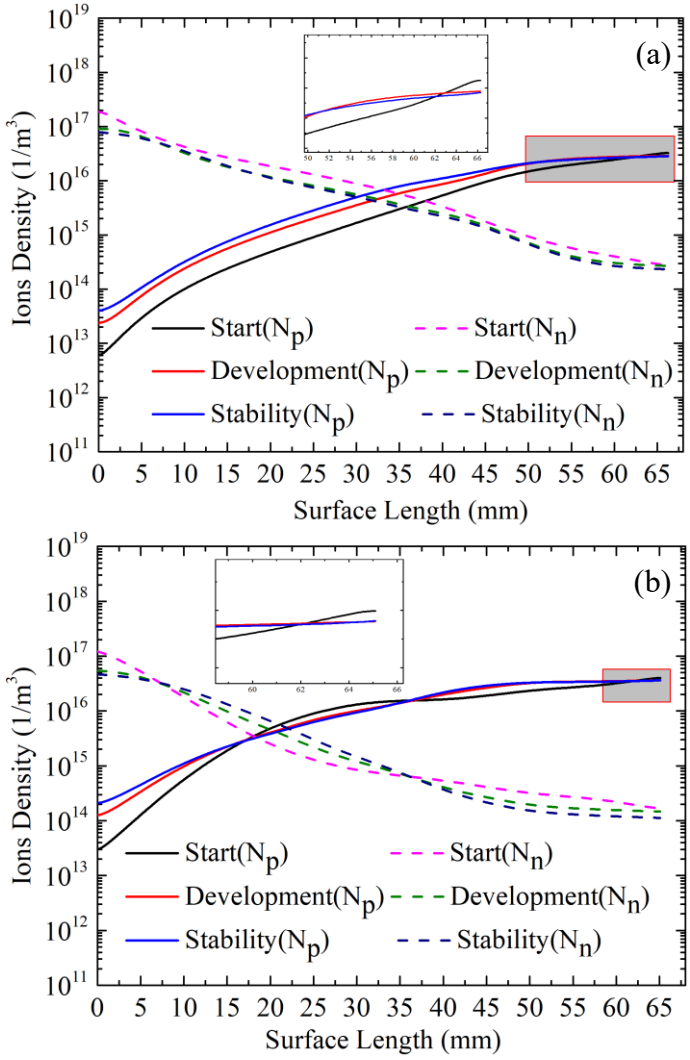

Fig. 4.14. Ion density under DC super imposed opposite polarity lightning impulse voltage (a) upper surface, (b) lower surface.

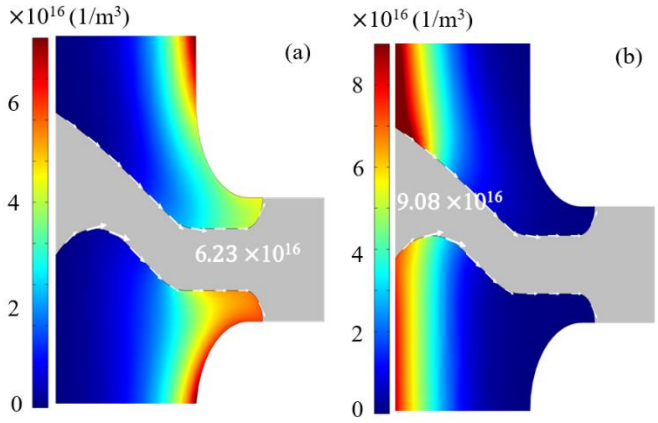

Fig. 4.15. Ion density distribution around the spacer under DC super imposed opposite polarity lightning impulse voltage (a) Np, (b) Nn.

Fig. 4.16 shows the ion density under lightning impulse voltage on the surface of the spacer. It can be seen that the change of positive and negative ions under lightning impulse voltage was very small and the ion density changed in the range of 10^{15}-10^{16} 1/m^3. At the beginning, the density of positive and negative ions remained almost the same. Then, the positive ions slowly increased and the negative ions started to decrease. The main reason is attributed to the density of positive and negative ions that was lowest under lightning impulse voltage conditions, which were 1.10×10^{16} 1/m^3 and 2.09×10^{16} 1/m^3 respectively. As shown in the ion density distribution around the spacer in Fig. 4.17, the ion number density at LI was low, the ion density did not change much and the charge accumulation effect was not obvious. It is worth noting that on the lower surface, at the beginning stage the lightning impulse, the amplitude was large and ion density fluctuation was small, while in the later stage with the decrease of the lightning impulse voltage, the density of positive and negative ions increased alternately due to the effect of charge accumulation and change of curvature, which corresponded to the alternating amplitude of positive and negative ions on the lower surface as shown in Fig. 4.17.

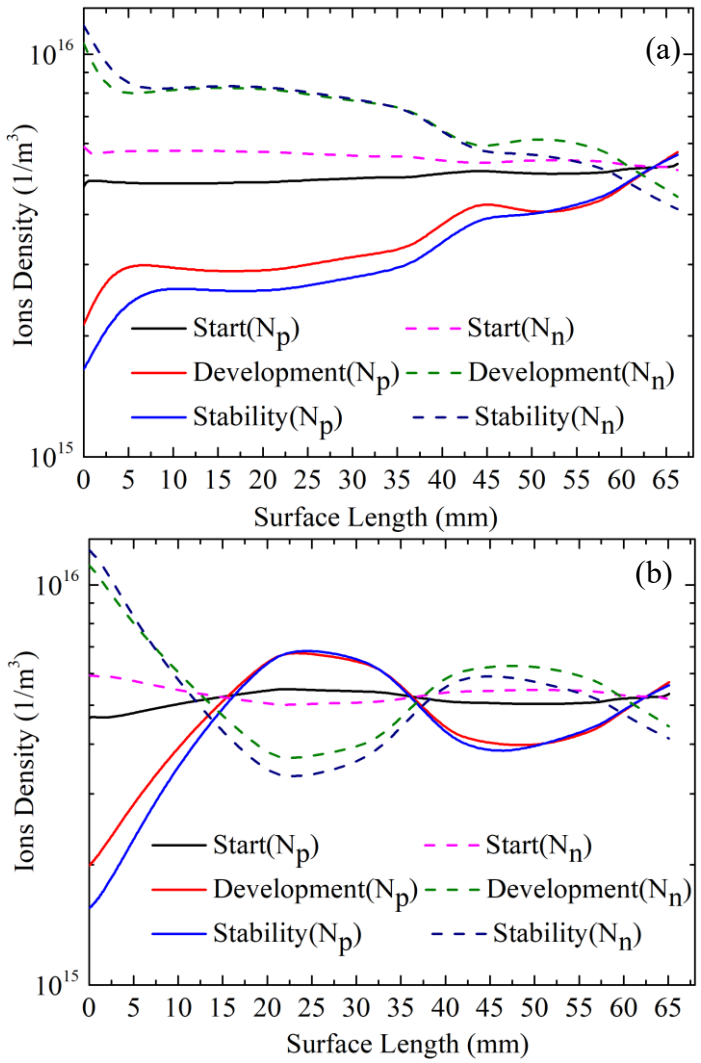

Fig. 4.16. Ion density under lightning impulse voltage (a) upper surface, (b) lower surface.

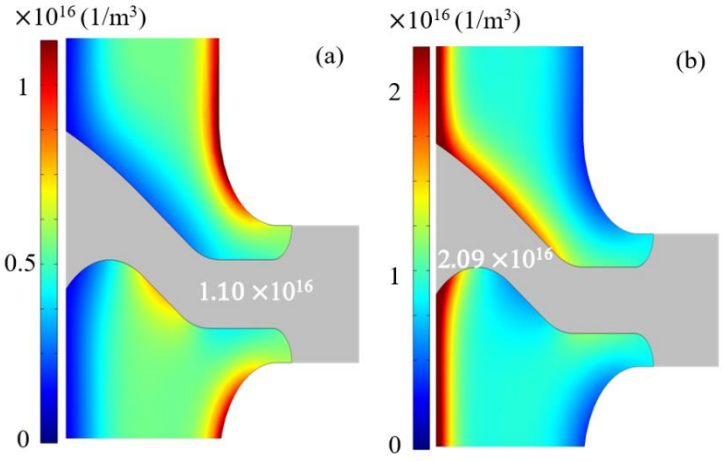

Fig. 4.17. Ion density distribution around the spacer under lightning impulse voltage (a) Np, (b) Nn.

4.4 Conclusion

Several researchers have conducted investigations concerning the electric field distribution under DC superimposed lightning impulse voltage as described in [105], while the simulation results lacked ion density distribution. In [107], researchers calculated the ion density distribution under DC applied voltage, and it lacked results of other working conditions. In this work, the electric field distribution and space charge distribution was simulated using a finite element model combining steady-state and transient solvers in a gas-insulated system under DC superimposed lightning impulse voltage, which revealed the ion transportation law under lightning excitation. The main outcomes of this chapter can be summarized as follows:

- Under lightning impulse voltage and DC superimposed lightning impulse voltage, the electric field intensity on the lower surface of the spacer was higher than that on the upper surface with the value around 2 kV/mm, and the electric field intensity tended to have smaller transition time from lightning to stability.
- Under lightning impulse voltage and DC superimposed lightning impulse voltage, the maximum electric field on the spacer surface showed a similar trend that increased first and then decreased. Among them, the tangential amplitude of electric field under DC superimposed same polarity lightning impulse voltage was the highest.
- The tangential electric field distribution on the surface of the spacer was affected by the radius of the curvature. The tangential electric field intensity fluctuated at 3 mm, 37 mm and 57 mm on the upper surface of the spacer, which was the combined effect of the electric field enhancement, the charge accumulation, and the attenuation of the lightning impulse voltage.
- With the three stages of lightning impulse voltage start, development, and stability, the electric field distribution on the surface of the spacer presented a decreasing trend, and the pulse function reached its peak at the start stage.

It is also speculated that, under the three working conditions, if there is no flashover on the surface of the spacer, the system will return to working state after the lightning impulse is superimposed on the DC voltage.

- The electric field distribution under DC superimposed positive polarity lightning impulse voltage was the highest, and the positive ions showed an increasing trend while the negative ions showed the opposite trend. The ions were driven by the electric force, positive ions Np, migrated to the enclosure and increased with the highest value of ion density 1.85×10^{17} $1/m^3$, while negative ions Nn accumulated on the conductor in the opposite direction, with the highest value of ion density 6.54×10^{17} $1/m^3$.
- When the ion concentration was not high, it was difficult to change linearly due to the temperature constraints and electric field distribution. When the positive and negative ions moved in opposite directions, they were attracted by the Coulomb force of the nearby moving ions, and part of them accumulated or deviated. The movement was in the direction of the current density.

Chapter 5 Design of Reduced Scale GIL and Associated Laboratory Equipment

5.1 Introduction

Up to recently, gas insulation systems are filled with SF_6 or its mixture as the insulation medium and use spacers to isolate gas compartments and mechanically support conductors. This research investigates the use of geometric and material properties optimization for spacer models to reduce electric field enhancement along the spacer surface. Moreover, it explores the feasibility of using C4-PFN and CF_3I gas mixtures as potential substitutes for SF_6 in DC gas insulation system applications.

In this research project, a reduced-scale coaxial GIL prototype was designed and fabricated to investigate the dielectric performance of the optimized shape with conventional material spacers and filled with C4-PFN and CF_3I gas mixtures. The PDIV experiment under DC voltage was used to check the partial discharge inception voltage of the C4-PFN/CO_2 and CF_3I/CO_2 gas mixtures, and when conducting the PDIV experiment, different electrode configurations were selected.

This chapter first describes the development of the reduced-scale GIL prototype and pressure vessel for gas research. Subsequently, the fabrication of the spacers is introduced, and then the test setup is reviewed in the context of this research.

5.2 Pressure Vessel

5.2.1 Reduced-scale GIL Prototype

The reduced-scale GIL prototype is made of stainless steel and does not react with alternative gases. The design and construction of the prototype is based on 1:4 scale of 420 kV AC GIL. The maximum design pressure is limited to 11 bar (abs.). Table. 5.1 and Fig. 5.1 show the dimensions of the prototype.

Table. 5.1. Demonstrator of the GIL prototype

Parameter	Demonstrator	Reduced Scale
R_e	270 mm	64.1mm
D_e	540mm	128.2mm
R_c	95.5mm	24.15mm
D_c	191mm	48.3mm
Gas gap	174.5mm	39.95mm

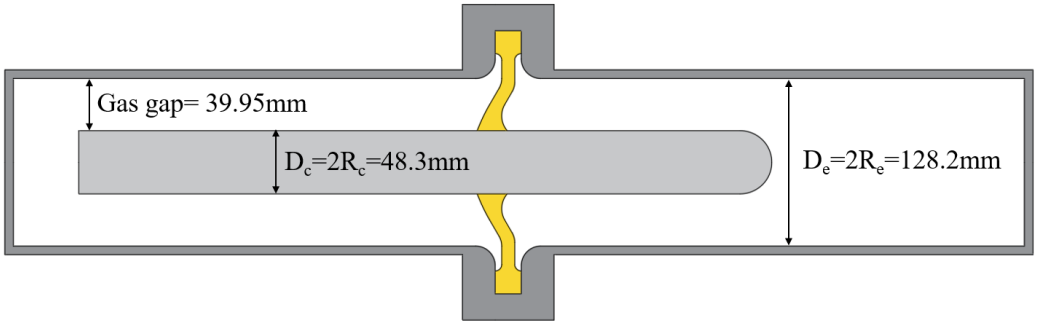

Fig. 5.1. Reduced-scale GIL prototype.

Fig. 5.2 shows the constructed reduced-scale GIL prototype. The prototype is divided into two sections with lengths 550mm and 950mm and has a radius of 64.1mm, giving the GIL vessel volumes of approximately 7L and 12L in each section. The wall thickness of the prototype enclosure is at least 10mm. The conductor inside the GIL prototype was connected to the high voltage power supply through a 400kV bushing. A side window was installed in order to observe the process when performing the tests. O-rings were used to prevent any leakage at each bolted joint. A spacer was installed between section 1 and section 2 for practical withstand tests.

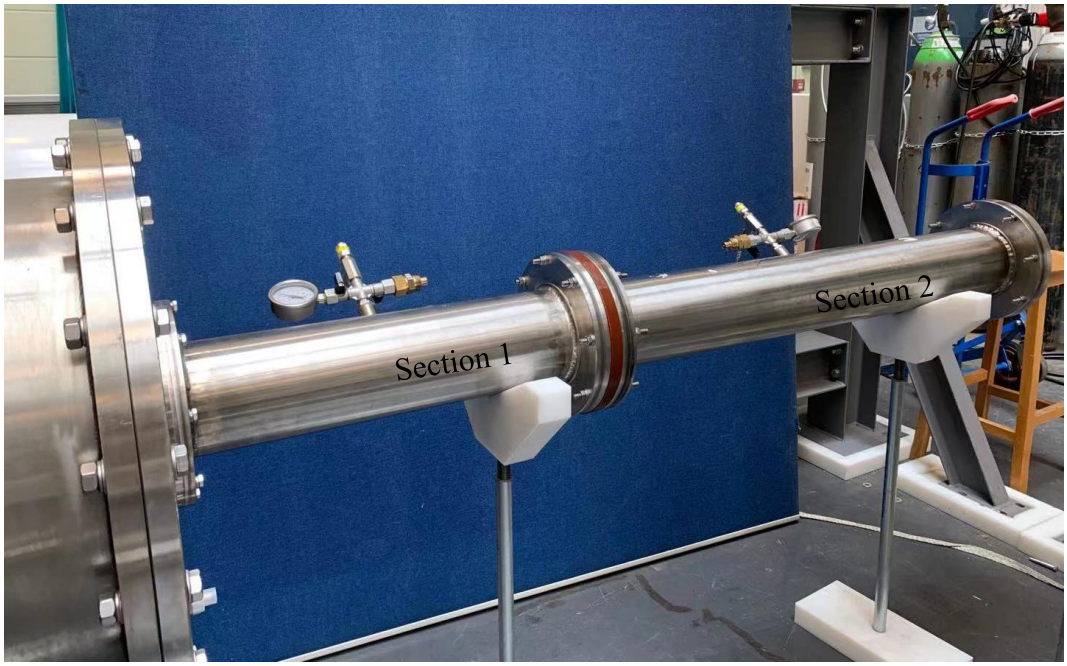

Fig. 5.2. Reduced-scale GIL prototype.

After fabrication, the external surfaces of the high voltage electrode tubes and internal surfaces of the enclosure sections were polished to obtain a surface roughness of 0.421µm to 0.967µm by the manufacture. The HV electrode tube is shown in Fig. 5.3. The pressure test for each section was carried out with water under 15 bar(abs.) for 1 hour. The vacuum and gas pressure tests with N_2 at 6 bar(abs.), 8 bar(abs.) and 10 bar(abs.). During this period, no signs of pressure drop were detected.

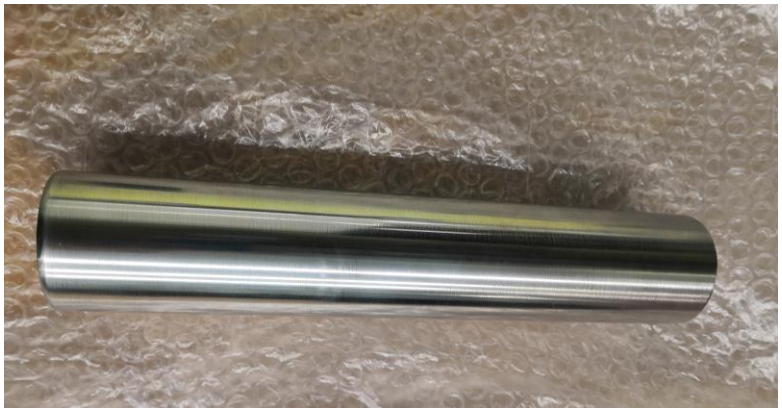

Fig. 5.3. Inner conductor (HV electrode tube) for GIL prototype.

Each section of the prototype was equipped with an analog pressure gauge to

provide the reading of the internal pressure of the vessel with the range from 1-15 bar(abs.), and the accuracy class of the pressure gauge is 1.0 as shown in Fig. 5.4.

Fig. 5.4. Analog pressure gauge from 1-15bar(abs.).

5.2.2 Pressure Vessel for PDIV Test

Fig. 5.5 shows the adopted vessel for PDIV test. Again, the vessel is made of stainless steel with a diameter of 200mm, a height of 380mm, and a thickness of 10mm minimum giving a volume of around 12L with a maximum operating pressure up to 12 bar(abs.). This pressure vessel was designed [108] to conduct dielectric tests for alternative gases using different electrode configurations and insulation gas media. The design pressure is 15 bar(abs.).

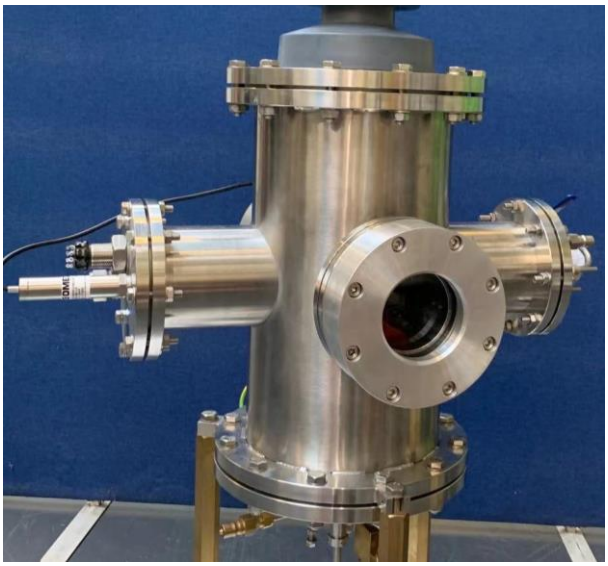

Fig. 5.5. Pressure vessel for PDIV test.

When performing the experiments, in order to measure the pressure inside the vessel, an OMEGA PXM409-010 BAUABH built-in pressure sensor was used to measure the pressure as shown in Fig. 5.6. The sensor has a standard type A plug USB connector for direct connection to a computer, and a USB output pressure transducer with up to 1000 readings per second. The measurement range is from 0 mbar to 20 bar (abs.).

Fig. 5.6. OMEGA built-in pressure sensor.

5.3 Spacers

The spacers used for verification tests were based on the geometrical optimization as described in Chapter 3 and were designed and fabricated at the university workshop as shown in Fig. 5.7 and Fig. 5.8.

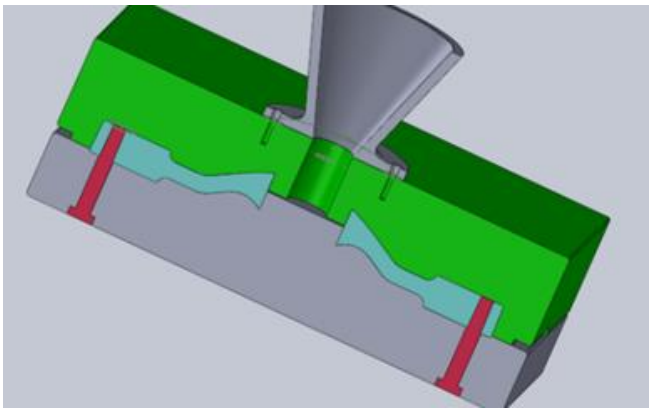

Fig. 5.7. Mold design of the optimized spacer.

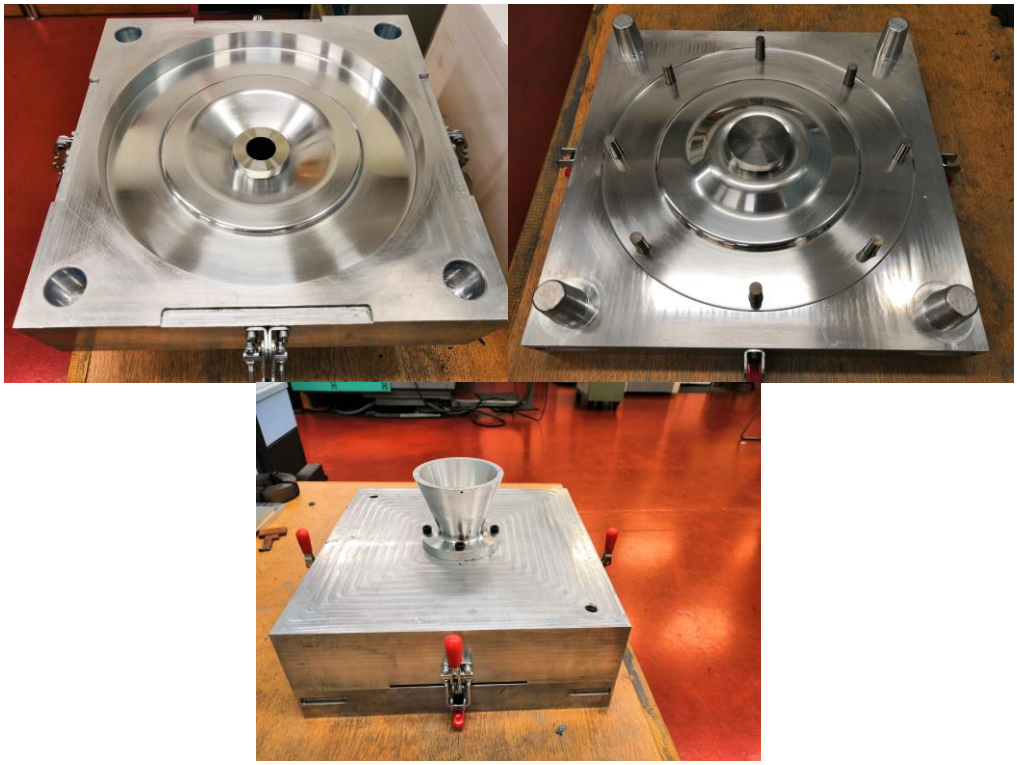

Fig. 5.8. Mold of the optimized spacer.

Spacer model fabrication was at MEKUFA UK which is a manufacturer of epoxy based MV components. Two epoxy formulations were used: (i) Silica-filled epoxy: Silica filler was provided by MEKUFA UK; and (ii) Alumina-filled epoxy: Alumina filler was provided by Huber Germany. The epoxy resin was sourced from Huntsman US. The composite materials were prepared at Synergy Devices Limited. The manufacturing process was vacuum casting, and, for each epoxy formulation, 4 spacer models were fabricated.

The general procedure to fabricate the spacer models is as follows: The melted epoxy resin is intensively mixed with the dried filler in a thin film degassing mixer under vacuum and then the hardener is added. The ready mixture is fed directly into the preheated spacer mold in the autoclave at 120–140 °C.

It should be noted that the fabrication of the DC spacers was not a trivial task and straightforward. Indeed, the first trials using silica-filled epoxy were not successful due to the leak of the melted filled epoxy from the mold during casting as illustrated in Fig.5.8(a) leading to imperfections at some locations of the spacers as shown in Fig.5.8(b) and resulting in a bad gas tightness at the flanges, as well as defects near

the central conductor that would lead to surface flashover during HV testing shown in Fig. 5.9.

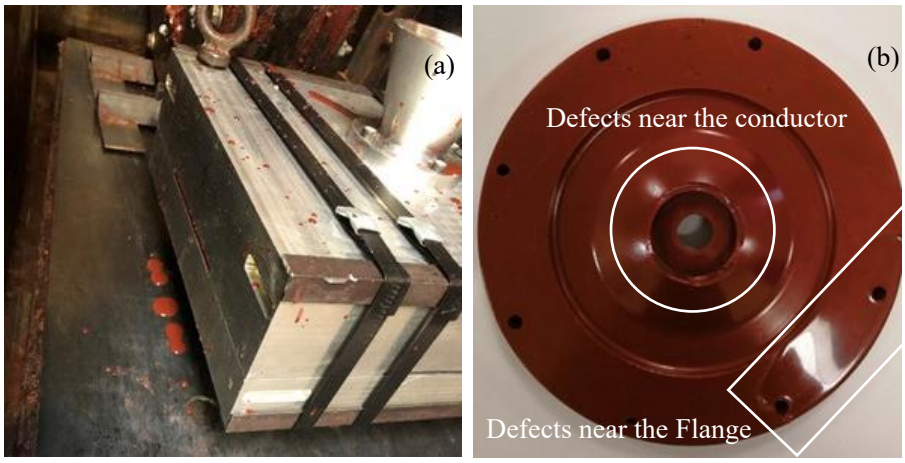

Fig. 5.9. Problems encountered during spacers' fabrication, (a) Leak of the melted filled epoxy from the mold; (b) presence of imperfections near the central conductor and at some locations near the flange.

After mold improvement, the desired DC spacers were finally obtained smooth and without any defects as shown in Fig. 5.10.

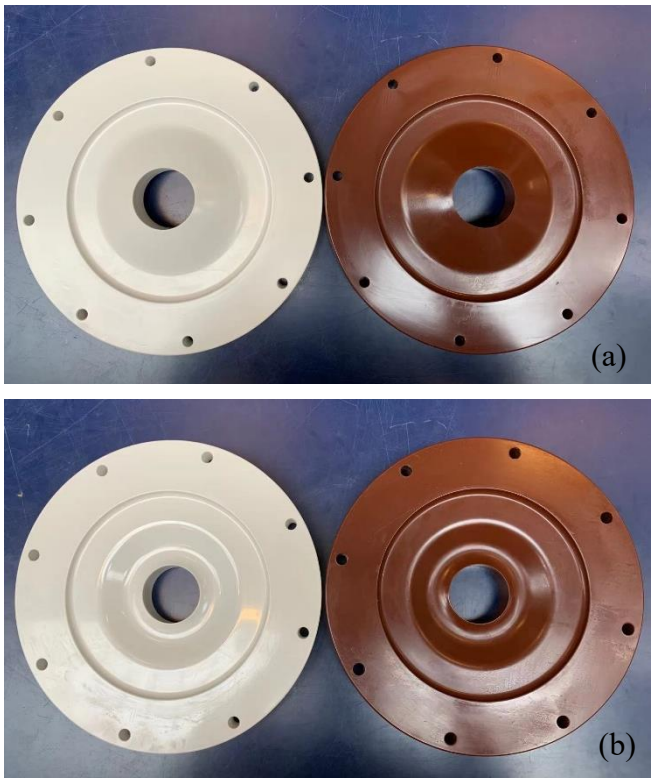

Fig. 5.10. Spacer models (a) convex (b) concave: Alumina filled epoxy (left) and Silica filled epoxy (right).

5.4 Electrodes

There were two sets of needle-plane electrode systems which were used for the PDIV tests with the tip diameter 20±0.5μm and 200±0.5μm respectively. The needle electrode is made of tungsten. The needle shaft diameter is 0.51mm, and the length is 32mm. The plane electrode is made of stainless-steel with the diameter of 150mm and the thickness of 15mm. The electrode configuration is shown in Fig. 5.11.

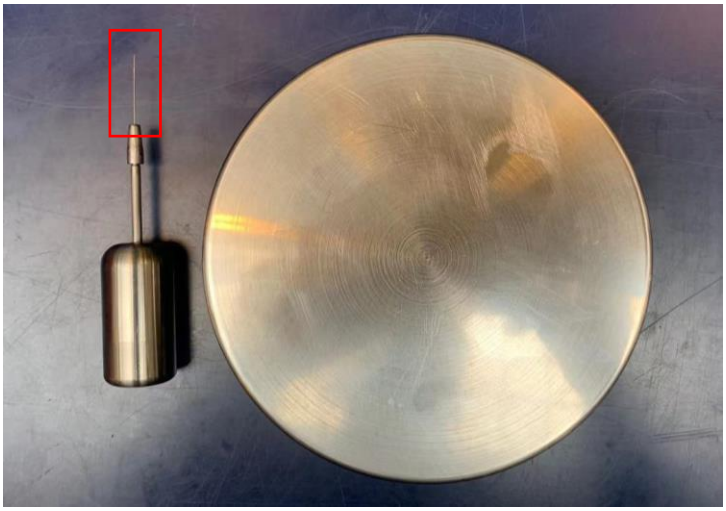

Fig. 5.11. Needle-plane electrodes setups

5.5 Generation and Measurement of Direct Voltage and Current

5.5.1 Generation of DC Voltage

In the laboratory experimental work, a Glassman WR Series DC power supply was used to generate DC voltage, perform spacer withstand tests and partial discharge experiments in different gas mixtures as shown in Fig. 5.12. If a load arcing problem develops, internal circuitry will detect the arcs and cut off the power supply, then automatically restart. The power supply can generate up to 125kV output voltage and the maximum output current is 20mA.

Fig. 5.12. Glassman DC power supply.

5.5.2 Measurement of DC Voltage

In this project, a Ross Engineering Corp. series 081014-4 DC voltage divider was used to measure the applied voltage with a divider ratio of 1:2000 and the bandwidth is up to 10M Hz as shown in Fig. 5.13.

Fig. 5.13. DC voltage divider.

5.5.3 Measurement of Current

A Stangenes Industries inc. 3-0.1 series current transformer (CT) was used to measure the leakage current when doing the withstand test. The output accuracy (±0.5%) was 0.1(Volt/Amp), the maximum measured current was 5000A, and the useful rise time is 20ns as shown in Fig. 5.14. Note that this CT will not measure

the direct current under steady state conditions but will only detect the discharge activity with high frequency variations.

Fig. 5.14. Stangenes Industries inc. 3-0.1 series CT.

5.5.4 Recording Instrument

When performing the spacer withstand test, a Teledyne LeCroy WaveJet Touch 354 oscilloscope was used. The oscilloscope can capture high-speed single pulses at a maximum sampling rate of 2 GS/s.

When carrying out the PDIV test, the signal was measured by the Pico Technology 5000 series Pico-scope. The Pico-scope can capture high-speed single pulses at a maximum sampling rate of 1 GS/s and 500MHz bandwidth. Equation (5.1) is frequently referred to as a rule of thumb and it is used to estimate the measuring capability of oscilloscopes with regards to the rise time of the obtained signals and can be found in manuals and user guides provided by the manufacturers of such equipment[109].

$$\tau_r = \frac{0.35}{f_{3dB}} \tag{5.1}$$

From the specific pulse with a PDIV event as described in Chapter 6, the very fast rise time is around 6 ns, indicating the bandwidth requirement of the pico-scope is around 58 MHz which proved the pico-scope has sufficient bandwidth range.

5.6 Gas Removal and Filling System

Since this study involves a gas mixture of C4-PFN or CF_3I, it is necessary to prevent the gas from being released into the atmosphere as much as possible during

each experiment. Besides, after each experiment, the gas mixture must be taken out and stored in a gas cylinder which can be seen in Fig.5.15. This will then be disposed of in an environmentally responsible manner.

5.6.1 Gas Storage Cylinders

Before conducting the experiments, new gas mixtures were made first. According to Dalton's law[110], the total pressure of the gas mixture equals the sum of the partial pressures as shown in Equation (5.2).

$$P_T = \sum_{i=1}^{n} P_i \tag{5.2}$$

In this case, the pressure of C4-PFN/CO_2 and CF_3I/CO_2 mixtures can be determined as:

$$P_{T1} = P_{\mathrm{C4-PFN}} + P_{\mathrm{CO2}} \tag{5.3}$$

$$P_{T2} = P_{\mathrm{CF3I}} + P_{\mathrm{CO2}} \tag{5.4}$$

As can be seen from Equation (5.3) and Equation (5.4), if a total pressure 1 bar (abs.) is filled into the vessel, the partial pressures of 4% C4-PFN/96%CO_2 and 30% CF_3I/70% CO_2 are 0.04 bar (abs.) for C4-PFN, 0.96 bar (abs.) for CO_2; and 0.3 bar (abs.) for CF_3I, 0.7 bar (abs.) for CO_2 respectively.

When creating the new gas mixture, the bottle was vacuumed to leave no impurity inside the bottle, and the lower proportion gas was filled first. In this case, the vessel was first filled with environmentally friendly alternative gases, and then the buffer gas was added up to the total pressure. After making the new gas mixture, the cylinder containing the new gas was stood for 5 days to fully mix the gases. When the experiment is over, the test gas mixture was pumped out of the vessel and went back to the storage cylinder.

In order to vacuum the pressure vessel and inject other atmospheric gases, a DILO B078R06 vacuum pump was used. The suction capacity of the vacuum pump is 10 m^3/h, and the achievable final pressure can be less than 1 mbar(abs.).

5.6.2 Gas Removal System for Alternative Gas Mixtures

The gas removal system for alternative gas mixtures adopted the degassing system produced by DILO. The device for C4-PFN was with model B095R12, and the device for CF_3I was a Mini Service Cart with model Z579R03. Both carts consisted of compressors, vacuum compressors, vacuum pumps, pre-filters and some other accessories and some other components.

When recovering the gas mixture, the gas passed through three main units before entering the gas cylinder, including a pre-filter unit, a vacuum compressor unit and a compressor unit.

In the pre-filter unit, the dry filter element absorbs moisture and decomposition products from the gas. The device consists of a tube filled with desiccant. There is also a particle filter, which can filter solid particles and solid decomposition products in the gas. This will ensure that the gas is purified and dried during the recovery process.

The vacuum compressor is dry-running, completely oil-free. With a delivery rate of 3.3 m^3/h for C4-PFN and 1.3 m^3/h for CF_3I, the device for C4-PFN can achieve a final vacuum of less than 5mbar(abs.) and the device for CF_3I can achieve a final vacuum of less than 10 mbar (abs.) respectively.

The compressor unit is also a dry-running type. The maximum suction overpressure is 10 bar (abs.), which is controlled by a pressure switch. The device provides a final pressure of up to 20 bar at a delivery speed of 1.9 m^3/h for C4-PFN, and 50 bar at a delivery speed of 1.0 m^3/h for CF_3I. The process diagram of making new 4% C4-PFN/96%CO_2 and 30% CF_3I/70% CO_2 gas mixtures is shown in Fig. 5.15. Before the gas injection, the pressure vessel volume is vacuumed down to less than 1 mbar using a vacuum pump. Once the required vacuum levels are reached, the vacuuming process continues for 30 additional minutes in order to minimize the presence of humidity residuals. C4-PFN or CF_3I will be injected first and then it will be balanced with CO_2. After that, the gas recovery system including the pre-filter unit and the compressor is connected to the vessel together with a gas cylinder where the new gas mixtures are stored to recycle the gas mixtures. The condition of

the gas mixture is labelled for the storage cylinder.

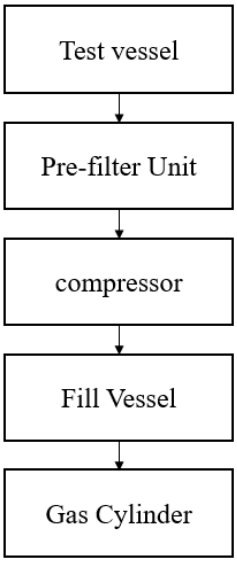

Fig. 5.15. Process diagram of making new 4% C4-PFN/96%CO_2 and 30% CF_3I/70% CO_2 gas mixtures.

5.7 Fittings and Assemblies

5.7.1 Pressure Gauges

Besides the analog pressure gauge on the pressure vessel, in order to obtain more accurate readings, Truck DPI 705IS and DPI 705E electronic pressure gauges were used to measure the pressure in the vessel with the gas mixtures of C4-PFN/CO_2 and CF_3I/CO_2 respectively. The measuring range of the two pressure gauges is 0 - 20 bar (abs.). Each gas mixture has a dedicated pressure gauge to avoid mixing C4-PFN and CF_3I.

5.7.2 Regulators and Heater

In order to fill the pressure vessel, a pressure regulator was required. It was installed at the outlet of the gas cylinder or high-pressure pipeline. The regulator was used to reduce the gas pressure in the cylinder to a lower pressure which was set by the user.

When CO_2 passed from the gas cylinder through the outlet valve, the gas pressure decreases and absorbs heat. During this process, the temperature of CO_2 would drop, which might cause the moisture in the CO_2 to freeze the regulator, and the flow of gas would be restricted, which might block the system. Therefore, a CO_2 heater was needed to eliminate this effect. The heater heats the CO_2 gas to approximately 79 ºC, and it was connected between the output end of the gas cylinder and the input end of the CO_2 pressure regulator. Fig. 5.15 shows the procedure of making new gas mixtures.

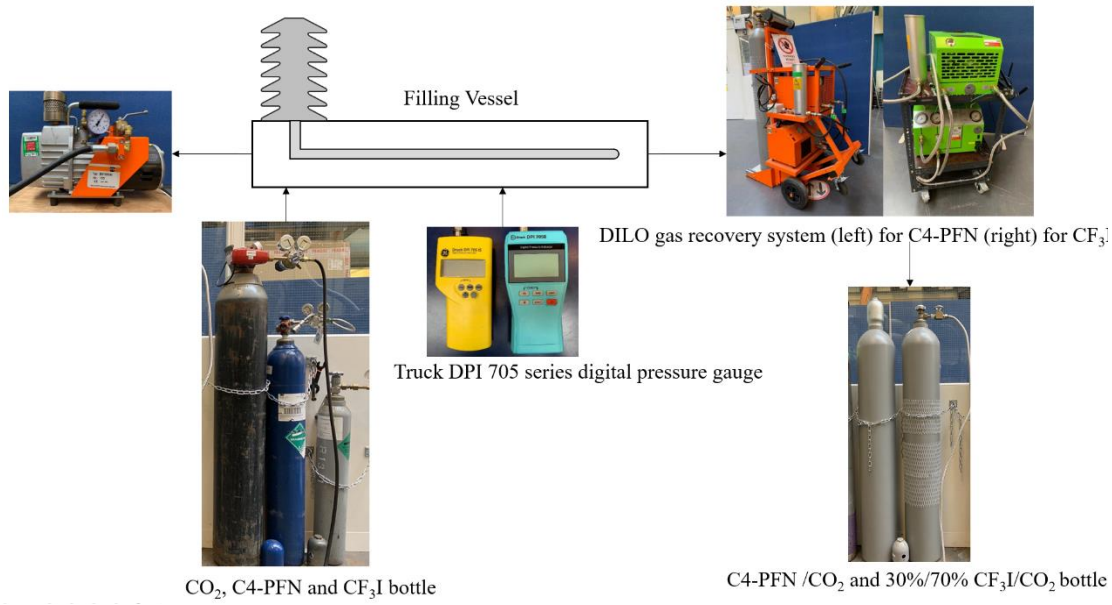

Fig. 5.16. Procedure of making new gas mixtures.

5.8 Protection System

During the withstand experiment, the likely large magnitude current generated by the flashover on the spacer surface or breakdown in the gas might damage the DC power supply. A circuit breaker was designed to prevent this, and the circuit is shown in Fig. 5.17. The circuit will keep open before pushing the button “Push to Enable”. When the large current is generated, an external trigger signal will be sent out from the oscilloscope. After receiving this signal, a signal will be sent out from the wave generator to disable the circuit.

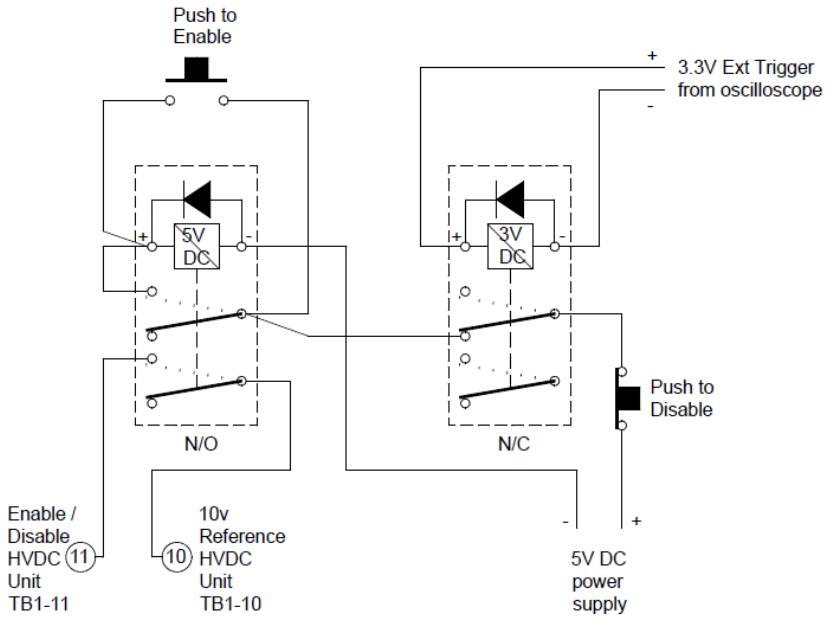

Fig. 5.17. Circuit of the circuit breaker.

The external trigger from the back panel of the Teledyne Lecroy WaveJet Touch oscilloscope was connected to the RIGOL DG4062 series wave generator as shown in Fig. 5.18, and then to the circuit breaker, because the pulse of the external trigger from the oscilloscope could not activate the circuit breaker.

Fig. 5.18. RIGOL DG4062 series wave generator.

The wave generator was set such that, when receiving the trigger from the external trigger from the oscilloscope, the wave generator would send out a pulse voltage with the waveform width of 5 seconds, rising time of 10μs, and the amplitude of 8V to activate the circuit breaker. After receiving the trigger, the circuit

breaker would automatically disable the high voltage to protect the DC power supply and other equipment. Fig. 5.19 shows the figure of the connection between the circuit breaker, oscilloscope, and the wave generator.

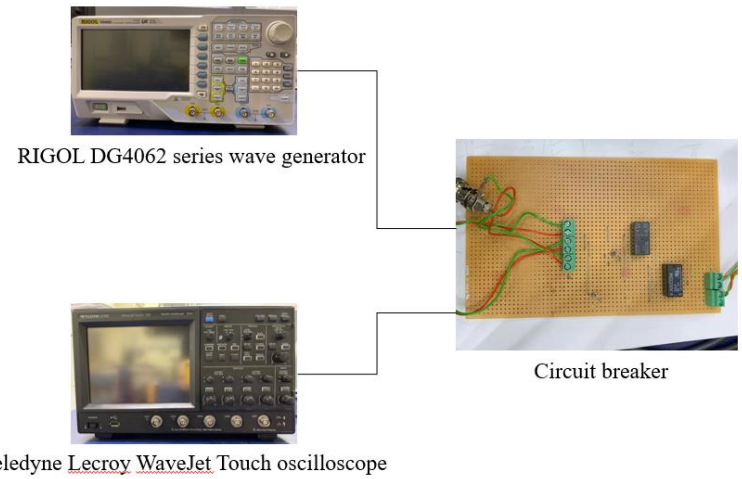

Fig. 5.19. Connection between the circuit breaker, oscilloscope, and the wave generator.

5.9 Conclusion

This chapter described the functions of the experimental setups for the research, including: (i) two pressure vessels used as test chambers; (ii) the fabrication of the conventional material spacers; (iii) the needle-plane electrodes for PDIV tests; (iv) generation of DC voltage; (v) the measurement of DC voltage and current which includes a DC divider, a current transformer, a digital storage oscilloscope, and a Pico scope; (vi) a gas recovery system which includes DILO units and storage cylinders; and (vii) a protection system was designed to prevent unexpected flashover on the surface of insulator or breakdown in the gas.

The reduced-scale GIL prototype for withstand test was built which could carry out tests of up to 11 bars (abs.) in pressure using shape modified and conventional material spacers. A test rig for PDIV under DC voltage was built since it is important to investigate the partial discharge characteristics in different gas mixtures, pressures, electrode configurations and gap distances.

Chapter 6 Laboratory Experiments on SF_6 Free Gas Mixtures

6.1 Introduction

Due to the rapid development of DC power transmission technology, HVDC gas insulated transmission lines (GIL) and gas insulated switchgear (GIS) are considered as potential alternative systems for future long-distance DC transmission. Therefore, extensive research and development are currently ongoing worldwide. Spacers for the HVDC GIS/GIL play an important role in mechanically supporting conductors and separating compartments. At the same time, their insulation performance affects the safety of system operation. Design rules and knowledge specific to AC spacers do not apply to those of DC spacers. SF_6 has been widely used as a reliable insulating gas thanks to its excellent dielectric properties. However, due to its high global warming potential, other environmentally friendly alternative gas mixtures to replace the usage of SF_6 have been found such as C4-Perfluoronitril (C4-PFN) and Trifluoroiodomethane (CF_3I) based gas mixtures., an optimized shape of a spacer model based on finite element electric field calculations were studied. A deep understanding of the behaviour of the HVDC gas insulated systems using alternative insulating gases is necessary to operate safely and economically. This chapter first presents the withstand tests using the shape optimized spacers which considered the shape influence on the surface electric field intensity of the spacer under HVDC applied voltage as determined in Chapter 3 with SF_6-free surrounding gas mixtures C4-PFN/CO_2 and CF_3I/CO_2. Then, the partial discharge inception voltage (PDIV) using C4-PFN/CO_2 and CF_3I/CO_2 gas mixtures are tested at different pressures ranging from 1 bar to 5 bar under both positive and negative DC voltage with electrode arrangement of different shapes and different gap distances.

6.2 Withstand Performance of Scaled GIL and New Spacer Design under Direct Voltage

Whilst high voltage gas-insulated switchgear (GIS) and gas-insulated transmission lines (GIL) are well-proven technologies for high-voltage alternating current (HVAC) electricity transmission applications under at least 800 kV AC [111]-[113],

their operation under high voltage direct current (HVDC) is extremely challenging. Therefore, they are currently under development worldwide for the ±550 kV DC rated voltage (maximum continuous operating voltage) and ultra-high voltage (UHV) of ±800 kV DC. The need for next generation UHVDC power transmission over long distances is expected to grow substantially in the coming years.

Among the critical challenges for this development, there is the problem of the epoxy cast resin insulators that are used to separate gas compartments of the GIL/GIS also so-called spacers and to provide mechanical support for high-voltage conductors. Indeed, under steady state DC operating voltage, the electric field distribution along the spacers' surface is controlled by the electric conductivity, σ, of the epoxy spacers and the surrounding gas through the formula $\mathrm{div}(\sigma E) = 0$, where σ depends on the electric field (E) and strongly on the temperature. So, when the GIL/GIS is under full load operation, a temperature gradient forms from the energized HV conductor to the grounded enclosure due to the DC current flow and, as a result of this, the electric field strength near the conductor reduces while, at the same time, it increases near the enclosure where the conductivity is lower.

Furthermore, in addition to the effect of the electric conductivity, the shape of the spacer and its contacts with the HV conductor/grounded enclosure-epoxy spacer-the gas called triple junction, also modify the electric field distribution. The electric field is intensified near the triple junction areas formed by the triple contact. Therefore, in order to keep the electric field strength within the permissible level, it is necessary to design the shape of the spacer properly.

Concerning research studies using HVDC spacer models having smaller dimensions (downsized spacers), some electric field distribution calculations based on the spacer shape optimization have been conducted[2],[62],[97], but without experimental verification. Few experimental investigations have been carried out on the novel spacer shape presented in the works [17],[114]-[115]. Hence, there is still much to be well understood and solved about spacers for HVDC and UHVDC GIL/GIS applications.

In this section, the withstand tests were carried out to verify the performance of the optimized spacer model made of standard alumina and silica filled epoxy

materials. A reduced scale gas insulated system to mimic the full size one was designed and constructed. The mold of the spacer was also designed and fabricated. Furthermore, three SF_6 free alternative gases were utilized in this investigation which are:

- 4% C4-perfluoronitrile (C4-PFN, 3M^{TM} Novec^{TM} 4710) mixed with 96% CO_2;
- 30% trifluoroiodomethane (CF_3I) mixed with 70% CO_2;
- Dry air.

This means that the compatibility of these gases with the DC spacers were also taken into account and checked.

6.2.1 Experimental Setup

Fig. 6.1 shows the schematic arrangement for the experimental investigation. It is composed of:

- A reduced-scale GIL prototype;

- A Glassman ± DC generator (Max. ±125 kV) to apply high voltage;

- A voltage divider with the ratio of 2000:1 to reduce the generated voltage to a safe and measurable level;

- A Stangenes Industries inc. 3-0.1 series current transformer (CT) connected to the GIL prototype to help identify whether a flashover occurred on the surface of the spacer or a breakdown across the gas gap of the prototype.

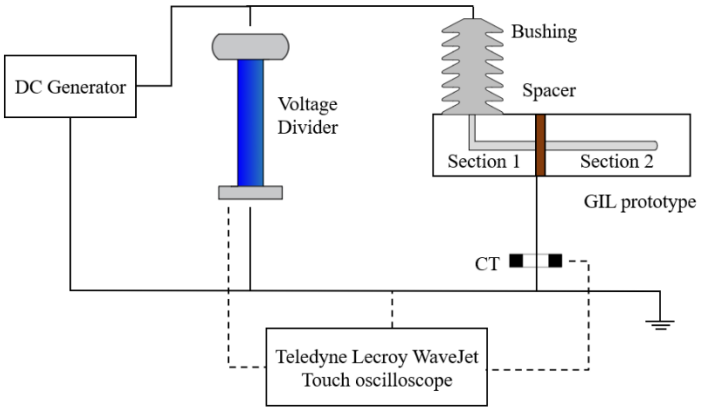

Fig. 6.1. Schematic arrangement of the HVDC test setup and the reduced scale GIL prototype.

6.2.1.1 GIL Prototype

The prototype is made of stainless steel and is composed of three compartments. A central conductor tube is supported by two spacers. Each compartment contains an opening for gas inlet and pressure gauge. The central conductor tube of the GIL prototype is connected to the high voltage (HV) supply through a bushing, and all the compartments are connected to the ground.

It should be noted that the design principle of this prototype is based on a commercial conventional full-size high voltage alternating current (HVAC) 420 kV gas-insulated system reduced to a ¼ scale. Namely, the dimensions of the full-size gas-insulated system relative to the outer diameter (D_C) of the central conductor and the inner diameter (D_E) of the enclosure are downsized by a factor of ¼ (0.25). Thus, the diameter of the inner conductor (D_C) and enclosure (D_E) of the reduced scale prototype are 48.3 mm and 128.2 mm, respectively, and the gas gap is 39.95 mm as shown in Fig.6.2. The ¼-size gas-insulated system has been chosen to reproduce the design of the commercial full-size HVAC 420 kV GIL/GIS in such a way to obtain approximately the same applied electric fields at the central HV conductor (E_C) and at the grounded enclosure (E_E).

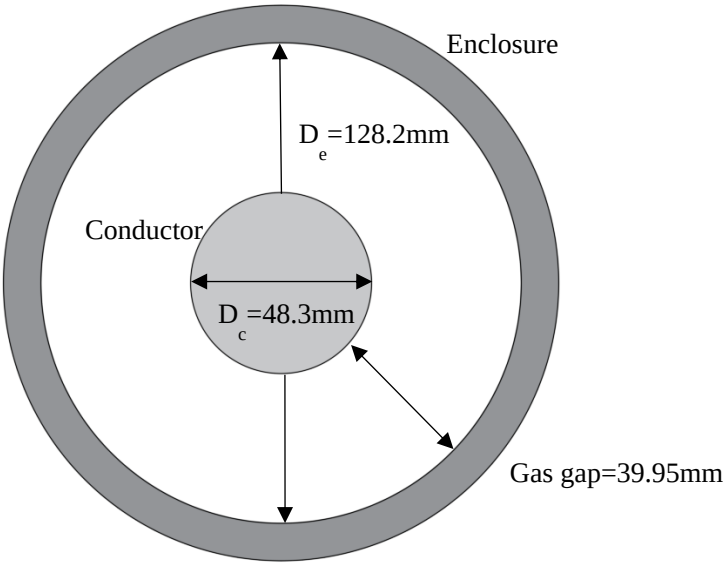

Fig. 6.2. Cross sections of reduced-scale GIL prototype.

Assuming that the 420 kV-AC design can also be used for the rated voltage 550 kV-DC, the resulting electric fields E_C and E_E are, respectively:

$$E_C = \frac{V}{\frac{1}{2}D_C \cdot \ln\frac{D_E}{D_C}} = \frac{550}{\frac{1}{2}191 \cdot \ln\frac{540}{191}} \approx 5.6\ \mathrm{kV/mm}, \quad (5.1)$$

$$E_E = \frac{V}{\frac{1}{2}D_E \cdot \ln\frac{D_E}{D_C}} = \frac{550}{\frac{1}{2}540 \cdot \ln\frac{540}{191}} \approx 2.0\ \mathrm{kV/mm}, \quad (5.2)$$

where V is the applied voltage on the inner conductor

Therefore, the corresponding direct voltage that was used in the simulations for the reduced scale model is 131.3 kV DC.

The mold of the optimized DC spacer was designed and fabricated at Cardiff University as detailed in Chapter 5. The spacers are made of conventional filled epoxy matrix with alumina (Al_2O_3), as mentioned above, and also with silica (SiO_2) The material formulations and the fabricated spacer models were agreed on and made in collaboration with MEKUFA UK, manufacturer of epoxy resin medium voltage components.

6.2.2 Experimental Procedure

Since SF_6 is a highly potent greenhouse gas [3], it is not allowed to use it in the

laboratory due to the restrictive regulations that require obtaining a license for using the gas, handling and recovery equipment, controlling leakage as well safe disposal of the used gas. Instead, these environmentally friendly surrounding gases were used for the experiments: dry air, 4% C4-PFN/96% CO_2, and 30% CF_3I/70% CO_2 whose electric breakdown strength (dielectric strength) with reference to that of SF_6 at the same pressure is given in Table 6.1[27][116]-[117]. It is worth noting that the measured breakdown voltage for air was under AC applied voltage with gas pressure 1-5 bar (abs.), for C4-PFN/CO_2 gas mixture was under DC applied voltage with gas pressure 1 bar (abs.), and for CF_3I /CO_2 gas mixture was under standard lightning impulse voltage with gas pressure 1 bar (abs.).

Table 6.1 Dielectric strength of alternative gas mixtures compared with SF_6[27][116]-[117].

Gas Mixture	**Dielectric Strength with Reference to SF_6**
Air	0.3–0.4
4% C4-PFN/96% CO_2	0.83
30% CF_3I/70% CO_2	0.75–0.8

To obtain the same dielectric strength performance as that of SF_6, higher pressures should be applied. Thus, based on Table 6.1 and that the pressure in a 500 kV GIL filled with pure SF_6, is 4.73 bar (abs.)[118], the pressures in the vessel when conducting the experiments were, respectively, 4.73/0.83 = 5.7 bar (abs.) for 4% C4-PFN/96% CO_2, 4.73/0.78 = 6 bar (abs.) for 30% CF_3I/70% CO_2 and at the maximum allowed operating pressure of 10 bar (abs.) for dry air.

Since the experiments were carried out in a high-pressure environment for a long time, in order to ensure the safety, reliability and tightness of the system, pressure tests were first performed before conducting the verification tests to ensure that there was no leakage in the system.

The DC voltage was applied up to 123 kV with both positive and negative polarities raised with a rate of 1 kV/s. It should be noted that since the voltage limit of the used DC generator is ±125 kV, one could cover ±119 kV that is equivalent to the nominal voltage ±500 kV DC of the full-size GIL.

A 6-hour test duration was considered for each applied voltage to verify the

dielectric performance of the spacers and gases. Each test was repeated once, and, if there was a flashover on the surface of the spacer, the test would be repeated with a new spacer.

The reduced-scale GIL prototype and spacers were first cleaned with alcohol before the tests. The spacers were dried for 24 hours in an oven to remove any moisture and then were installed in the prototype. Before conducting the experiments, the prototype was vacuumed for another 10 min after reaching the vacuum level to maintain low humidity levels inside, and then the test vessel was filled with experimental gas mixtures. All laboratory experiments were carried out in the ambient temperature range of 17–21 °C.

The verification tests were first run without the spacers and then with the presence of the spacers.

6.2.3 Verification Tests without the Spacers

Table 6.2 summarizes the DC test results. If there was no breakdown in the gas mixtures, the results are marked as passed. As can be seen in Table 6.2, all three insulating gases showed, as expected, good insulation performance up to ±123 kV DC since the maximum electric field at the central electrode of 5.2 kV/mm is much lower than the dielectric strength of the gases. Indeed, the electric breakdown field under DC voltage application of 4% C4-PFN/96% CO_2 at 5.7 bar (abs.) is around 24 kV/mm[78] and that of 30% CF_3I/70% CO_2 is around 9 kV/mm at 1 bar (abs.) [27].

Table 6.2. Test results without the spacer. Note that ±119 kV is equivalent to ±500 kV and ±123 kV is the maximum applicable voltage using the DC generator (Max. ±125 kV).

Applied voltage	Dry air 10 bar(abs.)	4% C4-PFN/96% CO_2 5.7 bar(abs.)	30% CF_3I/70% CO_2 6 bar(abs.)
+119kV	Passed	Passed	Passed
+123kV	Passed	Passed	Passed
-119kV	Passed	Passed	Passed
-123kV	Passed	Passed	Passed

6.2.4 Verification Tests with the Spacers

The verification tests with the integrated spacers in the GIL prototype were then performed. The results are shown in Tables 6.3 and 6.4. If there is no flashover on the surface of the spacer, the results are marked as passed. As can be seen, all the tests up to ±123 kV-DC using both silica and alumina filled epoxy-based spacers with surrounding dry air, 4% C4-PFN/96% CO_2 and 30% CF_3I/70% CO_2 were satisfactorily passed. The spacers did not exhibit any surface flashover which means that the shape-optimized cone-type spacer with the use of AC conventional silica and alumina filled epoxy materials seem to be adequate for use at constant ambient temperature.

Table 6.3. Tests' results using silica filled epoxy.

Applied voltage	Dry air 10 bar(abs.)	4% C4-PFN/96% CO_2 5.7 bar(abs.)	30% CF_3I/70% CO_2 6 bar(abs.)
+90 kV	Passed	Passed	Passed
+100 kV	Passed	Passed	Passed
+110 kV	Passed	Passed	Passed
+119 kV	Passed	Passed	Passed
+123 kV	Passed	Passed	Passed
-90 kV	Passed	Passed	Passed
-100 kV	Passed	Passed	Passed
-110 kV	Passed	Passed	Passed
-119 kV	Passed	Passed	Passed
-123 kV	Passed	Passed	Passed

Table 6.4. Tests' results using alumina filled epoxy.

Applied voltage	Dry air 10 bar(abs.)	4% C4-PFN/96% CO_2 5.7 bar(abs.)	30% CF_3I/70% CO_2 6 bar(abs.)
+90 kV	Passed	Passed	Passed
+100 kV	Passed	Passed	Passed
+110 kV	Passed	Passed	Passed
+119 kV	Passed	Passed	Passed
+123 kV	Passed	Passed	Passed
-90 kV	Passed	Passed	Passed
-100 kV	Passed	Passed	Passed
-110 kV	Passed	Passed	Passed
-119 kV	Passed	Passed	Passed
-123 kV	Passed	Passed	Passed

As mentioned before, only few experimental investigations [17],[114]-[115] were found in the literature on novel geometry of downsized HVDC spacers. Direct result comparison with them could not be made because the developed DC spacer's profile and its epoxy material composition are different. Nevertheless, some common findings are reported. In the series studies [17],[114]-[115], the developed model spacer has a bowl shape. According to the electric field simulations along the spacer surface under DC high voltage application, its magnitude is lower than that of the regular HVAC model spacer.

The bowl-shaped spacer made of silicon carbide (SiC)-doped epoxy exhibits better performance than without doping. To experimentally verify the design, the bowl-shaped model spacers were tested in a 220 kV GIS unit filled with SF_6 at ambient temperature (20–26 °C) [17],[114]-[115]. It was found that, under DC voltage application, the surface flashover voltage is the highest for the bowl-shaped model spacer with SiC doped epoxy.

Furthermore, the obtained results are in accordance with those on full-scale HV GIL/GIS spacers, where it was found that new profiles should be used for DC application [24].

6.3 Partial Discharge Characteristics of C4-PFN/CO_2 and CF_3I/CO_2 Gas Mixtures under DC Voltage

Due to the rapid development of DC power transmission technology, HVDC GIL and GIS are considered as potential alternative systems for future long-distance DC transmission. Therefore, extensive research and development activities are currently ongoing worldwide. SF_6 has been widely used as a reliable insulating gas thanks to its excellent dielectric properties. However, due to its high global warming potential, other environmentally friendly alternative gas mixtures to replace the usage of SF_6 have been tested. These include C4-PFN and CF_3I based gas mixtures. A deep understanding of the behavior of the HVDC gas insulated system using these alternative insulating gases is necessary to operate safely and economically. This means that partial discharge diagnosis under HVDC voltage application is very important.

At present, the research on the substitution of SF_6 mainly focuses on the dielectric strength of different substitute gases [119]-[128], and there are few studies on the partial discharge (PD) behaviour of these gases [78], [129]. Detection of PD allows rapid intervention to limit the subsequent development of the discharge and avoid situations that may cause major interruptions. Therefore, the detection, measurement and analysis of PD are of great significance to the monitoring and diagnosis of high-voltage devices.

So far, the understanding of the PD process in DC applications is still poor. In addition, the mechanism and characteristics of PD in alternating current (AC) applications present different modes, which cannot be directly applied to direct current. Some research works[130]-[132] are related to the behavior of PD under DC voltage, but the majority are carried out for standard gas such as nitrogen (N_2), air or SF_6. There are few studies on the PD behavior of SF_6 replacement gases. Given increasing legislation for limiting the usage of SF_6, understanding the use of environmentally friendly alternatives for partial discharge diagnosis under DC voltage is an area of strategic importance.

In this section, the partial discharge inception voltage was investigated using 4%

C4-PFN / 96% CO_2 and 30% CF_3I / 70% CO_2 gas mixture under DC applied voltages with positive and negative polarities at different pressures from 1 to 5 bar (abs.) with different electrode shapes and different gap distances. The investigation results of this section contribute a reference for the future application of SF_6 free alternatives in HVDC GIS/GIL applications.

6.3.1 Experimental Setup

Fig. 6.3 shows the main parts of the experimental configuration used in this chapter. For DC voltage application, a Glassman 125kV/20mA DC voltage generator was used, and the voltage was applied through a control unit to ensure personal safety. A voltage divider with the ratio of 2000:1 was used to reduce the generated voltage to a safe and measurable level. The test vessel is a polished stainless-steel pressure vessel with a diameter of 200mm and a height of 380mm giving the volume around 12L with the maximum operating pressure up to 12 bar(abs.).

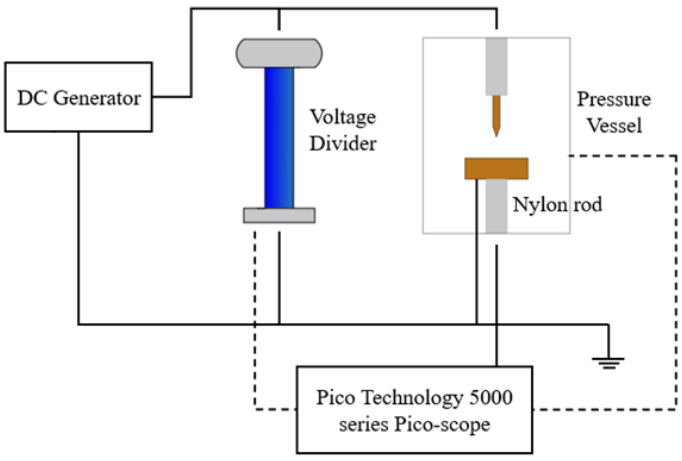

Fig. 6.3. Experimental setup for DC application (The test vessel showed in Fig.5.4).

A shunt resistor was used for direct measurement of the partial discharge current. Considering that the test configuration was installed in a grounded metal pressure vessel, an SMA connector was installed at the bottom of the plane electrode to make the measured partial discharge signal reach the sensing device with minimal

distortion and attenuation. A 50Ω RG-405 coaxial cable connected the plane electrode to the feedthrough pre-installed on the vessel, and then the signal was measured by the Pico Technology 5000 series Pico-scope, 200M Hz, 500MS/s, 8 bits.

Two sets of needle-plane electrode structures were used with the tip diameter 20±0.5μm and 200±0.5μm respectively. The needle electrode is made of tungsten. The needle shaft diameter is 0.51mm, and its length is 32mm. The needle electrode was connected to a stainless-steel needle holder. The plane electrode is made of stainless-steel with the diameter of 150mm and a thickness of 15mm. The plane electrode was electrically separated from the rest of the installation system by a nylon threaded rod.

6.3.2 Experimental Method

All the experiments described in this section were carried out in the laboratory temperature range of 19-22°C. The experimental vessel was cleaned with alcohol before the experiment and vacuumed for 10 minutes after reaching the vacuum level to maintain low humidity levels inside the test vessel. The experimental pressure ranged from 1 to 5 bar(abs.), and the distance between the electrodes varied from 10 to 30mm, and CO_2 was used for control experiments.

During the test, the trigger of the Pico-scope was set just above the noise, and the applied voltage was increased at a rate of 200V/s from zero until the detection of partial discharges. Five partial discharge tests were carried out for each gas medium combination. Between two consecutive voltage applications, a time interval of 5 minutes was maintained.

6.3.3 Experimental Results

6.3.3.1 Partial Discharge Inception Voltage

Partial discharge inception voltage activities under applied direct voltage were first precisely measured with different gap distances in CO_2 as the control gas. Fig. 6.4 shows the obtained typical data for positive and negative applied direct voltage respectively. From Fig. 6.4, it can be seen that the PDIV increased linearly with the

increase of pressure, being monotonously increased in positive and negative polarities. Besides, under the same gap distance and pressure, the positive PDIV was higher than that for negative. For example, when the gap distance was 30mm and the pressure was 3bar(abs.), the positive PDIV was 5.99kV and the negative PDIV was 3.99kV.

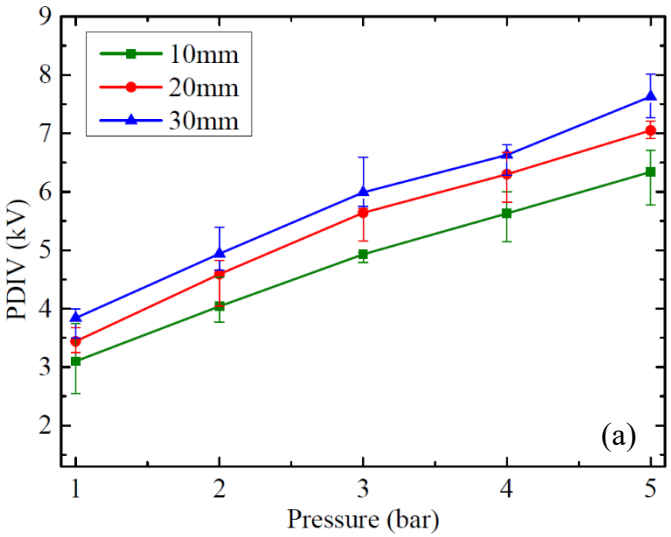

(a) Positive polarity

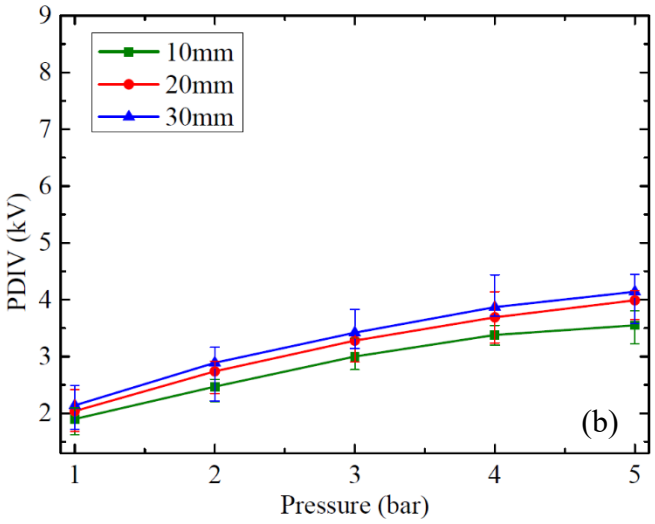

(b) Negative polarity

Fig. 6.4. PDIV with 20μm diameter of needle–plane electrode using CO_2.

The PDIVs for larger tip diameter needle with the tip diameter of 200μm is shown in Fig. 6.5. It can be seen that when increasing the needle sharpness, the PDIV would increase for both positive and negative DC polarity, and the PDIV with larger

tip diameter needle was higher than that with smaller tip diameter needle.

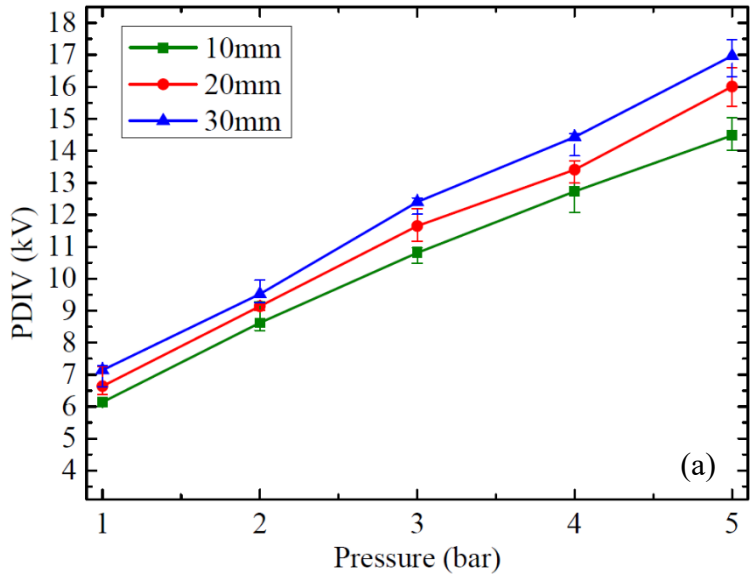

(a) Positive polarity

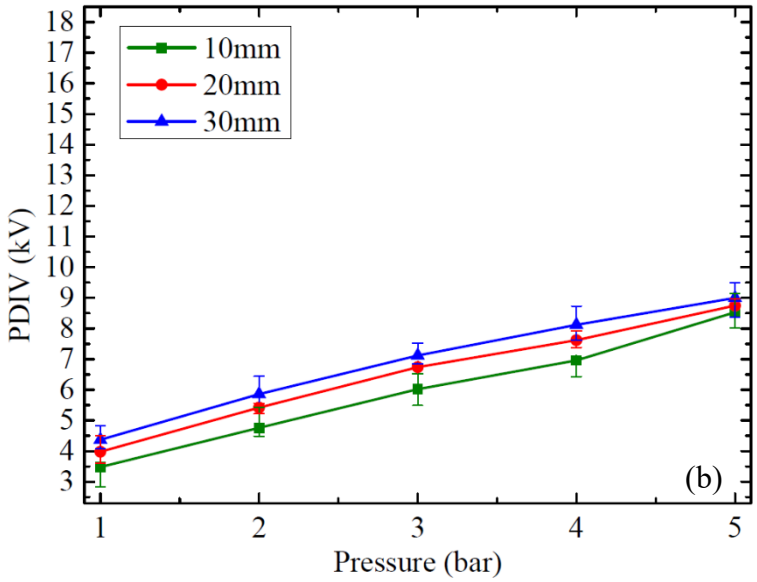

(b) Negative polarity

Fig. 6.5. PDIV with 200µm diameter of needle–plane electrode using CO_2.

Based on the difference in the physical mechanism of the inception of positive and negative partial discharges, the above-mentioned partial discharge characteristics can be well understood. The high-voltage electrode was more likely to be partially activated in the negative polarity than in the positive polarity. When the discharge occurs, the electric field intensity near the tip is the highest. Electrons

are easily emitted in the negative polarity, and secondary electron emission occurs when positive ions collide with the cathode, making the discharge appear first in negative polarity

Experimental PDIV characteristics of 4% C4-PFN/96% CO_2 gas mixture are shown in Fig. 6.6 and Fig. 6.7 for both positive and negative DC polarity and different diameters of needle tips.

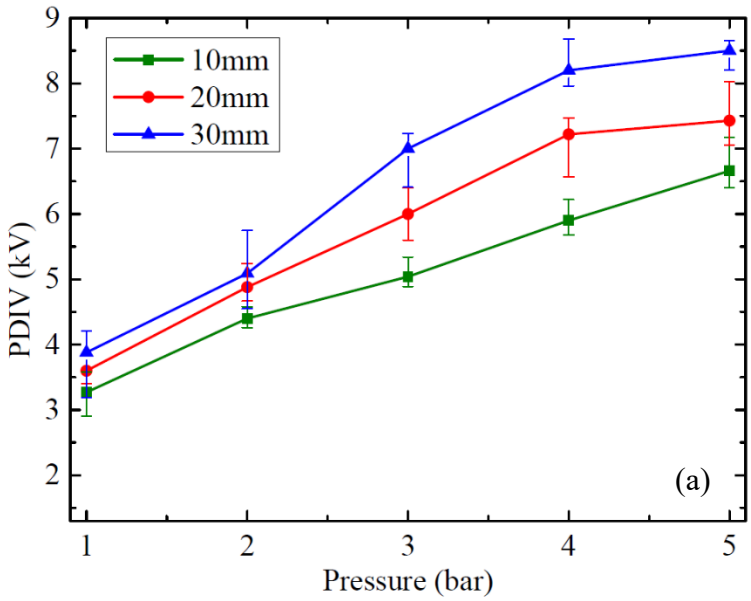

(a) Positive polarity

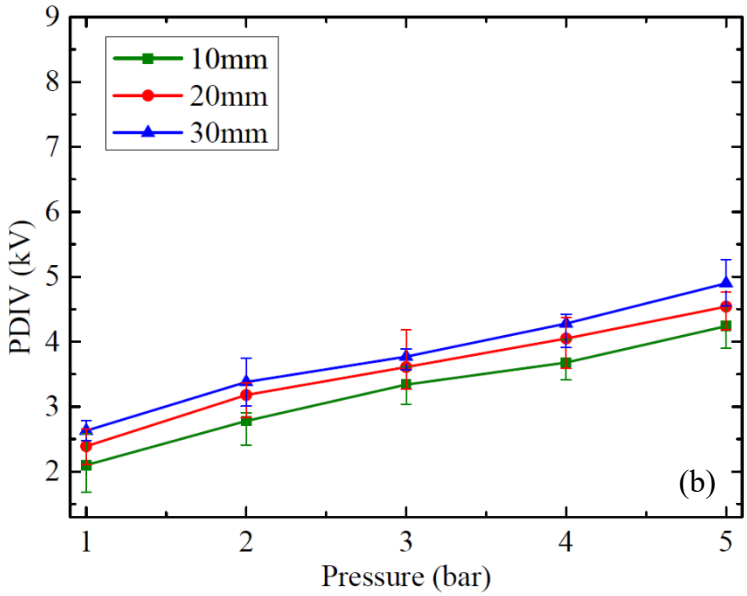

(b) Negative polarity

Fig. 6.6. PDIV with 20µm diameter of needle–plane electrode using 4% C4-PFN/96% CO_2.

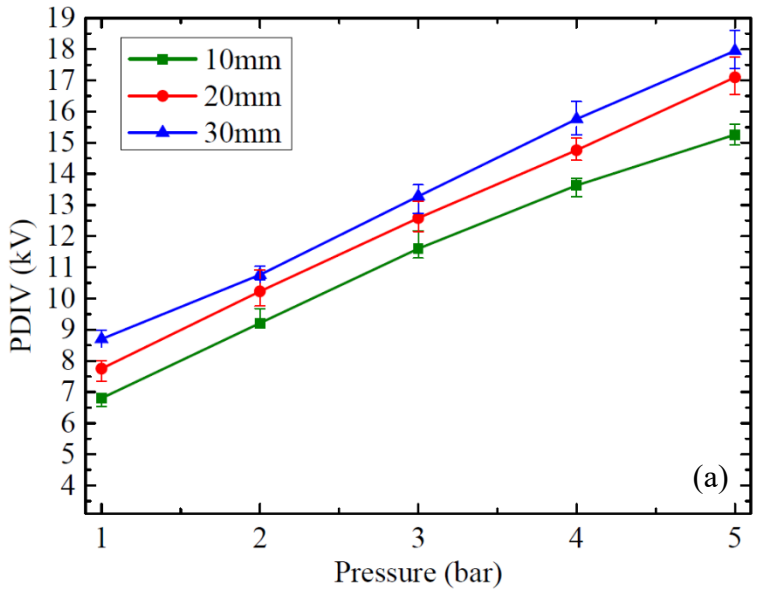

(a) Positive polarity

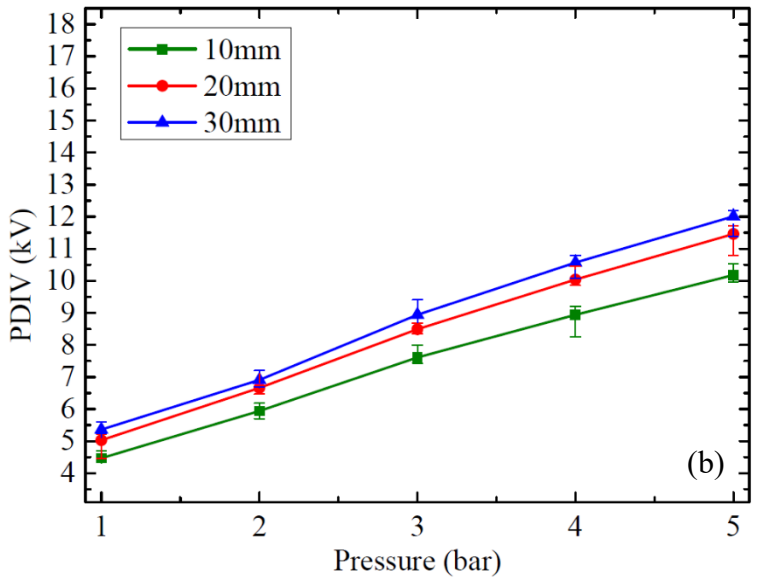

(b) Negative polarity

Fig. 6.7. PDIV with 200µm diameter of needle–plane electrode using 4% C4-PFN/96% CO_2.

For 30% CF_3I/70% CO_2 gas mixture, the experimental results of PDIV are illustrated in Fig. 6.8 and Fig. 6.9 under the same conditions of those of C4-PFN / CO_2 namely under same positive and negative applied direct voltage with different diameter of needle tips. As can be seen, the three different gases investigated had similar a trend of PDIV behaviour, namely, it increased monotonously with the pressure increase for both positive and negative direct voltage. Furthermore, for the

same gap distance and pressure, the positive PDIV was higher than that of negative polarity. Also, when increasing the needle radius, PDIV would increase for both positive and negative DC polarity. However, compared with CO_2, C4-PFN / CO_2 and CF_3I / CO_2 gas mixtures had similar PDIV level which is apparently higher than that of CO_2.

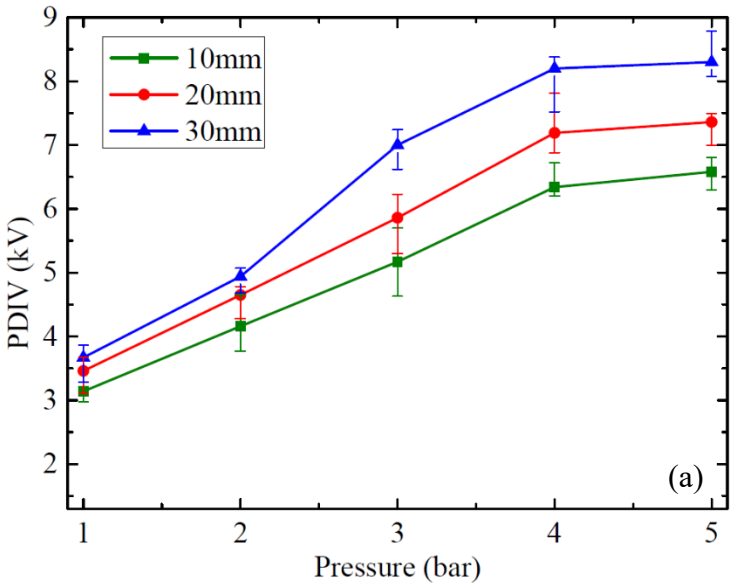

(a) Positive polarity

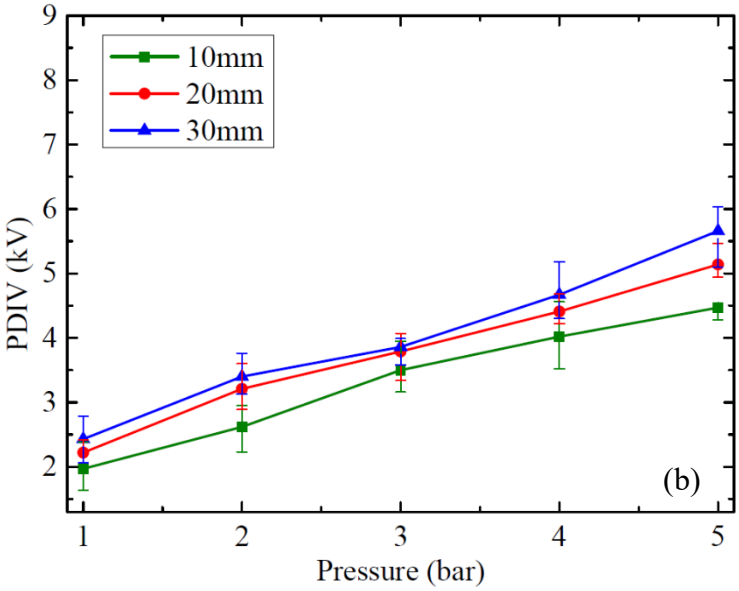

(b) Negative polarity

Fig. 6.8. PDIV with 20µm diameter of needle–plane electrode using 30% CF_3I/70% CO_2.

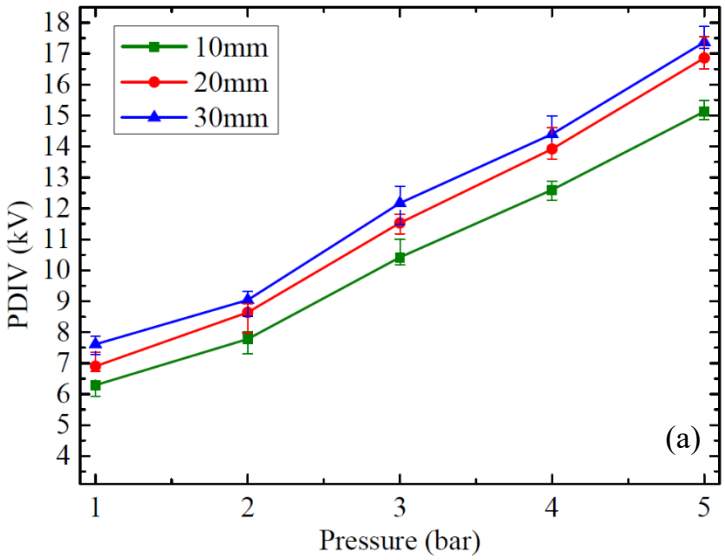

(a) Positive polarity

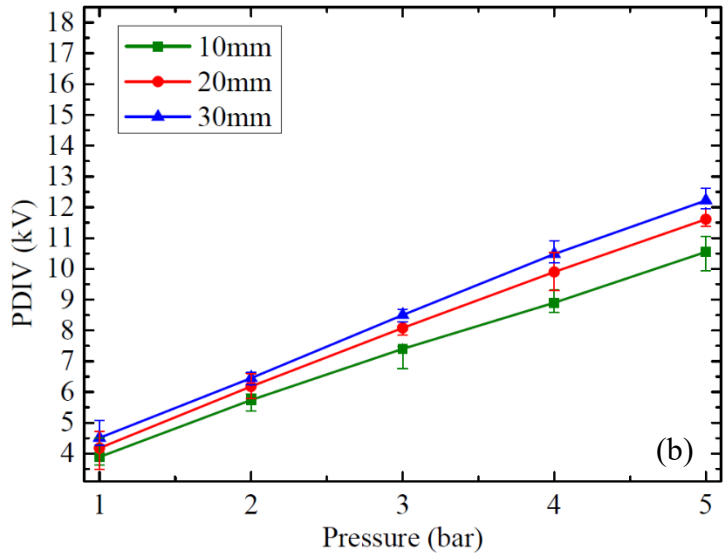

(b) Negative polarity

Fig. 6.9. PDIV with 20μm diameter of needle–plane electrode using 30% CF_3I/70% CO_2.

6.3.3.2 Partial Discharge Current Pulse Waveforms

Fig. 6.10 and Fig. 6.11 show examples of DC partial discharge current pulse signals. As can be seen from Fig. 6.10, for the same gap distance and pressure, the resulting corona discharge current pulse amplitude was higher under negative DC voltage than that under positive DC voltage. The amplitude of the current pulse using CO_2 was much higher than that of C4-PFN / CO_2 and CF_3I / CO_2 gas mixtures. A similar trend had been found when using larger tip diameter needle, taking the

positive DC partial discharge current pulse waveforms with the 200μm diameter as an example, the amplitude of typical partial discharge current pulses were higher than in the case of the smaller tip diameter needle as shown in Fig. 6.11.

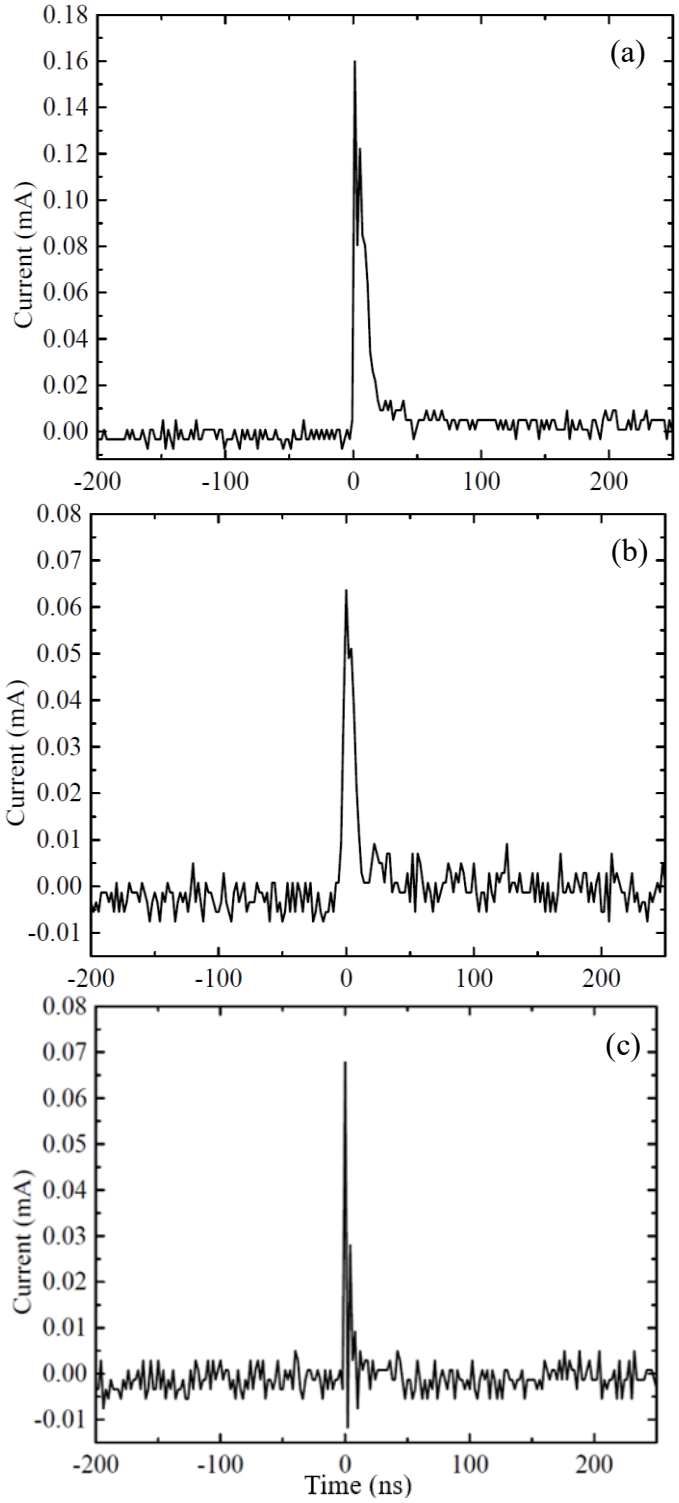

(i) Positive polarity

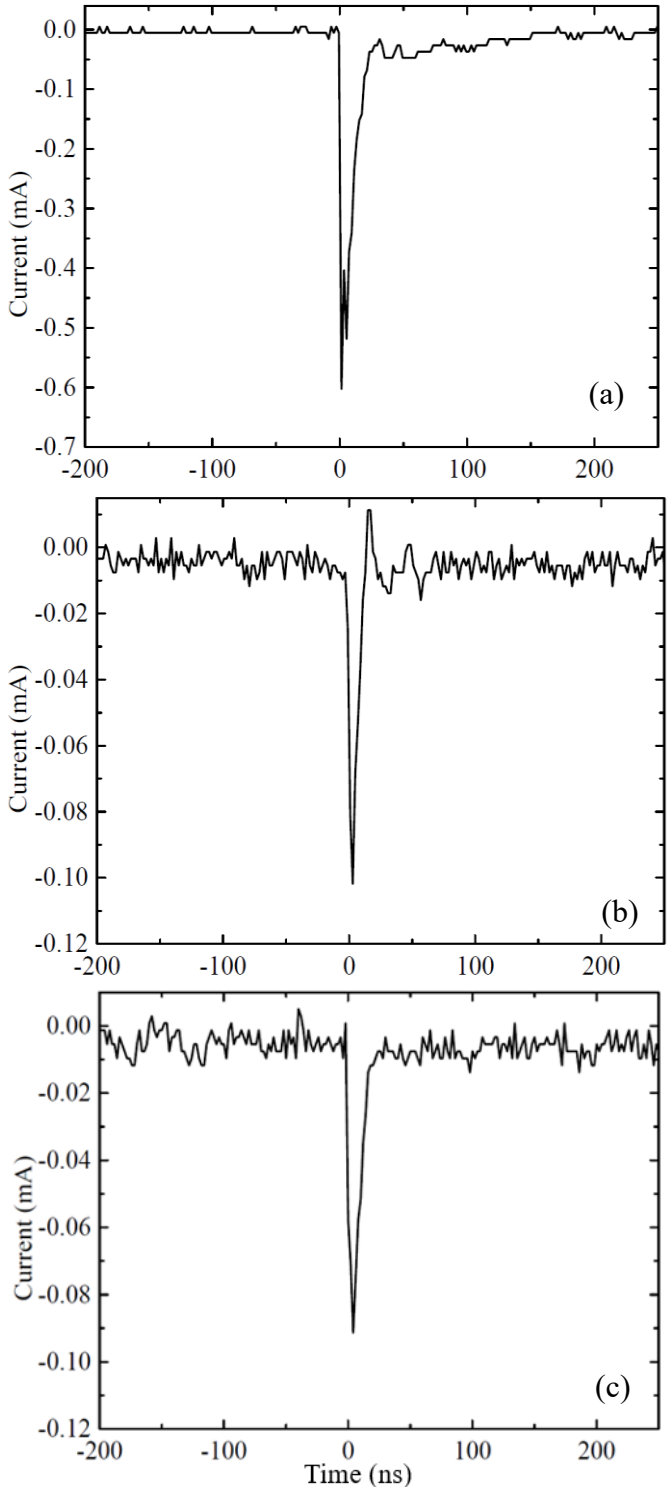

(ii)Negative polarity

Fig. 6.10. (i) Positive polarity and (ii) negative polarity DC partial discharge current pulse waveforms with the 20µm diameter of needle–plane electrode (a) CO_2 (b) 4% C4-PFN /CO_2 (c) CF_3I/CO_2.

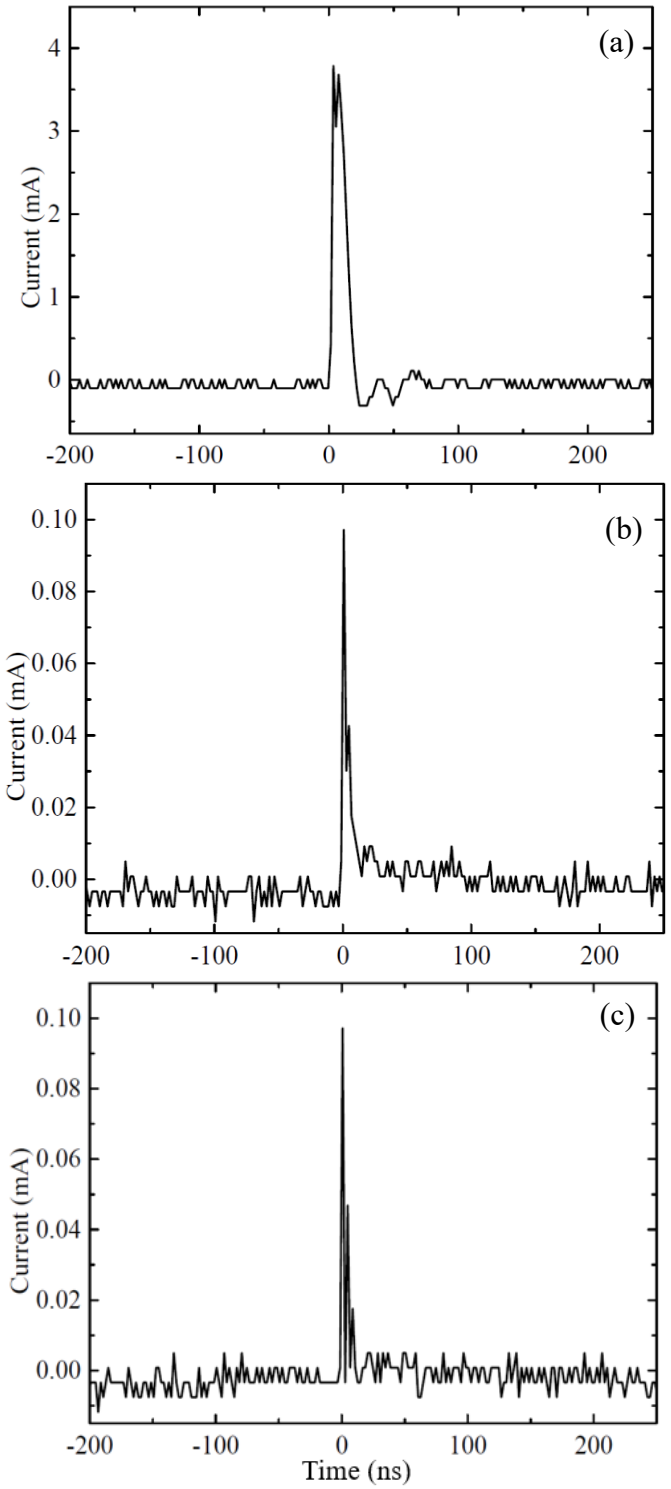

Fig. 6.11. Positive DC partial discharge current pulse waveforms with the 200µm diameter of needle–plane electrode (a) CO_2 (b) 4% C4-PFN /CO_2 (c) CF_3I/CO_2.

6.4 Conclusion

This chapter provides an extensive experimental investigation to verify the

performance of DC spacers models whose shape was optimized through DC electric field calculations where conventional epoxy filled material without temperature gradient influence. The main outcomes can be summarized as follows:

- Reduced scale gas insulated prototype to mimic the full-scale GIL/GIS system was designed and constructed. This setup fulfills the requirements of cleanliness, surface smoothness of the HV electrode and the internal walls of the grounded enclosure, as well as gas tightness. Such prototype construction was very challenging. Three SF_6 alternative gases were utilized in this study which are dry air; 4% C4-PFN/96% CO_2 and 30% CF_3I/70% CO_2.
- The mold of the geometrically optimized spacer was also designed and constructed. The good functionality of this mold was checked through several epoxy vacuum casting trials to get the desired final spacers without any imperfections.
- At constant temperature and under DC voltage testing up to the maximum applicable ±123 kV, where ±119 kV corresponds to ±500 kV of full-size GIL/GIS, the test results showed that the optimized DC spacers made of silica and alumina filled epoxy withstood these voltage levels and did not exhibit any surface flashover. These results confirmed the findings of the electric field simulations and the effectiveness of the optimized DC spacer under uniform temperature. In addition, the utilized SF_6 free alternatives are compatible with the filled epoxy materials of the DC spacers.

Then experimental results of DC partial discharge inception voltage of CO_2, 4% C4-PFN / 96% CO_2 and 30% CF_3I / 70% CO_2 gas mixtures under different pressures, electrode configurations, and gap distances have been presented and discussed. The main outcomes can be summarized as follows:

- At non-uniform electric field, the PDIV of all the three types of gases increased with the increase of the gap distance and the pressure.
- Under the same pressure, gap distance, and electrode configuration, the negative PDIV was lower than the positive PDIV. When the gap distance was

30mm and the pressure was 3bar(abs.), the positive PDIV was 5.99kV and the negative PDIV was 3.99kV.

- Under DC applied voltages with positive and negative polarities at different pressures from 1 to 5 bar (abs.), needle-plane electrode structures with the tip diameter 20±0.5μm and 200±0.5μm, and gap distance varying from 10mm to 30mm, the PDIV level of 4% C4-PFN / 96% CO_2 and 30% CF_3I / 70% CO_2 gas mixtures were essentially equivalent.
- The amplitude of the PD current generated during the discharge inception on CO_2 was higher than the other two gas mixtures. It is worth noting that there is no unified standard for the detection of partial discharge under DC applied voltage, according to IEC60270, current literatures only used current pulse as the indication of the partial discharge, and they did not provide all the pulse data. When the gap distance was 20mm and the pressure was 4bar(abs.), the amplitudes of the positive PD current for 4% C4-PFN / 96% CO_2 and 30% CF_3I / 70% CO_2 gas mixtures with the 20μm diameter of needle–plane electrode were 0.065mA and 0.068mA respectively, while the positive PD current for CO_2 was 0.16mA.

Chapter 7 Conclusion and Future Work

7.1 Conclusions

The spacer is the key component in the gas insulation system, and the discharge caused by the loss of its insulation performance will affect the safety and stability of the entire system. This threat is widespread in both traditional power transmission systems using SF_6 as the insulating medium or gas insulating systems using environmentally friendly gases as the insulating medium. The electric field distribution under HVDC voltage is related to the conductivity of the spacer material, and the conductivity is also related to the temperature. In addition to the influence of electrical conductivity, the shape of the spacer also significantly affects the electric field distribution at the gas, conductor/enclosure, and interface of spacer. However, the current published research on HVDC spacers is limited. It needs the combination of the appropriate spacer shape design and the adjustment of the DC electric conductivity of the spacer's epoxy material by modifying slightly its chemical composition. Besides, testing of HVDC GIS and GIL prototype installations is required to demonstrate the reliability of the systems under real service conditions. Furthermore, the knowledge, the reliability and compatibility of alternatives to SF_6 in some commercial HVAC gas insulated systems under HVDC GIS/GIL gas insulated systems are needed in extensively studied and test verified. This work contributes to simulation study to optimize the geometry of the HVDC spacers. It also identifies suitable new materials. A reduced scale prototype of 500kV GIL is designed and built. Also, a new type of spacer is designed and built. Laboratory tests included withstand tests of the scaled GIL and spacer, and evaluation of performance of with different alternative gas and their mixtures which are contributed to replace SF_6 in the future gas insulated system design.

In this thesis, numerical simulation and experimental studies were carried out for spacers, and the potential substitutes C4-PFN and CF_3I were investigated. Due to the high cost of manufacturing a 500kV DC gas insulation system, a reduced-scale GIL prototype is designed and fabricated, and the electric field distribution is similar to that of a 500kV full-scale GIL. The prototype was then incorporated into the measurement system and gas recovery unit, making it possible to recover the test gas mixture for further use.

The investigation of spacers properties, C4-PFN and CF_3I, and their mixtures were described in Chapter 2. The review revealed that the spacers for HVAC applications at this stage were not suitable for HVDC GIS/GIL applications due to resistive electric field enhancement, charge accumulation on the spacer's surface, flashover under superimposed lightning/switching impulse voltage onto DC operating voltage and metallic particles. Therefore, in the design of GIS/GIL under HVDC applied voltage, the spacers require further consideration. At the same time, the review gave a deeper understanding of the potential substitutes C4-PFN and CF_3I. The two gases have many similar characteristics with SF_6, such as being chemically inert and non-flammable and, due to their good dielectric strength, the application of these two gases is very promising.

In order to study the optimization of spacers, finite element modelling was used in the calculation. A reduced-scale simulation model was developed based on a full-scale 420kV AC GIL. Computational modelling took advantage of the axisymmetric characteristics of the test bench and requires less calculation time.

The spacer was simulated using different materials with and without temperature gradient. The simulation results showed that when there is a temperature gradient between the conductor and the container, the electric field distribution is strongly affected. The novel adopted material FGM was found to be very effective at controlling the enhancement of electric field strength around critical regions. Besides, the change of gas conductivity had little effect on the electric field distribution around the spacer. This research showed that, when the HVDC spacer was manufactured, the shape and material of the spacer need to be optimized.

The shape of spacer was optimized using geometry shape and dimensions parameters and with traditional materials. The results showed that the geometrically optimized spacer model profile was very effective in reducing the electric field enhancement at critical regions under DC applied voltage. The achieved maximum electric field was acceptable or within the allowed range. The existence of a high temperature gradient had a significant impact on the electric field distribution along the surface of the spacer and moved the maximum electric field from the central high-voltage conductor to the grounding enclosure. One of the measures to reduce

the electric field enhancement was to use a new modified filled epoxy resin material, which had weak temperature-dependent conductivity, and lower thermal activation than traditional AC alumina-filled epoxy. When AC standard materials were used, the increase of temperature gradient also led to an enhancement in charge accumulation on the surface of the spacer with the highest surface charge density. New non-linear resistive field grading materials with moderate non-linear coefficients were also effective but seemed not necessary. The optimization of the modified filled epoxy spacer was sufficient to meet the requirements of 500 kV DC GIS/GIL applications.

After optimizing the shape of the spacer, the electric field distribution under direct voltage superimposed lightning impulse voltage was simulated. Under lightning strikes, the charge accumulated on the spacer surface will reduce the insulation strength. Therefore, in order to design a reliable spacer for HVDC applications, it must meet the requirements of direct voltage superimposed lightning impulse voltage.

A new test rig was developed for spacer dielectric strength and gas research work. The reduced-scale GIL prototype has been designed and tested to withstand pressures up to 11 bar (abs), and after each test, the gas is recycled back into the cylinder so that it will not be released into the atmosphere. Since the study of arcing by-products of the alternative gas mixtures is important for future work, this recovery process provides a way to obtain the degraded gas under study.

The optimized spacer was designed and manufactured, and withstand tests were carried out on the reduced-scale prototype. Before installing the spacers, withstand tests using dry air, 4% C4-PFN / 96% CO_2, 30% CF_3I / 70% CO_2 were carried out to ensure the reliability of the test setup. Two different spacer materials, silica-filled epoxy and alumina-filled epoxy were subsequently subjected to withstand tests. Experimental results showed that the optimization of the shape and material of the insulator can meet the needs of future HVDC gas insulated system, and C4-PFN and CF_3I are also feasible as substitutes for replacing the usage of SF_6.

Experiments were conducted on CO_2, and a gas mixture of 4% C4-PFN/96% CO_2, 30% CF_3I/70% CO_2, and under non-uniform electric field, using two different

electrode configurations to investigate the partial discharge inception voltage under different pressures, different electrode distance, and different applied voltage polarities. The experimental results showed that the PDIV of all the three types of gases increased with the increase of the gap distance and the pressure. Under the same pressure, gap distance, and electrode configuration, the negative PDIV is lower than the positive PDIV. Under the same test conditions, the PDIV level of 4% C4-PFN/96% CO_2 and 30% CF_3I/70% CO_2 gas mixtures are essentially equivalent. The amplitude of the PD current generated during the discharge inception on CO_2 is higher than the other two gas mixtures.

7.2 Future Work

Based on the work carried out in this research, the following areas have been identified that can be used for related future investigations:

a) Withstand tests under DC applied voltage with the presence of the temperature gradient:

In this thesis, the withstand tests were carried out to verify the performance of the optimized spacer model under DC applied voltage without the temperature gradient. It would be useful to carry out continuous experiments with the presence of temperature gradient. A heating system with a real-time temperature indicator applied to the conductor could be engineered to further evaluate the performance of the results of spacers optimization.

b) Presence of metal particles on the spacer surface:

The metal particles attached to the surface of the spacer will increase the local electric field near the spacer and reduce the insulation of the system. Therefore, analyzing the influence of different factors on the flashover voltage along the surface of the spacer under the conditions of particle size, pressure, voltage polarity and particle attachment position is of great significance to reduce the insulation loss caused by metal particles to the gas insulation system.

c) Flashover test:

The surface flashover voltage measurement for spacers of different materials can be analyzed from the influence of different electrode shapes, humidity, and surface roughness, which can provide further reference for the optimization of spacers in gas insulation systems in the future.

d) Investigation of arcing by-products:

The decomposition products of C4-PFN and CF_3I after discharge under DC voltage can be detected. The samples collected before and after the discharge can be tested, which cannot only effectively analyze the types of discharge products, but also quantitatively analyze the toxicity of the gas. The insulation performance, greenhouse effect and toxicity of gaseous decomposition products are all important indicators for evaluating the ability of gas mixtures to replace SF_6, and its degree pf toxicity is important to protect health.

References

[1] T. Hasegawa, K. Yamaji, M. Hatano, F. Endo, T. Rokunohe and T. Yamagiwa, “Development of Insulation Structure and Enhancement of Insulation Reliability of 500 kV DC GIS”. *IEEE Transactions on Power Delivery*, vol. 12, no. 1, pp. 194-202, Jan. 1997.

[2] T. Sakai, T. Furuyashiki, K. Kato and H. Okubo, “Electric Field Analysis and Electrical Insulation Performance for Solid Insulator in HVDC Gas Insulated Switchgear”. In Proceedings of *the International Symposium on High Voltage Engineering (ISH)*, Pilsen, Czech Republic, pp. 23–28 Aug. 2015.

[3] Intergovernmental Panel on Climate Change (IPCC), Working Group I Contribution to Fourth Assessment Report of the IPCC - Intergovernmental Panel on Climate Change, Geneva, Switzerland: Addendum-Errata of Climate Change2007-The Physical Science Basis IPCC WG1 AR4 Report, 2008.

[4] A. Singhasathein, A. Pruksanubal, N. Tanthanuch and W. Rungseevijitprapa, “Dielectric Strength of Breakdown Voltage of Nitrogen and Carbon-dioxide”. 2013 10th International Conference on Electrical Engineering/Electronics, Computer, Telecommunications and Information Technology, Krabi, Thailand, 2013, pp. 1-5.

[5] J. G. Owens, “Greenhouse gas emission reductions through use of a sustainable alternative to SF_6.” IEEE Electric Insulation Conference, 2016, pp. 535–538.

[6] L. Chen, P. Widger, M. S. Kamarudin, H. Griffiths and A. Haddad, “CF_3I Gas Mixtures: Breakdown Characteristics and Potential for Electrical Insulation”. *IEEE Transactions on Power Delivery*, vol. 32, no. 2, pp. 1089-1097, April 2017.

[7] “GIL – Power Transmission Technology for the 245 to 550 kV Range”. [Online]. Available: www.siemens.de/hv-gil [Accessed: 01-Mar-2021].

[8] M. Morcos and K. D. Srivastava, “On Electrostatic Trapping of Particle Contamination in GITL Systems”. *IEEE Transactions on Power Delivery*, vol. 7, no. 4, pp. 1698-1705, Oct. 1992.

[9] H. Koch, *Gas-Insulated Transmission Lines*. Chichester, UK: John Wiley & Sons, Ltd, 2011.

[10] M. Mendik, S. M. Lowder and F. Elliott, “Long Term Performance Verification of High Voltage DC GIS”. *1999 IEEE Transmission and Distribution Conference*, vol.2, pp. 484-488, 1999.

[11] T. Nitta and K. Nakanishi, “Charge Accumulation on Insulating Spacers for HVDC GIS”. *IEEE Transactions on Electrical Insulation*, vol. 26, no. 3, pp. 418-427, June 1991.

[12] T. Hasegawa, K. Yamaji, M. Hatano, H. Aoyagi, Y. Taniguchi and A. Kobayashi, “DC Dielectric Characteristics and Conception of Insulation Design for DC GIS”. *IEEE Transactions on Power Delivery*, vol. 11, no. 4, pp. 1776-1782, Oct. 1996.

[13] T. Shimato, T. Hashimoto, and M. Sampei. “The Kii Channel HVDC link in Japan”. *CIGRE*, no. 14- 106, Japan, 2002.

[14] S. Okabe, G. Ueta, T. Utsumi and J. Nukaga, “Insulation Characteristics of GIS Insulators under Lightning Impulse with DC Voltage Superimposed”. *IEEE Transactions on Dielectrics and Electrical Insulation*, vol. 22, no. 6, pp. 1-9, December 2015.
[15] S. Okabe, G. Ueta and K. Nojima, “Insulation Characteristics of GIS Epoxy Insulators with Non-uniform Surface Resistance under DC Voltage”. *IEEE Transactions on Dielectrics and Electrical Insulation*, vol. 22, no. 1, pp. 516-525, Feb. 2015.
[16] U. Riechert, U. Straumann and R. Gremaud, “Compact Gas-insulated Systems for High Voltage Direct Current Transmission: Basic Design”. *2016 IEEE/PES Transmission and Distribution Conference and Exposition*, pp. 1-5, 2016.
[17] C. Li et al., “Novel HVDC Spacers by Adaptively Controlling Surface Charges – Part I: Charge Transport and Control Strategy”. *IEEE Transactions on Dielectrics and Electrical Insulation*, vol. 25, no. 4, pp. 1238-1247, Aug. 2018.
[18] M. Tenzer, H. Koch and D. Imamovic, “Compact Systems for High Voltage Direct Current Transmission”. *International ETG Congress*, pp. 1-6, 2015.
[19] Siemens Energy. Gas-insulated DC Switchgear (DC GIS). Available online: https://www.siemens-energy.com/global/en/offerings/power-transmission/transmission-products/gas-insulated/dc-gis.html (accessed on 24 October 2020).
[20] T. Magier, M. Tenzer and H. Koch, “Direct Current Gas-Insulated Transmission Lines”. *IEEE Transactions on Power Delivery*, vol. 33, no. 1, pp. 440-446, Feb. 2018.
[21] M. Tenzer, H. Koch and D. Imamovic, “Underground Transmission Lines for High Power AC and DC Transmission”. *2016 IEEE/PES Transmission and Distribution Conference and Exposition (T&D)*, pp. 1-4, 2016.
[22] T. Sorquist and A. E. Vlastos, “Outdoor Polymeric Insulators Long-term Exposed to HVDC”. *Proceedings of 1996 Transmission and Distribution Conference and Exposition*, pp. 135-142 1996.
[23] J. Kuffel, E. Kuffel, and W. S. Zaengl, *High voltage engineering fundamentals*, Newnes, 2000.
[24] N. Zebouchi and M. A. Haddad, “A Review on Real-Size Epoxy Cast Resin Insulators for Compact High Voltage Direct Current Gas Insulated Switchgears (GIS) and Gas Insulated Transmission Lines (GIL)—Current Achievements and Envisaged Research and Development”. *Energies*, 13, 6416, 2020.
[25] J. Reilly, R. Prinn, J. Harnisch, J. Fitzmaurice, H. Jacoby, D. Kicklighter, J. Melillo, P. Stone, A. Sokolov and C. Wang, “Multi-gas Assessment of the Kyoto Protocol”. *Nature,* 401(549–555), 1999.
[26] X. Zhang, H. Xiao, J. Tang, Z. Cui and Y. Zhang, “Recent Advances in Decomposition of the Most Potent Greenhouse Gas SF_6”. *Critical Reviews in Environmental Science and Technology* 47(18), 1763-1782, 2017.
[27] H. Katagiri, H. Kasuya, H. Mizoguchi and S. Yanabu, “Investigation of the Performance of CF_3I Gas as a Possible Substitute for SF_6”. *IEEE Transactions on Dielectrics and Electrical Insulation*, vol. 15, no. 5, pp. 1424-1429, Oct. 2008.

[28] L. G. Christophorou, J. K. Olthoff and R. J. Van Brunt, “Sulfur Hexafluoride and the Electric Power Industry”. *IEEE Electrical Insulation Magazine*, vol. 13, no. 5, pp. 20-24, Sep.-Oct. 1997.
[29] X. Zhang et al. “Theoretical Study of the Interaction of SF_6 Molecule on Ag (1 1 1) Surfaces: A DFT study”. *Applied Surface Science*, vol. 457, pp. 745-751, 2018.
[30] Z. Zheng et al., “Compatibility between C_4F_7N and the Sealing Material EPDM Used in GIL”. *2019 IEEE Conference on Electrical Insulation and Dielectric Phenomena (CEIDP)*, pp. 146-149, 2019.
[31] R. Zhong et al., “Insulation characteristics of CF_3I/c-C_4F_8/N_2 Gas Mixtures in Slightly Non-uniform Electric Field”. *IEEE Transactions on Dielectrics and Electrical Insulation*, vol. 25, no. 4, pp. 1371-1379, August 2018.
[32] L. G. Christophorou and J. K. Olthoff, “Electron Interactions with SF_6”. *Journal of Physical and Chemical Reference Data,* vol.29, pp.267-330, 2000.
[33] D. Koch, “SF_6 Properties, and Use in MV and HV Switchgear”. *Schneider Electric*, cahier technique no.188, pp.3–22, 2003.
[34] “3M™ Novec™ 4710 Insulating Gas”. [Online]. Available: https://www.3m.co.uk/3M/en_GB/p/d/b40006511/ [Accessed: 13-09-2020]
[35] L. Yi, et al. “Experimental Study on the Partial Discharge and AC Breakdown Properties of C_4F_7N/CO_2 mixture”. *High Voltage*, vol. 4.1, pp. 12-17, 2019.
[36] Subcommittee on Iodotrifluoromethane, *Iodotrifluoromethane*: *Toxicity Review*. Washington, USA: The National Academies Press, 2004.
[37] Climate Change 1995-The Science of Climate Change. *Contribution of Working Group I to the Second Assessment Report of the Intergovernmental Panel on Climate Change (IPCC),* the Press Syndicate of the University of Cambridge, 1996.
[38] “Safety Data Sheet of SF_6”, [online] Available: https://www.alsafetydatasheets.com/download/se/Sulphur_hexafluoride-SE_ENG.pdf [Accessed: 05-12-2023]
[39] Z. Peng et al., “Gas Sensor Based on Semihydrogenated and Semifluorinated h-BN for SF_6 Decomposition Components Detection”. *IEEE Transactions on Electron Devices*, vol. 68, no. 4, pp. 1878-1885, April 2021.
[40] “Safety Data Sheet of 3M™ Novec™ 4710”, [Online]. Available: https://multimedia.3m.com/mws/mediawebserver?mwsId=SSSSSuUn_zu8l00xmxmBmxmSOv70k17zHvu9lxtD7SSSSSS-- [Accessed: 13-09-2021]
[41] Y. Li et al., “Assessment on the Toxicity and Application Risk of C_4F_7N: A New SF_6 Alternative Gas”. *Journal of Hazardous Materials*, vol. 368, pp. 653-660, 2019.
[42] S. Xia et al. “Review of Decomposition Characteristics of Eco-Friendly Gas Insulating Medium for High-Voltage Gas-Insulated Equipment”. *Journal of Physics D: Applied Physics*, 54(37): 373002, 2021.
[43] Subcommittee on Iodotrifluoromethane, Iodotrifluoromethane: Toxicity Review, Washington, USA: The National Academies Press, 2004.
[44] P. Widger, M. Haddad, “Analysis of Gaseous By-Products of CF_3I and CF_3I-CO_2 after High Voltage Arcing Using a GCMS”. *Molecules*, *24*, 1599, 2019.
[45] T. Nitta and K. Nakanishi, “Charge Accumulation on Insulating Spacers for HVDC GIS”. *IEEE Transactions on Electrical Insulation*, vol. 26, no. 3, pp. 418-427, 1991.

[46] T. Hasegawa, K. Yamaji, M. Hatano, H. Aoyagi, Y. Taniguchi and A. Kobayashi, “DC Dielectric Characteristics and Conception of Insulation Design for DC GIS”. *IEEE Transactions on Power Delivery*, vol. 11, no. 4, pp. 1776-1782, Oct. 1996.
[47] T. Hasegawa, K. Yamaji, M. Hatano, F. Endo, T. Rokunohe and T. Yamagiwa, “Development of Insulation Structure and Enhancement of Insulation Reliability of 500 kV DC GIS”. *IEEE Transactions on Power Delivery*, vol. 12, no. 1, pp. 194-202, 1997.
[48] E. Volpov, “Dielectric Strength Coordination and Generalized Spacer Design Rules for HVAC/DC SF_6 Gas Insulated Systems”. *IEEE Transactions on Dielectrics and Electrical Insulation*, vol. 11, no. 6, pp. 949-963, 2004.
[49] A. De Lorenzi et al. “The Insulation Structure of the 1MV Transmission Line for the ITER Neutral Beam Injector”. *Fusion Engineering and Design*, vol. 82, no. 5, pp. 836–844, 2007.
[50] Z. Jia, B. Zhang, X. Tan and Q. Zhang, “Flashover Characteristics along the Insulator in SF_6 Gas under DC Voltage”. *2009 Asia-Pacific Power and Energy Engineering Conference*, pp. 1-4, 2009.
[51] R. Gremaud, et.al “Solid Insulation in DC Gas-Insulated Systems”. *CIGRE Conference*, Paris, France, 2014.
[52] A. Winter and J. Kindersberger, “Transient Field Distribution in Gas-solid Insulation Systems under DC Voltages”. *IEEE Transactions on Dielectrics and Electrical Insulation*, vol. 21, no. 1, pp. 116-128, 2014.
[53] B. Du, H. Liang, J. Li and Z. Ran, “Electrical Field Distribution along SF_6/N_2 Filled DC-GIS/GIL Epoxy Spacer”. *IEEE Transactions on Dielectrics and Electrical Insulation*, vol. 25, no. 4, pp. 1202-1210, 2018.
[54] B. Zhang, Y. Guo, Y. Yao, Z. Wang, H. Zhang and G. Jin, “Charge Transport and Accumulation around the Cone-type Insulator in SF_6-filled 550 kV DC GIL”. *The Journal of Engineering*, 2610–2614, 2019.
[55] W. Li, X. You, H. Mu, J. Deng and G. Zhang, “Numerical Optimization and 3D-printing Fabrication Concept of High Voltage FGM Insulator”. *2015 IEEE PES Asia-Pacific Power and Energy Engineering Conference (APPEEC)*, pp. 1-4, 2015.
[56] N. Hayakawa, Y. Miyaji, H. Kojima and K. Kato, “Simulation on Discharge Inception Voltage Improvement of GIS Spacer with Permittivity Graded Materials (ε-FGM) using Flexible Mixture Casting Method”. *IEEE Transactions on Dielectrics and Electrical Insulation*, vol. 25, no. 4, pp. 1318-1323, 2018.
[57] N. Hayakawa, R. Oishi, H. Kojima, K. Kato and N. Zebouchi, “Electric Field Grading by Functionally Graded Materials (FGM) for HVDC Gas Insulated Power Apparatus”. *2018 IEEE Conference on Electrical Insulation and Dielectric Phenomena (CEIDP)*, pp. 309-312, 2018.
[58] Rachmawati et al., “Electric Field Grading by Permittivity and Conductivity Graded Materials (ε/σ-FGM) for HVDC Gas Insulated Power Apparatus”. *2020 International Symposium on Electrical Insulating Materials (ISEIM)*, pp. 421-424,2020.
[59] H. Koch, D. Imamovic, B. Lutz, K. Juhre, T. Neidhart, R.D. Rogler, “High Power Underground Transmission for HVDC”. *Proceedings of the CIGRE Conference*, Paris, France, pp.22-26, 2016.

[60] T. Vu-Cong, L. Zavattoni, P. Vinson, A. Girodet, “DC GIS: Importance of Simulations for the Design and Testing”. *CIGRE*, Paris, 2016.
[61] U. Riechert, R. Gremaud, S. Thorson, M. Callavik, “Application Options and Electrical Field Studies as Basis for Adequate Testing of Gas-insulated Systems for HVDC”. *Proceedings of the CIGRE Winnipeg 2017 Colloquium Study Committees*, vol.3, Canada, 2017.
[62] J. Koo, et al. “Modeling and Simulation of HVDC Epoxy Spacer for SF_6 Gas Insulated System”. *Proceedings of the International Symposium on High Voltage Engineering (ISH)*, pp. 23-28, Pilsen, Czech Republic. 2015.
[63] R. Nakane, K. Takabayashi, K. Kato and H. Okubo, “Electrical Insulation Performance of HVDC-GIS Spacer under Various Testing Conditions”. *2017 IEEE Conference on Electrical Insulation and Dielectric Phenomenon (CEIDP)*, pp. 621-624, 2017.
[64] A. Winter, et al. “Solid/gaseous Insulation Systems for Compact HVDC Solutions”. *45 CIGRE Session 2014*. 2014.
[65] K. Nakanishi, A. Yoshioka, Y. Arahata and Y. Shibuya, “Surface Charging on Epoxy Spacer at DC Stress in Compressed SF_6 gas”. *IEEE Transactions on Power Apparatus and Systems*, vol. PAS-102, no. 12, pp. 3919-3927, Dec. 1983.
[66] S. Sato, W. S. Zaengl and A. Knecht, “A Numerical Analysis of Accumulated Surface Charge on DC Epoxy Resin Spaces”. *IEEE Transactions on Electrical Insulation*, vol. EI-22, no. 3, pp. 333-340, June 1987.
[67] N. H. Malik and A. H. Qureshi, “A Review of Electrical Breakdown in Mixtures of SF_6 and Other Gases”. *IEEE Transactions on Electrical Insulation*, vol. EI–14, no.1, pp.1–13, 1979.
[68] J. C. Devins, “Replacement Gases for SF_6”. *IEEE Transactions on Electrical Insulation*, vol. EI-15, no. 2, pp. 81-86, 1980.
[69] F. A. M. Rizk and M. B. Eteiba, “Impulse Breakdown Voltage-Time Curves of SF_6 and SF_6-N_2 Coaxial-Cylinder Gaps”. *IEEE Transactions on Power Apparatus and Systems*, vol. PAS-101, no. 12, pp. 4460-4471, 1982.
[70] R. S. Nema, S. V. Kulkarni, and E. Husain, “On Calculation of Breakdown Voltages of Mixtures of Electron Attaching Gases”. *IEEE Transactions on Electrical Insulation*, vol. EI–17, no.5, pp.434–440, 1982.
[71] N. H. Malik and A. H. Qureshi, “Breakdown Gradients in SF_6-N_2, SF_6-Air and SF_6-CO_2 Mixtures”. *IEEE Transactions on Electrical Insulation*, vol. EI–15, no.5, pp.413–418, 1980.
[72] T. Takuma, S. Hamada and O. Yamamoto, “Application of a Gas Mixture with c-C_4F_8 in Gas Insulation”. *1999 Eleventh International Symposium on High Voltage Engineering*, pp. 197-200 vol.3, 1999.
[73] X. Liu, J. Wang, Y. Wang, Z. Zhang and D. Xiao, “Analysis of the Insulation Characteristics of c-C_4F_8/CO_2 Gas Mixtures by the Monte Carlo Method” *Journal of Physics D: Applied Physics*, 41.1, 2008.
[74] X. Li, H. Zhao, J. Wu and S. Jia, “Analysis of the Insulation Characteristics of CF_3I Mixtures with CF_4, CO_2, N_2, O_2 and Air”. *Journal of Physics D: Applied Physics*, 46.34, 2013.
[75] J. D. Mantilla, N. Gariboldi, S. Grob and M. Claessens, “Investigation of the Insulation Performance of a New Gas Mixture with extremely Low GWP”. *2014 IEEE Electrical Insulation Conference (EIC)*, pp. 469-473, 2014.

[76] M. Hyrenbach and S. Zache, “Alternative Insulation Gas for Medium-voltage Switchgear”. *2016 Petroleum and Chemical Industry Conference Europe (PCIC Europe)*, pp. 1-9, 2016.

[77] H. E. Nechmi, A. Beroual, A. Girodet and P. Vinson, “Fluoronitriles/CO_2 Gas Mixture as Promising Substitute to SF_6 for Insulation in High Voltage Applications”. *IEEE Transactions on Dielectrics and Electrical Insulation*, vol. 23, no. 5, pp. 2587-2593, October 2016.

[78] Y. Tu, Y. Cheng, C. Wang, X. Ai, F. Zhou and G. Chen, “Insulation Characteristics of Fluoronitriles/CO_2 Gas Mixture under DC Electric Field”. *IEEE Transactions on Dielectrics and Electrical Insulation*, vol. 25, no. 4, pp. 1324-1331, August 2018.

[79] L. Chen, H. Griffiths, A. Haddad and M. S. Kamarudin, “Breakdown of CF_3I Gas and its Mixtures under Lightning Impulse in Coaxial-GIL Geometry”. *IEEE Transactions on Dielectrics and Electrical Insulation*, vol. 23, no. 4, pp. 1959-1967, August 2016.

[80] M. N. Ngoc, A. Denat, N. Bonifaci, O. Lesaint, W. Daoud and M. Hassanzadeh, “Electrical Breakdown of CF_3I and CF_3I-N_2 Gas Mixtures”. *2009 IEEE Conference on Electrical Insulation and Dielectric Phenomena*, pp. 557-560, 2009.

[81] Y. Tu, Y. Luo, C. Wang, S. Luo, and Y. Cheng, “Breakdown Characteristics of CF_3I and CF_3I/N_2 Gas Mixtures in Uniform Field”. *2015 IEEE 11th International Conference on the Properties and Applications of Dielectric Materials (ICPADM)*, pp. 520-523, 2015.

[82] L. Zavattoni, C. Vu, P. Vinson and A. Girodet, “Leakage Current Measurements in Direct Current Gas Insulated Substations Equipment”. *2016 IEEE International Conference on Dielectrics (ICD)*, pp. 860-863, 2016.

[83] R. Kochetov, T. Andritsch, P. H. F. Morshuis and J. J. Smit, “Thermal and Electrical Behavior of Epoxy-based Microcomposites Filled with Al_2O_3 and SiO_2 Particles”. *2010 IEEE International Symposium on Electrical Insulation*, pp. 1-5, 2010.

[84] E. Volpov, “Electric Field Modeling and Field Formation Mechanism in HVDC SF_6 Gas Insulated Systems”. *IEEE Transactions on Dielectrics and Electrical Insulation*, vol. 10, no. 2, pp. 204-215, April 2003.

[85] H. Yahyaoui, P. Notingher, S. Agnel, Y. Kieffel and A. Girodet, “Analysis of Conduction Mechanisms in Alumina-filled Epoxy Resin under DC Field and Temperature”. *2013 Annual Report Conference on Electrical Insulation and Dielectric Phenomena*, pp. 667-670, 2013.

[86] R. Gremaud, Z. Zhao and M. Baur, “Measurement of DC Conduction in Alumina-filled Epoxy”. *2016 IEEE International Conference on Dielectrics (ICD)*, pp. 1097-1101, 2016.

[87] I. Kwon, J. Koo, H. Lee, J. Koo and B. Lee, “DC Electric Field Control of Ending Box-Air (EB-A) Type Outdoor Termination Under DC Voltage Stress”. *20th International Symposium on High Voltage Engineering*, 2017.

[88] S. Blatt and V. Hinrichsen, “Mathematical Model for Numerical Simulation of Current Density in Microvaristor Filled Insulation Materials”. *IEEE Transactions on Dielectrics and Electrical Insulation*, vol. 22, no. 2, pp. 1161-1170, April 2015.

[89] M. Hering, K. Juhre, M. Secklehner and V. Hinrichsen, “Requirements on

Solid Insulating Materials and Gas-solid Interfaces in Compact HVDC Gas-insulated Systems". *Proceedings of the International Symposium on High Voltage Engineering*, 2017.

[90] M. Tenzer, M. Secklehner and V. Hinrichsen, "Short and Long Term Behavior of Functionally Filled Polymeric Insulating Materials for HVDC Insulators in Compact Gas-insulated Systems". *Proceedings of the Nordic Insulation Symposium*, no. 23, 2013.

[91] A. Winter, J. Kindersberger, V. Hinrichsen, D. Imamovic, and M. Tenzer, "Compact Gas-Solid Insulating Systems for High-Field-Stress in HVDC applications". *CIGRE Study Committee B3&D1 Colloquium, Brisbane*, Australia, September 2013.

[92] R. Kochetov, T. Andritsch, P. H. F. Morshuis and J. J. Smit, "Thermal and Electrical Behavior of Epoxy-based Microcomposites filled with Al_2O_3 and SiO_2 Particles" *2010 IEEE International Symposium on Electrical Insulation*, pp. 1-5, 2010.

[93] S. Qin and S. Boggs, "Design Considerations for High Voltage DC Components". *IEEE Electrical Insulation Magazine*, vol. 28, no. 6, pp. 36-44, Nov.-Dec. 2012.

[94] E. Martensson, B. Nettelbled, U. Gafvert and L. Palmqvist, "Electrical Properties of Field Grading Materials with Silicon Carbide and Carbon Black". *ICSD'98. Proceedings of the 1998 IEEE 6th International Conference on Conduction and Breakdown in Solid Dielectrics*, pp. 548-552, 1998.

[95] T. Sorqvist, T. Christen, M. Jeroense, V. Mondiet and R. Papazyan, "HVDC Light Cable Systems-Highlighting the accessories". *21st Nordic Insulation Symposium (Nordis 2009)*, 2009.

[96] E. Volpov, "Dielectric Strength Coordination and Generalized Spacer Design Rules for HVAC/DC SF_6 Gas Insulated Systems". *IEEE Transactions on Dielectrics and Electrical Insulation*, Vol. 11, No. 6, pp. 949 – 962, 2004,

[97] R. Nakane, K. Takabayashi, K. Kato and H. Okubo, "Electric Field Analysis and Electrical Insulation Performance for Gas-solid Composite Insulation in HVDC GIS". *International Symposium on High Voltage Engineering (ISH)*, 2017

[98] H. Zhou, G. Ma, C. Li, C. Shi and S. Qin, "Impact of Temperature on Surface Charges Accumulation on Insulators in SF_6-filled DC-GIL". *IEEE Transactions on Dielectrics and Electrical Insulation*, vol. 24, no. 1, pp. 601-610, Feb. 2017.

[99] S. Xiao, X. Zhang, J. Tang, S. Liu, "A review on SF_6 substitute gases and research status of CF_3I gases". *Energy Reports,* **2018,** 4, 486-496.

[100] Q. Lin, S. Zhao, D. Xiao, B. Zhou, "Breakdown characteristics of $CF_3I/N_2/CO_2$ mixture in power frequency and lightning impulse voltages". *Plasma Science and Technology,* **2019,** 21, (1), 8.

[101] J. Brisset, J. Pawlat, "Chemical effects of air plasma species on aqueous solutes in direct and delayed exposure modes: discharge, post-discharge and plasma activated water". *Plasma Chemistry and Plasma Process.* **2016,** 36, (2), 355-381.

[102] J. Lowke, "Theory of electrical breakdown in air - the role of metastable oxygen molecules". *Journal of Physics D-Applied Physics* **1992,** 25, (2), 202-210.

[103] D. Smith, P. Spanel, "Selected ion flow tube mass spectrometry (SIFT-MS) for on-line trace gas analysis". *Mass spectrometry reviews,* **2005,** 24, (5), 661-700.
[104] A. Likhanskii, M. Shneider, S. Macheret and R. Miles, "Modeling of dielectric barrier discharge plasma actuators driven by repetitive nanosecond pulses". *Physics of plasmas*, **2007**, 14(7).
[105] T. Vu-Cong, F. Jacquier, and A. Girodet. "Electric field computation for HVDC GIS/GIL spacer under superimposed impulse conditions". 2019 IEEE Conference on Electrical Insulation and Dielectric Phenomena (CEIDP). IEEE, 2019: 409-412.
[106] Y. Serdyuk. "Propagation of cathode-directed streamer discharges in air", Proceedings of COMSOL Conference, Rotterdam, the Netherlands, 2013.
[107] X. Li, G. Zhang, X. Lin. "Influence of geometry and operation conditions on the surface charge characteristics of DC-GIL spacer", IET Generation, Transmission & Distribution, **2022**, 16(9): 1768-1779.
[108] P. Widger, M. Hills and D. Mitchard, "Schlieren Images of Negative Streamer and Leader Formations in CO_2 and a CF_3I-CO_2 Electronegative Gas Mixture". *Applied Sciences*. 2020; 10(22):8006.
[109] "Measurement System Signal Integrity: Important Factors to Consider," Technical Brief: 55W-18024-3, Tektronix Inc, 2010.
[110] Kutner, B. Y., A Study of Dalton's Law as Applied to Properties of Moist Air. America: University of Illinois at Urbana-Champaign, 1938.
[111] H. Koch, "Basic Information on Gas Insulated Transmission Lines (GIL)". *2008 IEEE Power and Energy Society General Meeting - Conversion and Delivery of Electrical Energy in the 21st Century*, pp. 1-4, 2008.
[112] H. Koch, "Gas Insulated Substation". John Wiley & Sons: Chichester, UK, 2014; pp. 18–49.
[113] Y. Kieffel, F. Biquez, and P. Ponchon, "Alternative Gas to SF_6 for Use in High Voltage Switchgears: g^3". *23rd International Conference on Electricity Distribution*, pp. 15-18, 2015.
[114] C. Li, et al., "Novel HVDC Spacers by Adaptively Controlling Surface Charges—Part II: Experiment". *IEEE Transactions on Dielectrics and Electrical Insulation,* **2018**, *25*, 1248–1258.
[115] C. Li, et al., "Novel HVDC Spacers by Adaptively Controlling Surface Charges—Part III: Industrialization Prospects". *IEEE Transactions on Dielectrics and Electrical Insulation,* **2018**, *25*, 1259–1266.
[116] E. Onal, "Breakdown Mechanism of Different Sulphur Hexafluoride Gas Mixtures". *Advances in Materials Science and Engineering*, **2018**, pp: 1-4.
[117] B. Zhang, X. Li, T. Wang, and G. Zhang, "Surface charging characteristics of GIL model spacers under DC stress in C_4F_7N/CO_2 gas mixture". *IEEE Transactions on Dielectrics and Electrical Insulation,* **2020**, *27*, 597–605.
[118] H. Koch, Gas Insulated Lines (GIL). In Substations*, CIGRE Green Books*, Switzerland, 2019; pp. 528–531.
[119] E. Laruelle, Y. Kieffel and A. Ficheux, (2018) "g^3 – The Alternative to SF_6 for High Voltage Equipment". *International Conference on Eco-Design in Electrical Engineering*, vol 440, 2017.
[120] H. Nechmi, A. Beroual, A. Girodet and P. Vinson, "Effective Ionization Coefficients and Limiting Field Strength of Fluoronitrile-CO_2 Mixtures".

IEEE Transactions on Dielectrics and Electrical Insulation, vol. 24, no. 2, pp. 886-892, April **2017**.

[121] M. Rabie and C. M. Franck, "Comparison of Gases for Electrical Insulation: Fundamental Concepts". *IEEE Transactions on Dielectrics and Electrical Insulation*, vol. 25, no. 2, pp. 649-656, April **2018**.

[122] B. Zhang, N. Uzelac and Y. Cao, "Fluoronitrile/CO_2 Mixture as an Eco-friendly Alternative to SF_6 for Medium Voltage Switchgears". *IEEE Transactions on Dielectrics and Electrical Insulation*, vol. 25, no. 4, pp. 1340-1350, **2018**.

[123] H. Nechmi, M. Slama, A. Haddad, G. Wilson, "AC Volume Breakdown and Surface Flashover of a 4% NovecTM 4710/96% CO_2 Gas Mixture Compared to CO_2 in Highly Nonhomogeneous Fields". *Energies*, 13, 1710, **2020**.

[124] Y. Zheng et al., "Dielectric Strength of 9%C_4F_7N/91%CO_2 Gas Mixture Under Three Typical Voltage Waveforms". *2021 IEEE 4th International Electrical and Energy Conference (CIEEC)*, pp. 1-5, 2021.

[125] F. Ye et al., "AC Breakdown Strength and its By-products of Eco-Friendly Perfluoroisobutyronitrile/O_2/N_2 Gas Mixture at High Pressure for HV Equipment". *IEEE Transactions on Dielectrics and Electrical Insulation*, vol. 28, no. 3, pp. 1020-1027, June **2021**.

[126] J. Wei, A. Cruz, F. Haque, C. Park and L. Graber, "Electrical Breakdown Characteristics of Supercritical Trifluoroiodomethane-Carbon Dioxide (CF_3I-CO_2) Mixtures". 2020 *IEEE Conference on Electrical Insulation and Dielectric Phenomena (CEIDP)*, pp. 427-430, 2020.

[127] S. Zhao, R. Zhong, D. Xiao and Y. Deng, "Investigation on Synergistic Effect of CF_3I Mixed Gas with Different Buffer Gases". *IEEE Transactions on Dielectrics and Electrical Insulation*, vol. 28, no. 2, pp. 745-751, Apr. **2021**.

[128] C. Tateyama, T. Kobayashi, A. Kumada and K. Hidaka, "Conceptual Design and Feasibility Study of Flexible Gas-Insulated Transmission Line Using CF_3I Gas Mixture". *IEEE Transactions on Dielectrics and Electrical Insulation*, vol. 28, no. 4, pp. 1424-1430, Aug. **2021**.

[129] H. Nechmi, M. Michelarakis, A. Haddad, G. Wilson, "Clarifications on the Behavior of Alternative Gases to SF_6 in Divergent Electric Field Distributions under AC Voltage". *Energies*, 14, 1065, **2021**.

[130] K. Takabayashi, R. Nakane, H. Okubo and K. Kato, "High Voltage DC Partial Discharge and Flashover Characteristics with Surface Charging on Solid Insulators in Air". *IEEE Electrical Insulation Magazine*, vol. 34, no. 5, pp. 18-26, **2018**.

[131] A. Pirker and U. Schichler, "Partial Discharges of Defects in Different Insulating Gases: N_2, CO_2, dry air and SF_6". *2018 12th International Conference on the Properties and Applications of Dielectric Materials (ICPADM)*, pp. 140-143, 2018.

[132] T. Götz, H. Kirchner and K. Backhaus, "Partial discharge Behavior of a Protrusion in Gas-insulated Systems under DC Voltage Stress". *Energies*, 13, 3102, **2020**.

Publications

Journals

N. Zebouchi, H. Li, and M. Haddad, “Development of Future Compact and Eco-Friendly HVDC Gas-insulated Systems: Shape Optimization of a DC Spacer Model and Novel Materials Investigation”. *Energies* 13.12 (2020): 3288.

H. Li, et al., “Development of Future Compact and Eco-friendly HVDC Gas Insulated Systems: Test Verification of Shape-optimized DC Spacer Models”. *Energies* 15.22 (2022): 8563.

Conferences

H. Li, N. Zebouchi, and M. Haddad, “Theoretical and Practical Investigations of Spacer Models for Future HVDC GIL/GIS Applications”. *The International Symposium on High Voltage Engineering (ISH)*, 2019.

H. Li, N. Zebouchi, M. Haddad, and A. Reid, “Partial Discharge Characteristics of Fluoronitriles/CO_2 and Trifluoroiodomethane/CO_2 Gas Mixtures under DC Voltage”. *2021 International Conference on Electrical, Computer and Energy Technologies (ICECET)*. IEEE, 2021.

H. Li, N. Zebouchi, M. Haddad, and A. Reid, “Characteristics for HVDC GIS/GIL Spacer under DC Superimposed Lightning Impulse Voltage Conditions”. *9th International Congress on Information and Communication Technology (ICICT)*, 2024.